CRUSTAL DEFORMATION ALONG THE SAN ANDREAS FAULT AND WITHIN THE TIBETAN PLATEAU MEASURED USING GPS

A

THESIS

Presented to the Faculty

of the University of Alaska Fairbanks

in Partial Fulfillment of the Requirements

for the Degree of

DOCTOR OF PHILOSOPHY

By

Qizhi Chen, B.S., M.S.

Fairbanks, Alaska

August 2002

ProQuest Information and Learning Company
300 North Zeeb Road
P.O. Box 1346
Ann Arbor, MI 48106-1346

CRUSTAL DEFORMATION ALONG THE SAN ANDREAS FAULT AND WITHIN THE TIBETAN PLATEAU MEASURED USING GPS

By

Qizhi Chen

RECOMMENDED:

Douglas H Christensen

Roger A Hansen

Advisory Committee Chair

Douglas H Christensen

Department Chair

APPROVED:

D Woodall

Dean, College of Science, Engineering and Mathematics

Dean of the Graduate School

8-12-02

Date

Abstract

Using the Global Positioning System (GPS), we study crustal deformation along the San Andreas Fault (SAF) in the San Francisco Bay area and within the Tibetan Plateau, and provide new constraints for the kinematics of these actively deforming plate boundaries.

GPS measurements in 1996 and 1997 and Electronic Distance Measuring (EDM) data from the 1970s and 1980s at sites along the SAF in northern California were used to determine the near-fault strain rate and to investigate the slip rate, locking depth, and rheology. We found a pronounced high near-fault shear strain rate that can be explained by a 2-D inhomogeneous model in which a low-rigidity compliant zone concentrates strain near the fault. We suggest that the materials on either side of the fault and the cumulative fault offset play a role in the development of the compliant zone. If such a compliant zone is present but unmodeled, the geodetic estimates of slip rate and locking depth (seismogenic depth) would be biased. This would lead to a miscalculated seismic hazard.

Thirteen GPS sites in southern Tibet, surveyed in 1995, 1998 and 2000, were merged with other data from China and Nepal into a single, self-consistent velocity field. The Himalaya and southern Tibet was modeled using a kinematically-consistent block model and elastic dislocation theory. We show a significantly lower convergence rate between India and Eurasia in central Himalaya than that previously estimated. We observe that southern Tibet undergoes non-uniform (spatial) east-west extension with one-half of the extension across the Yadong-Gulu rift. We infer that spatially non-uniform extension in southern Tibet results in variation of the arc-normal convergence rates along the Himalaya, and that the Yarlung-Zangbo suture or adjacent structure may be active as a right-lateral strike slip fault.

From 44 GPS sites in the Tibetan Plateau, we show that deformation of Tibet is distributed and strain accumulation is spatially uniform across the entire plateau. We propose a kinematic model for the Tibetan Plateau to be a combination of rigid block motion, pure shear and uniaxial contraction in the direction of about N32°E, comparable to the convergence direction between India and Eurasia.

Contents

List of Figures

List of Tables

Acknowledgements

This thesis would not be possible without the great support and encouragement from many people. I sincerely thank Dr. Jeffrey T. Freymueller, my advisor and committee chairman, for his enthusiasm, encouragement, and excellent scientific guidance throughout this study.

My sincere gratitude should be extended to my graduate advisory committee Drs. Douglas Christensen, Roger Hansen, Stephen McNutt, and Max Wyss, who have made helpful suggestions and provided guidance in many ways for my PhD program study.

I also thank my friends and colleagues who are/have been in Seismology Lab. Special thanks go to Drs. Stefan Wiemer, John Benoit, Chris Zweck, Kent Lindquist, Arthur Jolly, and Hilary Fletcher, Döerte Mann, Sigrún Hreinsdóttir, Liz Meyers, John Sánchez, Natalia Ratchkovski, Mitch Robinson and Lovro Valcic.

This is a data-driven thesis. I thank many people for their help in collecting data. Prof. ZhiQiang Yang from Chang'An University (China) coordinated the 1998 and 2000 Tibet campaigns; Wang Wenying, Ju Tianyi, Su Shengrui, Fu Zhongtan, and Ciwang contributed their endeavors to the survey. Wang Qi from Institute of Seismology, China Seismological Bureau, Xu Caijun and Jiang Weiping from Wuhan University kindly provided their published velocity field in China. I would also thank many people, whose names unfortunately I did not know, for their help in the field.

This project has been supported by USGS NEHRP Grant 1996-HQ-G02740, NSF Grant EAR 95-21922 and EAR 97-25563. I also acknowledge the Thesis Completion Fellowship from Graduate School, University of Alaska Fairbanks.

Last but not least, I am grateful to my wife, Xia Lin, for her dedicated love, her encouragement and support, without which none of this could be possible.

Chapter 1

Introduction

1.1 General

Plate tectonics has revolutionized the way geologists and geophysicists think about the Earth. Various tectonic features are observed along and/or near plate boundaries: collision (e.g., the India-Eurasia collision zone), subduction (e.g., the Aleutian arc), strike-slip faulting (e.g., the San Andreas fault), and extension (e.g., the Tibetan Plateau). A primary goal of studying plate tectonics is to understand seismic hazards throughout the plate boundaries. To accomplish this objective, accurate measurements of a plate motion and deformation are required and must be related to a source process. We use the Global Positioning System (GPS), a satellite-based geodetic technique for this work.

Scientists now have a fairly good understanding of how plates move and how such movements relate to earthquake activity. Based on the relative motion between two plates and whether oceanic or continental crust is at the edge of the lithospheric plate, three basic types of plate boundaries are recognized: (1) a divergent boundary, where lithospheric plates move away from each other and usually new crust is generated. The mid-Atlantic Ridge is one of the examples. (2) a convergent boundary, where lithospheric plates move toward each other and crust is destroyed. A special case of this is a collisional boundary, where two continental plates collide and their buoyancy resists subduction. The Tibetan Plateau and Himalaya are consequences of the collision between the Indian and Eurasian plates. (3) a transform boundary. At this boundary, plates slide past each other, and crust is neither

produced nor destroyed. The San Andreas fault in California is the most famous example, where the Pacific Plate slides past the North American Plate.

A plate boundary is not marked by a single fault but by a system of many faults. For example, the San Andreas fault system in northern California is composed of three right-lateral faults: the San Andreas, Ma'acama, and Bartlett Springs faults. The latter two faults are the northward extension of the Calaveras and Hayward faults in the San Francisco Bay area (Figure 1.1). A plate boundary deformation zone can be quite broad, often extending hundreds and sometimes thousands of kilometers into continental interiors, as illustrated by the Himalaya and Tibetan Plateau.

In this thesis, I focus on two main projects: (1) *Near-fault geodetic study of the San Andreas fault.* In this project, the San Andreas fault, a particular fault of a transform plate boundary is studied in detail. (2) *Kinematics and strain localization in the Himalaya and Tibet*, in which the broad kinematics of the India-Eurasia plate boundary zone in Tibet are investigated. Our challenge was to geodetically observe motions across the San Andreas fault and India-Eurasia collision zone using GPS in order to quantify rates of crustal deformation on the San Andreas fault and in the plateau, and to gain insight into the kinematics of these plate boundary zones.

The initial idea of the first project comes from differences in the observed near-fault distribution of strain along the San Andreas in the Point Arena and Point Reyes areas of northern California (Figure 1.1). In the Point Reyes area, a 3-4 km wide zone of pronounced strain around the San Andreas fault is observed [*Lisowski* et al., 1991]; in Point Arena this zone is absent [*Freymueller* et al., 1999]. To test for the presence of this zone in other locations along the San Andreas fault and explain its nature, we made GPS measurements in five small-aperture geodetic networks (Figure 1.1) along the San Andreas fault in San Francisco Bay area. The U. S. Geological Survey (USGS) established the trilateration networks and measured in these geodetic networks several times using Electronic Distance Measuring (EDM) in the 1970s and early 1980s to monitor deformation across fault zones in California [*Lisowski and Prescott*, 1981; *Lisowski* et al., 1991]. The combination of GPS and EDM measurements in these networks was used to determine the near-field strain rates and investigate the effects of the changes in material properties across the San Andreas fault system.

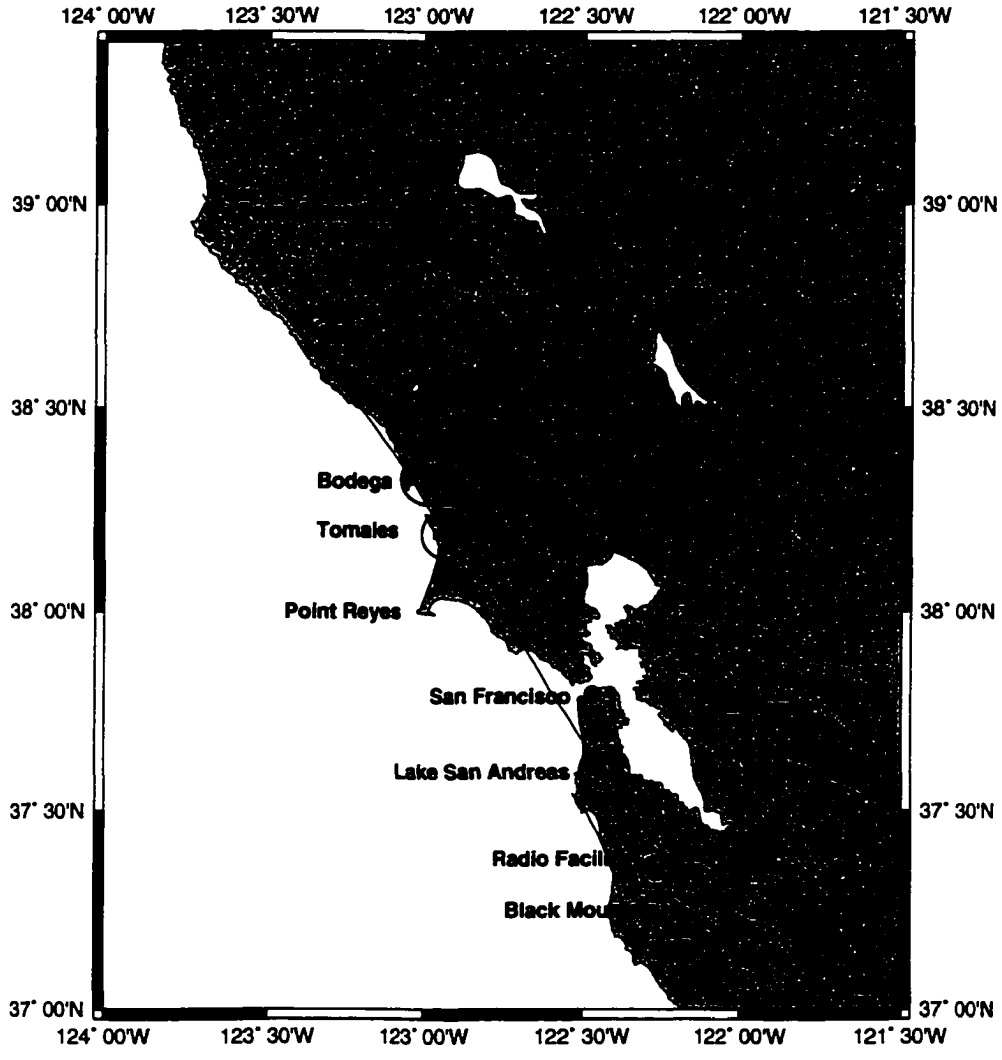

Figure 1.1. Map showing the study area in San Francisco Bay area. Large open circles show the locations of networks. Active faults are labeled with initials, SAF San Andreas Fault; MF Ma'acama fault; BSF Bartlett Springs fault; RCF Rodgers Creek fault; HF Hayward fault; CF Calaveras fault; SGF San Gregorio fault. Solid circle: San Francisco; Star: epicenter of the 1989 Loma Prieta earthquake.

In the second project (the Himalaya and Tibet project), eleven years of GPS data were used to investigate the present-day kinematics of the Tibetan Plateau. First, I focused on the study of active deformation in the Himalaya and southern Tibet. Then I expanded it to include strain accumulation across the entire plateau.

The Tibetan Plateau is the centerpiece of the broad India-Eurasia collision zone, and an ideal natural laboratory to study large-scale continental deformation. Questions about its origins, mechanisms, and tectonics have long fascinated researchers, and have been subject to much debate. Many attempts have been made to resolve these debates based on seismic, geologic, and geodetic data [*Molnar and Lyon-Caen*, 1989; *Armijo* et al., 1986, 1989; *England and Molnar*, 1997; *Holt* et al., 1995, 2000; *Bilham* et al., 1997; *Larson* et al., 1999], however, kinematic descriptions of the deformation field based on seismic and geologic data yield large uncertainties, and other precise kinematic data such as GPS data were very limited and sparse before this study.

A global plate motion model (NUVEL-1A) [*DeMets* et al., 1990, 1994] suggests that the NNE movement of India towards Asia varies from ~44 mm/yr in the western Himalaya to ~54 mm/yr in the eastern Himalaya (Figure 1.2). More recently, from space geodesy *Sella* et al. [2002] present the REVEL model, and show a lower rate of 31-40 mm/yr between India and Eurasia. Deformation within the India-Eurasia collision zone is typically diffuse. Although significant contraction occurs in the Himalaya [*Bilham* et al., 1997], about two-thirds of the plate convergence is distributed over length scales of hundreds and sometimes thousands of kilometers extending north and east of the Himalaya [*Tapponnier and Molnar*, 1977, 1979; *Armijo* et al., 1986].

Slip vectors of moderate earthquakes along the Himalayan arc show that the convergence along the Himalaya is approximately arc-normal [*Molnar and Lyon-Caen*, 1989]. If India is assumed to be rigid, this arc-normal slip requires ~N110°E extension of the southern Tibetan plateau at a rate approximating the rate of convergence between India and Eurasia [*Molnar and Lyon-Caen*, 1989]. The rate of extension across southern Tibet was estimated as 5-10 mm/yr by *Baranowski* et al. [1984], 18±9 mm/yr towards ~N115°E by *Molnar and Lyon-Caen* [1989] from seismic moment release in earthquakes, and 10±5 mm/yr by *Armijo* et al. [1986] from geologic mapping and interpretation of Landsat images. However, all these estimates based on either seismic or geologic data yielded large uncertainties.

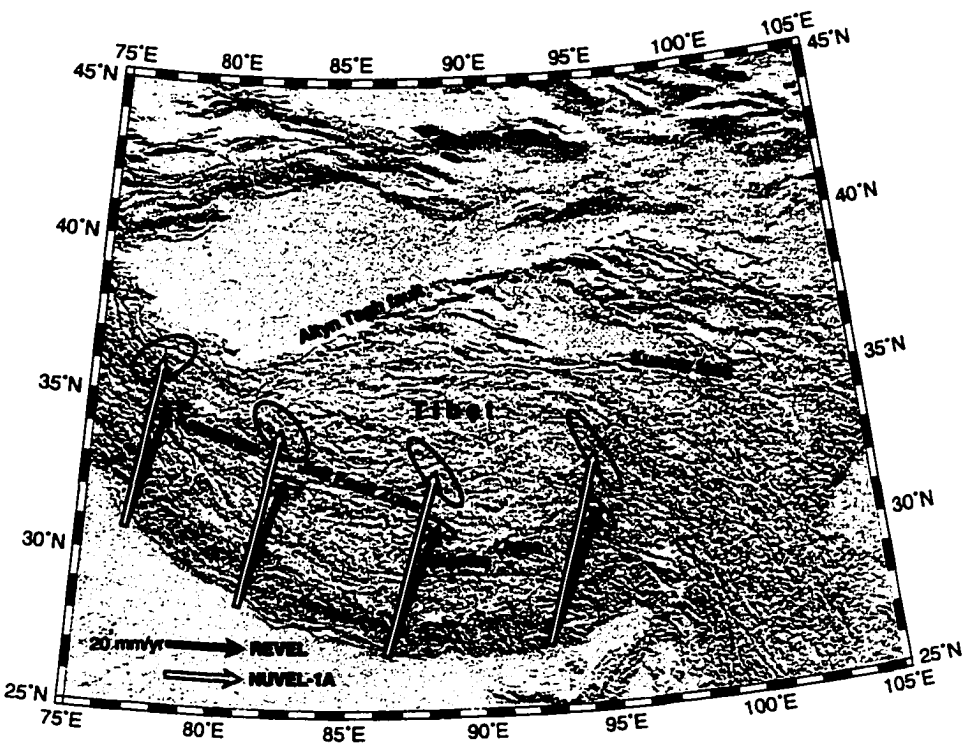

Figure 1.2. Shaded relief map of the Tibetan Plateau. Vectors with 95% ellipses show the NNE movements of India towards Eurasia along the Himalaya. Solid vectors: predicted by REVEL model; Open vectors: predicted by NUVEL-1A model.

A precise estimated extension rate in southern Tibet will help to understand the present kinematics and development of the Himalaya and Tibetan plateau.

The Tibetan Plateau is the largest expanse of high topography and anomalously thick continental crust on Earth. The thickened crust attests to the role of plate convergence in producing the plateau. How this convergence is accommodated within the crust and upper mantle underlying the Tibetan Plateau, however, remains a central question in the tectonics of the region. Two competing mechanisms have been proposed to describe this accommodation: (1) shortening and thickening of the crust, evidenced in the ~5 km average elevation of the Tibetan Plateau and a crustal thickness of ~70 km [e.g., *England and Houseman*, 1986], and (2) strike-slip faulting that transports material away from the collision, with corresponding eastward extrusion of Tibet [e.g., *Molnar and Tapponier*, 1975]. Resolving the debate of the crustal thickening versus lateral extrusion has important consequences for geodynamic models of the regions [e.g., *England and Houseman*, 1986; *Royden* et al., 1997].

Precise measurements of surface deformation throughout the India-Eurasia collision zone will help to resolve this debate. We made GPS measurements in Tibet by cooperating with Chinese scientists, analyzed and merged these data with all other data in China and Nepal into a single self-consistent velocity field [*Wang* et al., 2001]. In this thesis, I present results from GPS measurements at 71 sites in Nepal and the Tibetan Plateau to answer several major tectonic questions regarding the Tibetan Plateau: How rapidly is east-west extension occuring in southern Tibet? Is this extension spatially variable or uniform? What is the tectonic source for the east-west extension? How does local faulting such as Yadong-Gulu rift relate to the convergence between India and Eurasia? Is the deformation caused by the continental collision between India and Eurasia distributed across the entire plateau or localized on major faults? Is lateral extrusion or crustal thickening dominant in absorbing the convergence? Is the strain accumulation spatially variant or uniform? How fast is the eastward extrusion of eastern Tibet? Does it result only from large-scale strike-slip faulting, as proposed by *Armijo* et al. [1989]? If not, what is an alternative tectonic source?

In this thesis, I address these tectonic questions using GPS measurements. Models are presented to interpret the observations, and the tectonic implications of the models are discussed.

1.2 GPS Analysis

The GPS data presented in this thesis were analyzed using the GIPSY/OASIS II software (release 6) developed at the Jet Propulsion Laboratory (JPL) [*Zumberge* et al., 1997]. Raw GPS data collected in the field were analyzed in 24-hour daily solutions along with regional and global permanent sites. A total of 354 sites and 1250 daily solutions were analyzed and merged into a self-consistent solution [*Wang* et al., 2001].

Two types of GPS solutions were used in *Wang* et al. [2001] and also in this thesis. For data observed between 1991 and 1995, global solutions were estimated using all data from our network, along with a well-distributed set of global sites. In these solutions, GPS satellite orbit parameters were estimated together with all these station coordinates using the same models used by JPL in its current International GPS Service (IGS) analysis [*Zumberge* et al., 1997]. The selection of global sites varied with time as the global GPS network grew. Prior to 1994, the available global GPS sites were limited, so we included all global sites. Beginning in 1994, for those days when there were too many global sites to use along with the campaign sites, some sites far away from Tibet were excluded.

In the other type of solutions for those surveyed after 1995, we used regional solutions by combining campaign data with a regional set of permanent sites and used fixed orbits and satellite clock provided by JPL. For more details about solution strategy, refer to *Larson* et al. [1997]; *Freymueller* et al. [1999, 2000].

Then the daily free network solutions were transformed into the ITRF97 reference frame (International Terrestrial Reference Frame, epoch 1997) by estimating a seven-parameter similarity transformation for each solution [*Boucher* et al., 1999]. Finally, the individual daily GPS solutions were combined together to determine site velocities. The coordinates in the ITRF97 reference frame and their covariance matrix from the daily GPS solutions were used in a standard weighted least squares fit to estimate site positions at epoch 1995.0 and site velocities. The input covariances were scaled by a factor of 7.5, so that the reduced chi-squares statistic was equal to 1.0. *Wang* et al. [2001] used a total of 1250 daily GPS solutions spanning from March 1991 to January 2001 to estimate velocities for 354 sites in China and its vicinity.

The GPS results I present here are based on an improved version of the velocity field of

Wang et al. [2001]. Several updates and changes have been made in the velocity solution of *Wang* et al. [2001]. I fixed antenna height errors at some sites, fixed a reference clock problem that biased a few solutions, excluded a few outlier measurements, and added more data from regional permanent sites. Some additional solutions were added that slightly extend the time span of the observarions. About 60% of the solutions used in *Wang* et al. [2001] were improved in some way, although many changes were minor. New observations at some permanent sites from China are included here, which were not available to *Wang* et al. [2001]. The velocity field I use in this thesis was estimated from a total of 1580 daily GPS solutions spanning March 1991 to July 2001. Only 71 sites in Nepal and Tibet are discussed here.

For ease of interpretation, we express our velocities either relative to one particular site, usually a permanent site, or relative to a stable plate by subtracting the motion of the site (called reference site) or the plate relative to the ITRF97 reference frame, respectively. In this thesis, I chose Lhasa (LHAS), an IGS site, and Xigatse (XIGA) as reference sites (Figure 1.2). I also depict the velocity field in an "India-fixed" and an "Eurasia-fixed" frame when studying the kinematics of the Himalaya and southern Tibet, and the entire plateau, respectively. The site velocities relative to India/Eurasia-fixed frames depend on the plate motion model used. Figure 1.2 shows the predicted relative motions between India and Eurasia from the NUVEL-1A [*DeMets* et al., 1990, 1994] and REVEL [*Sella* et al., 2002] models. REVEL predicts that India moves at a significantly slower rate relative to Eurasia than does NUVEL-1A. The NUVEL-1A model is constrained only by seafloor spreading data, and there are no direct data measuring the convergence rate between Eurasia and India. The REVEL model was based entirely on precise space geodesy, and is consistent with other results based on different data sets. For example, the site velocities in Tibet relative to Eurasian reference frame defined by REVEL are in a good agreement (within 1 mm/yr) with those defined by *Wang* et al. [2001]. We use the REVEL [*Sella* et al., 2002] model to define a Eurasia-fixed and India-fixed reference frame in this study.

1.3 An overview of the Chapters

This thesis is divided into six chapters: this general introduction, three journal article manuscripts, a general conclusion, and a bibliography containing the references for all chapters in this thesis. Each of the main science chapters is presented in journal format with an abstract, introduction, method, result, discussion, and conclusion specific to that chapter.

Chapter 2 explores a 2-dimensional inhomogeneous dislocation model in which a low-rigidity compliant zone is embedded in the fault zone to interpret the observed high strain rate near the San Andreas fault in the San Francisco Bay area. A combination of GPS measurements and EDM data at sites in five small-aperture geodetic networks along the San Andreas fault (SAF) in northern California are first used to determine near-fault strain accumulation rates along the SAF, and then to test whether lateral variations in elastic moduli are important. We find that along most of the San Andreas fault in the San Francisco Bay area, the near-fault strain rate is significantly higher than would be expected based on uniform half-space models, and a model in which the fault is embedded within a narrow compliant zone best explains the data. This chapter was published in the *Bulletin of the Seismological Society of America* in March 2002. It has been slightly modified and formatted to be in accordance with the university thesis requirements.

In Chapter 3, we present results from GPS measurements of 17 sites in southern Tibet. By combining these data with 15 sites in Nepal, we investigate the present-day active deformation in southern Tibet and its causative mechanisms. All the observations are modeled by a series of blocks and dislocations. A manuscript about this chapter is in preparation and will be submitted to the *Journal of Geophysical Research.*

Chapter 4 focuses on a study of the present-day kinematics of the Tibetan plateau using a subset of data from *Wang* et al. [2001]. The hypothesis of spatially uniform strain accumulation was tested. A model of a combination of rigid block motion, pure shear, and uniaxial contraction is proposed to describe the present kinematics of the Tibetan plateau. Slip rates on two major strike-slip faults in the Tibetan plateau are suggested to be lower that those estimated from geologic evidence. A manuscript for this chapter is in preparation and will be submitted to the *Journal of Geophysical Research.*

The final chapter (Chapter 5) presents the general conclusions for the thesis, along with

an outline for future research directions.

Chapter 2

Geodetic Evidence For A Near-Fault Compliant Zone Along the San Andreas Fault in the San Francisco Bay Area[1]

2.1 Abstract

GPS measurements in 1996 and 1997 and EDM data from the 1970s and 1980s at sites in five small-aperture geodetic networks along the San Andreas fault in northern California were used to determine the near-fault strain rate. The tensor shear strain rate $\dot{\epsilon}_{12}$ (referred to a coordinate system with the 1 axis parallel to the fault and the 2 axis normal to the fault) in the Bodega-Tomales, Lake San Andreas, and Black Mountain-Radio Facility networks (from north to south) are 0.339±0.025, 0.366±0.095, and 0.316±0.060 μstrain/yr, respectively. The shear strain rate near the fault in the Black Mountain-Radio Facility and Lake San Andreas networks can be explained either by a 2D inhomogeneous model in which a low-rigidity compliant zone concentrates strain near the fault, or by a very shallow locking depth of 8 km. Other evidence points to a locking depth >10 km, so we prefer the

[1]Published under the same title with authors Q. Chen and J. T. Freymueller in *Bulletin of the Seismological Society of America, 92,* No. 2, pp. 656-671, 2002

first explanation. The contrast in rigidity between the fault zone and the surrounding rock appears to become stronger to the south, starting at approximately the northern extent of the Salinian block at Bodega Bay, suggesting that both the materials on either side of the fault and the cumulative fault offset play a role in the development of a compliant fault zone. Estimates of fault slip rates from far field geodetic data are only weakly sensitive to the presence of a compliant zone, but estimates of locking depths can be biased by ~10% toward shallower values if a compliant zone is present and unmodeled.

2.2 Introduction

The Peninsula and North Coast segments of the San Andreas Fault (SAF) have not experienced significant seismicity since 1906, although several earthquakes have ruptured further south. In the absence of seismicity, geodetic measurements take on a special importance for characterizing the strain accumulation mechanism and future seismic hazards in the San Francisco Bay area. Many models have been proposed to explain the deformation associated with the earthquake cycle on strike-slip faults [*Thatcher*, 1974, 1983; *Savage and Prescott*, 1978; *Thatcher* et al., 1997; *Li and Rice*, 1987; *Thatcher and England*, 1998; *Savage*, 1990, 1998; *Savage* et al., 1999; *Matthews and Segall*, 1993]. Many of these models regard the earth as a homogeneous elastic half-space, but variations in the elastic properties of the earth can have significant effects on slip models derived from surface displacements [*Árnadóttir* et al., 1991; *Du* et al., 1994].

In this chapter, we use a combination of GPS measurements and EDM data at sites in five small-aperture geodetic networks (Figure 2.1) along the San Andreas fault in northern California to test whether lateral variations in elastic moduli are important. We determine the near-fault strain accumulation rates along the SAF from near-fault geodetic data and use these to determine the near-fault properties. We find that along most of the San Andreas fault in the San Francisco Bay area, the near-fault strain rate is significantly higher than would be expected based on uniform half-space models, and a model in which the fault is embedded within a narrow compliant zone best explains the data.

According to the NUVEL-1A model [*DeMets* et al., 1990, 1994], the Pacific plate moves at 45 mm/yr N35°W toward North America in northern California. Most of this motion is

accommodated along the San Andreas fault system, which consists of the SAF and often one or more subparallel faults. Slip rates on the SAF are well-known from paleoseismic studies [e.g., *Schwartz* et al., 1998; *Hall* et al., 1999; *Working Group on California Earthquake Probabilities*, 1999] For example, north of the San Francisco Bay, *Niemi and Hall* [1992] estimated the slip rate on the San Andreas at Vedanta Retreat wind gap, near Point Reyes (~38°N) to be 23±3 mm/yr. Further north at Point Arena (~39°N), *Prentice* [1989] estimated the slip rate to be 25±3 mm/yr. *Working Group on California Earthquake Probabilities [1999] (WGCEP99)* adopted slip rates on the Santa Cruz Mountains and Peninsula segments of 17±2 mm/yr, and 24±1.5 mm/yr on North Coast South segment. The large-scale deformation field in northern California is also known from repeated laser trilateration measurements [*Lisowski* et al., 1991] and GPS data [*Williams* et al., 1994; *Freymueller* et al., 1999], and from the displacements caused by the 1906 earthquake [*Thatcher* et al., 1997].

2.2.1 Near-fault Geodetic Data

The U. S. Geological Survey (USGS) established many trilateration networks and measured them several times by Electronic Distance Measuring (EDM) in the 1970s and early 1980s to monitor deformation across fault zones in California [*Lisowski and Prescott*, 1981; *Lisowski* et al., 1991]. The five networks we used in this paper are (from north to south) Bodega Bay, Tomales Bay, Lake San Andreas, Radio Facility and Black Mountain (Figure 2.1). Each network typically spans 2-5 kilometers on either side of the surface trace of the fault. In most of these networks, no EDM measurements were made after the 1980s. We surveyed each of these networks using the Global Positioning System (GPS) in 1996 and 1997. We combined data from the adjacent Black Mountain and Radio Facility networks, and also the adjacent Bodega and Tomales networks, to estimate the near-fault strain rate tensor at three locations along the SAF. The Black Mountain-Radio Facility, Lake San Andreas, and Bodega-Tomales networks (Figure 2.1) are located in Santa Cruz Mountains, Peninsula, and North Coast South fault segments, respectively, defined by *WGCEP99*. Additional strain rate measurements are available at Point Reyes [*Lisowski* et al., 1991] and Point Arena [*Freymueller* et al., 1999].

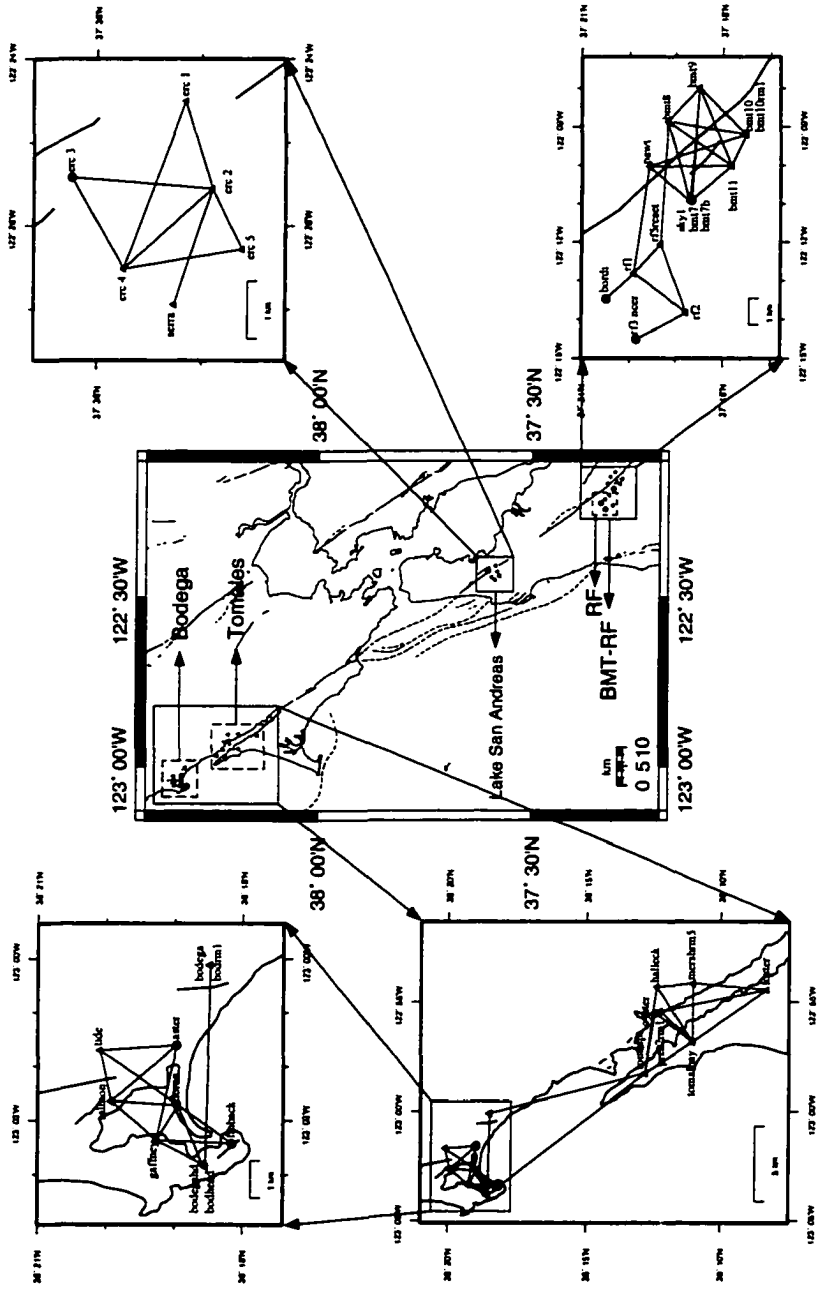

Figure 2.1. Map showing the network locations in California and the line lengths observed in this study. Solid triangles represent the EDM sites which have GPS surveys, solid circle represents the EDM sites that have no GPS survey.

2.2.2 Past Non-uniform Models

Although simple geodetic models to date can explain most observations of the deformation along the SAF, most models regard the earth as a homogeneous elastic half-space. Variations in the elastic properties of the earth can have significant effects on slip models derived from surface displacements [*Árnadóttir* et al., 1991; *Du* et al., 1994; *Thatcher*, 1983], *Savage* [1990] and *Savage* et al. [1999] suggested a viscoelastic coupling model featuring a layered elastic and viscoelastic medium, or vertical variations in rheology.

Models including lateral variations in rheology have been proposed as well. [*Lisowski* et al., 1991] suggested that the steep velocity gradient and pronounced asymmetry in velocities across the fault at Point Reyes can be explained by a model with differing elastic properties on either side of the San Andreas fault. A low modulus zone centered on the fault concentrates strain near the fault [*Rybicki and Kasahara*, 1977].

Two observations suggest that the strain rate near the SAF varies along strike. *Prescott* et al. [1979] found that shear strain rates in northern California appear to be high close to the faults; near fault shear strain rates along the San Francisco Peninsula are $0.6\pm0.1\times10^{-6}$ yr^{-1} (0.6 μstrain/yr) (engineering) with direction N47°W±9° [*Prescott* et al., 1981]. Near 38°N at Point Reyes, $0.64\pm0.07\times10^{-6}$ yr^{-1} (0.64±0.07 μrad/yr) of shear strain is concentrated near the San Andreas [*Prescott and Yu*, 1986]. The Point Reyes result was confirmed by *Lisowski* et al. [1991]. Similar strain rates were determined from repeated triangulation measurements between 1931 and 1978 by *Cline* et al. [1985]. In contrast, *Freymueller* et al. [1999] examined GPS-EDM line length changes at Point Arena network, and found a very small near-fault strain rate (0.022±0.084 μstrain/yr); the line length changes could be fit by a uniform half-space screw dislocation model with a deep locking depth of >12 km; these data provide only a lower bound on locking depth. The variation in strain rate appears to be greater than what would be predicted based on known variations in slip rate and locking depth.

2.3 Measurements and Analysis

2.3.1 EDM Networks and Measurements

The five short-range networks studied in this paper were installed by the USGS in the 1960s to 1980s [*Lisowski and Prescott*, 1981] and were surveyed from the 1970s to early 1980s. One network was resurveyed following the 1989 Loma Prieta earthquake. There are total of 34 sites in these networks, and most of them are located less than 2 km from the fault.

Table 2.1 summarizes the observation history of the networks. The EDM data we are using here were measured by several different instruments: Geodolite, Hewlett-Packard model 3800A, and Hewlett-Packard model 3808. All three are commercial electro-optical distance-measuring instruments. The operation is similar for all of the instruments [*Savage and Prescott*, 1973; *Lisowski and Prescott*, 1981]: a modulated beam is projected from the instrument to a remote retroreflector, which reflects the beam back to the instrument. Comparing modulation phases of the incoming and outgoing beams, the instrument determines the length of the optical path between instrument and retroreflector by adding a precisely measured fractional modulation length and an unknown number of whole modulation lengths. The unknown number of whole modulation lengths can be determined by measuring at successively lower modulation frequencies [*Savage and Prescott*, 1973].

The Black Mountain network consists of six stations. Three different marks (bmt7, bmt7b, and sky1) were used at one station, and two different marks at another (bmt10, and bmt10rm1). The use of different marks at the same station resulted from the line of sight requirements of EDM. The Radio Facility net, ~5 km east of the Black Mountain network, consists of six sites, all on the southwest side of the fault. One site could not be reached because we could not contact the landowner for permission. Two lines (pawt-rf1, and bmt8-rf5reset) connect the two nets. We analyzed the Black Mountain and Radio Facility networks separately, and also as a combined network (BMT-RF).

The Bodega network has nine sites, and a total of 17 lines were surveyed by EDM. In the field we found that the site Knobreset appeared to be sliding down a steep hill, so we excluded it when the line length changes confirmed this. We also excluded two lines (bodegahd-finback and doran-finrm2) because of extremely large uncertainties. The sites Finback and Finrm2 could not be found in 1996-7. The Tomales network consists

Table 2.1. Summary of EDM measurements of the line lengths† for California

Net Name	Line	Length in m	EDM Observation First	Last	Total	dL/dt mm/yr	σ mm/yr
BMT	bmt10-bmt11	1313.152	75.1	91.8	8	0.4	0.2
+	bmt10-bmt9	2526.587	75.1	91.8	6	-0.4	0.3
RF	bmt10-pawt	4003.497	75.1	91.8	8	-0.7	0.3
	bmt10rm1-bmt8	3066.003	77.0	77.1	2	-0.7	0.4
	bmt10rm1-bmt9	2521.301	77.0	91.8	7	-0.2	0.3
	bmt11-bmt7	2105.543	75.1	80.3	3	0.4	0.9
	bmt11-bmt8	3002.322	75.1	91.8	10	0.0	0.2
	bmt11-bmt9	3231.704	75.1	91.8	8	0.8	0.2
	bmt11-pawt	3267.816	75.1	91.8	8	-1.0	0.3
	bmt11-sky1*	2127.350	82.2	91.8	5	0.5	0.4
	bmt7-bmt8	3182.152	75.1	80.3	3	1.1	0.5
	bmt7-bmt9	4373.392	75.1	80.3	3	1.9	0.5
	bmt7b-bmt8	3182.393	82.1	91.8	5	0.4	1.1
	bmt7b-pawt	2132.329	75.1	91.8	8	-0.2	0.9
	bmt8-bmt9	1806.900	75.1	91.8	8	-0.1	0.1
	bmt8-rf5reset*	4711.993	82.1	91.8	5	2.0	0.4
	bmt9-sky1*	4383.999	82.1	91.8	5	1.7	0.4
	pawt-rf1	4150.492	75.1	91.8	9	1.3	0.2
	bordi-rf1*	1488.474	75.9	89.6	4	0.4	0.5
	rf1-rf2	2593.111	75.9	89.6	6	-0.4	0.3
	rf1-rf5reset	1539.857	75.9	89.6	4	0.0	0.1
	rf2-rf3ncer*	2077.306	75.9	80.3	3	0.6	1.0
	rf2-rf5reset	2832.057	75.9	89.6	4	0.5	0.4
Lake San	erc 1-erc 2	1628.838	75.1	91.8	12	0.7	0.2
Andreas	erc 1-erc 4	3171.273	75.1	91.8	9	1.3	0.2
	erc 2-erc 3*	2377.011	75.1	91.8	11	-1.0	0.3
	erc 2-erc 4	2112.220	75.1	91.8	9	-0.1	0.2
	erc 2-erc 5	1197.410	75.1	91.8	9	-0.2	0.1
	erc 2-serra	2155.874	78.8	91.8	4	0.0	0.5
	erc 3-erc 4*	1782.677	75.1	91.8	10	0.6	0.3
	erc 4-erc 5	2125.008	75.1	91.8	8	-0.3	0.2

Net Name	Line	Length in m	EDM Observation First	Last	Total	dL/dt mm/yr	σ mm/yr
Bodega +	aster-gaffney*	2638.124	75.3	82.5	5	1.4	1.3
Tomales	aster-salmon*	2288.365	75.3	82.5	6	0.0	1.4
	aster-tide*	1989.795	75.3	82.5	6	-1.3	0.7
	bodegahd-doran	1727.083	75.3	84.3	7	0.3	0.2
	bodegahd-gaffney	1410.430	75.3	82.5	6	-0.5	0.2
	doran-finback*	1698.217	75.3	80.4	5	-1.9	1.3
	doran-gaffney	1104.696	75.3	84.3	7	0.1	0.1
	doran-salmon	1812.191	75.3	84.3	7	-1.3	0.2
	doran-tide	2577.218	75.3	82.5	7	-0.5	0.2
	finback-gaffney*	1960.088	75.3	80.4	5	0.5	1.0
	gaffney-salmon	1610.957	75.3	82.5	6	-0.4	0.1
	salmon-tide	1407.259	75.4	82.5	6	0.3	0.2
	bod head-bod rm1	5401.734	83.8		1	1.5	0.3
	bod head-tomal pt	13301.578	83.8		1	0.4	0.3
	bod rm1-tomal pt	10727.201	83.8		1	-1.5	0.2
	foster-mershrm5	5002.630	83.8		1	-1.6	0.2
	foster-oyster	7837.232	83.8		1	-2.0	0.2
	foster-tomalbay	6069.057	83.8		1	0.3	0.2
	halleck-mershrm5	2594.438	83.8		1	-1.0	0.2
	halleck-tomal pt	5874.939	83.8		1	1.8	0.2
	halleck-tomalbay	4490.871	83.8		1	-0.5	0.2
	mershrm5-tomalbay	3923.228	83.8		1	1.2	0.2
	oyster-tomal pt	4138.366	83.8		1	2.5	0.2
	oyster-tomalbay	3317.750	83.8		1	-0.7	0.2
	pres2rm1-tomalbay	3238.038	83.8		1	0.0	0.2
	tomal pt-tomalbay	4014.637	83.8		1	-0.6	0.2

†In addition to the EDM observation, all lines except those indicated were surveyed by GPS in 1996 and/or 1997.

*Lines that have no GPS measurements.

of eight sites and 18 lines were surveyed by EDM in 1983. Two lines (bod head-tomal pt and bod rm1-tomal pt) link the Bodega and Tomales networks. We analyzed the Bodega and Tomales networks separately and also combined them into a single Bodega-Tomales network.

The Lake San Andreas network has six stations, two of which are on the east of SAF and four on the west of SAF. Eight lines were measured in this network. One of these sites was destroyed by construction between the last EDM occupation and 1996.

2.3.2 EDM Data Analysis

We used programs developed by the USGS to process the raw EDM data. A few changes in the source code were required to remove system-dependent code and make the programs portable to modern UNIX computers. Our revised versions are available on the Internet (ftp://giseis.alaska.edu/pub/USERS/qzchen/EDMprogs). Each type of instrument required use of a different program.

The measured distance must be corrected for variations in refractivity of the air along the line based on the temperature, pressure, and humidity. Two types of atmospheric measurements were used to correct the refractivity. For some Geodolite data, the temperature and humidity of the atmosphere along the line were measured from an aircraft and the pressure was measured at the two endpoints. For HP3800 and HP3808 and the remaining geodolite data, pressure temperature and humidity were measured at each end of the line and their mean values used to correct the distance measurement.

The raw EDM observations were first reduced to the instrument to reflector distance, then to the mark to mark distance using the measured heights of the instrument and reflector. Finally the mark to mark distance was projected into a horizontal distance on the ellipsoidal reference system (called the sea level arc distance). The mark to mark distance is only weakly sensitive to the assumed site coordinates (about 0.1 mm-1 mm), but the sea level arc distance is very sensitive to the assumed site coordinates, especially the height. This sensitivity results from the large elevation differences that are typical of these lines.

The assumed site coordinates used by the USGS to process raw EDM data were estimated from maps, which led to horizontal errors of several tens of meters and height errors of 15 m or more. The GPS-derived coordinates, on the other hand, are self-consistent to $\sim$1

cm, but are in a different horizontal datum and heights are referenced to the ellipsoid rather than the geoid. In order to compare line lengths projected to the horizontal plane using the two different systems, it is critical that the site coordinates used in projecting the GPS and EDM line lengths be the same. Otherwise there would be a significant bias between the projected measurements of the two systems. For example, for the baseline bmt10-pawt (~4 km), the sea level arc distance differs by ~20 mm when the site coordinates originally assumed by the USGS are changed to those derived from the GPS data. Poor height information can also result in errors in the atmospheric corrections. We improved the processing of short, steep EDM lines using the improved knowledge of site coordinates given by GPS. Note that it is only important that all data for a given line are projected using the same coordinates.

The precision of EDM line lengths is characterized by a standard deviation $\sigma = (a^2 + b^2L^2)^{1/2}$ where L is the line length, a and b depend on the instruments used. For geodolite data, $a = 3$ mm, and $b = 2.0\times10^{-7}$ [*Savage and Prescott*, 1973], and for HP3800 and HP3808 data, $a = 4.5$ mm, and $b = 0$ [*Lisowski and Prescott*, 1981]. For the typical line length (2 km) used in these networks, σ=3 mm for geodolite data and 4.5 mm for HP3800/HP3808 data.

2.3.3 GPS Measurements and Analysis

Using the Global Positioning System (GPS), we measured most of the sites in the BMT-RF, Lakes San Andreas, and Bodega-Tomales networks in 1996 and 1997, with measurements at each site generally lasting from 1 to 3 days. Where there were multiple marks at the same sites, we carried out short survey tie occupations of all marks and then made longer observations at one mark. A total of nine sites in the Black Mountain-Radio Facility (BMT-RF) network, 15 sites in the Bodega-Tomales networks, and five sites in the Lake San Andreas network were surveyed. Some sites were known to be destroyed and a few sites could not be found. In Table 2.1, the lines without GPS data are marked by asterisks.

The GPS data were analyzed using the GIPSY/OASIS II software developed at the Jet Propulsion Laboratory [*Zumberge* et al., 1997]. Our analysis methods are described in more detail by *Larson* et al. [1997] and *Freymueller* et al. [1999]. For the very short baselines used in this study, we modified our standard analysis scheme by estimating only a constant

tropospheric delay parameter for each site. This assumes that any time variation in the tropospheric path delay is the same for all sites. Most baselines used in this study are less than 5 km long, and we successfully resolved the phase ambiguities for almost every baseline. The GPS ambiguity-fixed solutions improved from 2-4 mm to 1-2 mm in the uncertainty of the east components of the baselines. Ambiguity resolution is most important for a few sites with short observation times, which improved from a precision of 10-20 mm to 2-4 mm.

2.3.4 Line Length Change Rates and Strain Rates

Line lengths computed from the GPS solutions were compared to the EDM line lengths. A systematic scale difference between the two systems were removed in order to make this comparison. GPS line lengths must be multiplied by $(1+0.283\times10^{-6})$ to remove the scale difference [*Savage* et al., 1996]. This scale difference results in a ~1.4 mm difference in the length of a 5 km baseline, which is comparable to the measurement precision. A portion of this scale difference is explained by the use of an older, less accurate value of the speed of light in the EDM reductions.

Then the EDM and GPS line lengths in the BMT-RF and Lake San Andreas networks were corrected for coseismic deformation caused by 1989 Loma Prieta earthquake using the coseismic slip model of *Árnadóttir and Segall* [1994]. Coseismic line length changes were up to 14 mm. The Bodega-Tomales network is located far from the 1989 coseismic rupture, and the effect of Loma Prieta earthquake is not significant (~0.03 mm). The line lengths in the BMT-RF were also corrected for postseismic deformation following the Loma Prieta earthquake using the model of *Bürgmann* et al. [1997]. Postearthquake displacements in the Lake San Andreas and Bodega-Tomales networks are not significant.

To calculate the near-fault strain rate, we made two assumptions: temporal and spatial uniformity of strain. First, we assumed the rate of strain accumulation was constant in any given time period (temporally). Second, we assumed the strain accumulated uniformly over each network (spatially). We used a weighted least squares regression model to determine the rates of change of the line length dL/dt [*Savage* et al., 1986]. The weight is $1/\sigma^2$, where σ was defined earlier for the EDM data, and for GPS, σ is the formal uncertainty of the baseline length. The dL/dt for each line is shown in Table 2.1. Line length versus time plots

are shown in Figures 2.2a-2.4a. The calculated line length change rates are the same by using mark to mark distance or sea level arc distance, as long as the same site coordinates are used in all computations.

Tensor shear strains are used in this paper rather than engineering shear strains. The uniform (spatial) strain rate and its standard deviation can be extracted from measurements of dL/dt based on the following linear model in the east-north coordinate system [*Prescott* et al., 1979; *Savage* et al., 1986].

$$\dot{\varepsilon}_i = \frac{dL_i/dt}{L_i} = \dot{\varepsilon}_{11}\cos^2\theta_i + 2\dot{\varepsilon}_{12}\cos\theta_i\sin\theta_i + \dot{\varepsilon}_{22}\sin^2\theta_i$$

Here $\dot{\varepsilon}_i$ is the strain rate in ith line, θ_i is the orientation of the ith baseline with respect to the x_1-axis (east, clockwise angles are positive). The components $\dot{\varepsilon}_{11}$ and $\dot{\varepsilon}_{22}$ are the extension rates in the east-west and north-south directions, respectively, and $\dot{\varepsilon}_{12}$ is the right lateral shear across a north-south line. We need at least three lines of different orientations in order to determine the three components. We then transform the strain tensor to a fault-parallel/fault-normal coordinate system, so the shear strain rate corresponds directly to shear parallel to the fault. In this coordinate system we expect that in general $\dot{\varepsilon}_{11}$=$\dot{\varepsilon}_{22}$=0.

The uniform strain rate that best fits the observed line length changes within each network is given as the "observed" strain rate in Table 2.2 and shown in Figures 2.2b-2.4b. The observed interseismic tensor shear strain rates in the BMT-RF, Lake San Andreas and Bodega-Tomales networks are 0.316±0.060, 0.366±0.059, and 0.339±0.025 μstrain/yr, respectively. The near-fault strain rate increases systematically from the BMT-RF to the north at Point Reyes [*Prescott and Yu*, 1986; *Lisowski* et al., 1991], then decreases in the Bodega-Tomales network and further north at Point Arena [*Freymueller* et al., 1999].

2.4 Dislocation Models

2.4.1 2D Uniform Model

Assuming a fault is long and straight and the deformation is uniform in the direction of fault strike, a simple physical model of a 2D uniform half-space screw dislocation model can be used to model a strike-slip fault, in which the upper part of the fault is locked between earthquakes, and the lower part of the fault slips at the long-term slip rate [*Sibson*, 1982, 1983]. The depth of the locked zone (D) is termed the locking depth, which is thought to

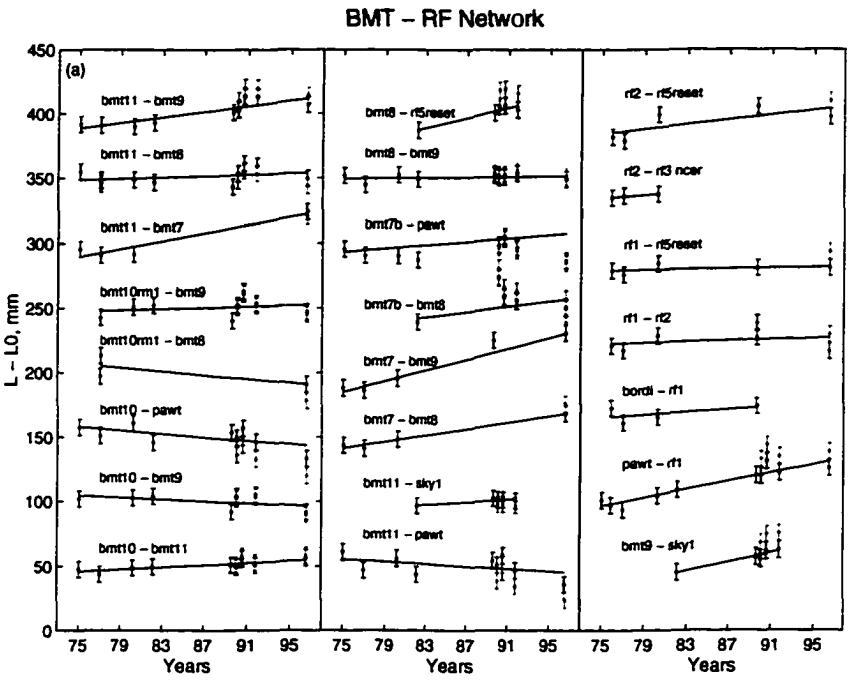

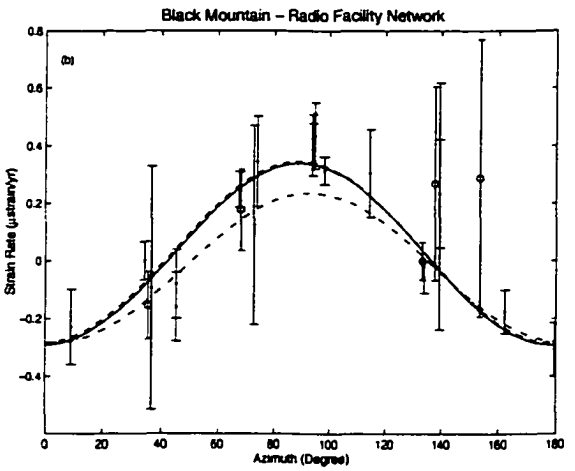

Figure 2.2. (a): Line length as a function of time for the Black Mountain-Radio Facility (BMT-RF) network. The error bars represent two standard deviations on either side of the plotted points. The grey points show the line lengths before correction for the coseismic and postseimic displacements of the 1989 Loma Prieta earthquake. (b): The best fit uniform strain tensor, shown in terms of the strain rate as a function of line azimuths in the Black Mountain (BMT), Radio Facility (RF) and its combined networks. The one standard deviation error bars with dot and circle show the observed strain rates in BMT and RF networks, respectively. Dashed line: BMT; Dot-dashed line: RF; Solid line: BMT-RF.

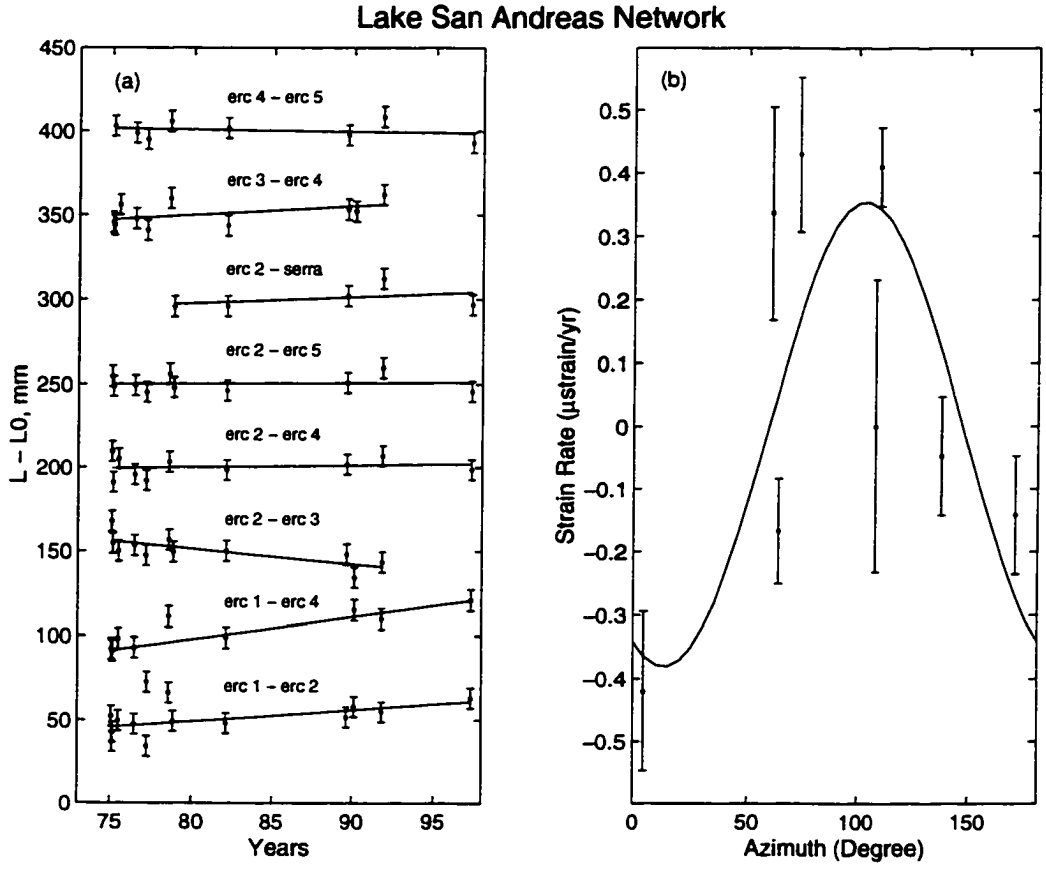

Figure 2.3. Same as Figure 2 for the Lake San Andreas network. We don't show the line lengths before correction for the coseismic displacements of the Loma Prieta earthquake, because the correction is too small to be distinguished in the figure.

correspond roughly to the depth at which large earthquakes nucleate (typically about 10-15 km in California). In the dislocation model, we assume that slip on the fault is zero down to depth D but is an amount V everywhere below that depth and use elastic dislocation theory to calculate the model displacement. Then the fault-parallel surface velocity v and the tensor shear strain rate $\dot{\varepsilon}_{xy}$ on the free surface are a simple function of the steady slip rate V, the locking depth D, and the distance x from the fault [*Savage and Burford*, 1973].

$$v = \frac{V}{\pi}\arctan(x/D) \tag{2.1}$$

$$\dot{\varepsilon}_{xy} = \frac{VD}{2\pi}(x^2 + D^2)^{-1} \tag{2.2}$$

Although the 2D uniform half-space screw dislocation model doesn't account for material heterogeneities, viscoelasticity, and other possibly important effects, it has predicted the deformation observed along much of the San Andreas fault system reasonably well. In this model, the strain rate is roughly constant over the range -$D \ll x \ll D$, so we can compare the strain rate at $x = 0$ with our estimated fault-parallel shear strain rate, as long as all sites are much closer to the fault than D (typically 10-15 km). At $x = 0$, we would expect $v = 0$ and $\dot{\varepsilon}_{xy} = \frac{V}{2\pi D}$.

Slip rates and locking depths for the segments of the SAF were taken from *WGCEP99* and are summarized in Table 2.2. Using equation (2.2), we calculated the expected strain rate from this 2D uniform half-space screw dislocation model (Table 2.2). The observed near-fault strain rates are significantly higher than what would be expected from the simple screw dislocation model in a uniform half-space, except for the Bodega-Tomales network which is almost exactly as predicted by the uniform half-space model. There are three possible explanations: The first is that *WGCEP99* has underestimated the fault slip rate or overestimated the locking depth. The second explanation is that the fault is creeping near the surface. This is unlikely because there has been no creep observed in the Penninsula, North Coast, and Santa Cruz Mountains segments of the SAF (see, *Lienkaemper* et al. [1991] Figure 1 for a summary of regional observations of creeping). The final possible explanation is that the uniform model does not account for significant changes in material properties near the fault. We will discuss the details later.

Table 2.2. Summary of Strain Rates for Each Network

Network	Observed strain rate μstrain/yr	Segments based on WGCEP	Slip rate† mm/yr	Locking depth† km	Expected strain rate‡ μstrain/yr	Rigidity ratio Fault width (km) 0.5	1	2.5	5
BMT	0.315±0.061	Santa Cruz Mtns	17±2	15±1	0.180	0.572	0.570	0.558	0.520
BMT-RF	0.316±0.060	Santa Cruz Mtns	17±2	15±1	0.180	0.570	0.568	0.556	0.520
Lake	0.366±0.095	Peninsula	17±2	13±1	0.208	0.568	0.565	0.549	0.501
Bodega*	0.429±0.134	North Coast South	24±1.5	11±1	0.347	1.000	1.000	1.000	1.000
Tomales*	0.333±0.025	North Coast South	24±1.5	11±1	0.347	1.000	1.000	1.000	1.000
Bodega-Tomales*	0.339±0.025	North Coast South	24±1.5	11±1	0.347	1.000	1.000	1.000	1.000

*Bodega-Tomales network can be predicted by a 2-D uniform model, so we don't apply 2-D inhomogeneous model, which would predict a higher strain rate.

†Slip rates and locking depths are from *WGCEP99*.

‡Expected from 2-D uniform half-space model.

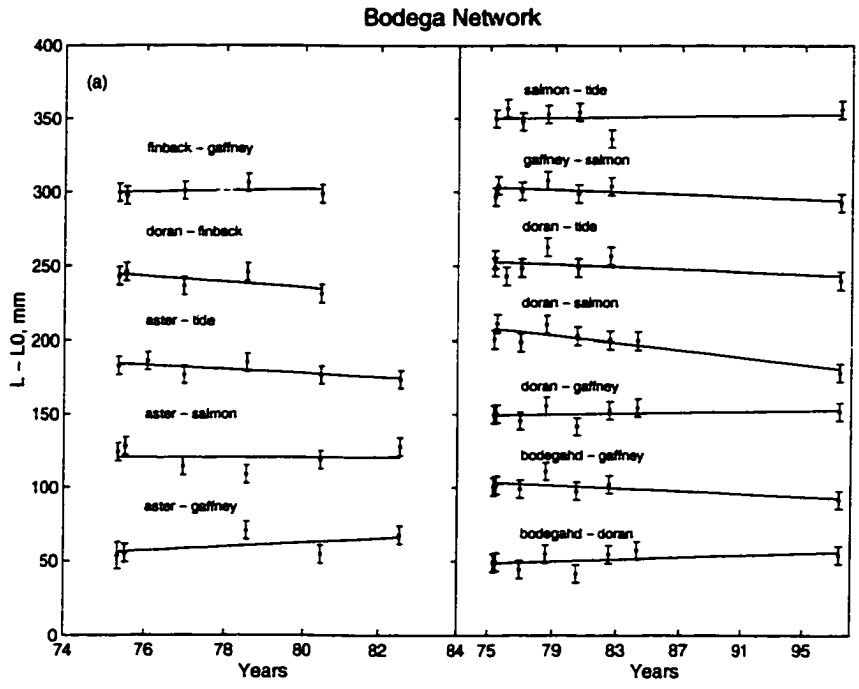

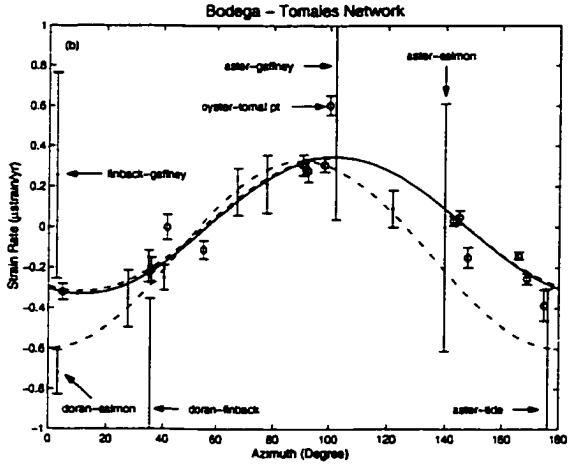

Figure 2.4. Same as Figure 2.2 for the Bodega network. (a): The Tomales network was surveyed only once by EDM and once by GPS, so the line lengths as a function of time are not shown. (b): Same as Figure 2.2b in the Bodega, Tomales and its combined networks. Dot: Bodega; Circle: Tomales; Dashed line: Tomales; Dot-dashed line: Bodega; Solid line: Bodega-Tomales. Two outlier lines and five lines with large uncetainties are labeled.

2.4.2 Locking Depth vs Seismogenic Depth

The long term slip rate V in equations (2.1) and (2.2) can be well determined from geodetic data and paleoseismic studies [*WGCEP99*, *Schwartz* et al., 1998; *Hall* et al., 1999; *Niemi and Hall*, 1992]. However, the geodetic locking depth is often poorly constrained and there can be a tradeoff between the estimated slip rate and locking depth if the data do not extend far away enough from the fault [e.g., *Johnson and Wyatt*, 1994], and the range of estimated locking depth from geodetic data could be very broad [e.g., *Freymueller* et al., 1999]. For example, based on the far-field geodetic data along the Black Mountain profile, the model of *Bürgmann* et al. [2000] shows a best-fitting locking depth of 10.5 km and a slip rate of 21.2 mm/yr on the SAF with a broad minimum mean square error [*Bürgmann*, personal communication, 2001]. This is comparable with the *WGCEP99* values.

The locking depth is often associated with the depth of the seismogenic zone. Some models, however, predict that at certain instants of time, the locking depth measured geodetically might be larger than the seismogenic depth. For example, *Savage and Lisowski* [1998] suggested that late in the earthquake cycle, the viscoelastic response of the lower crust could result in a geodetic locking depth that could be significantly greater than the seismogenic depth. Except in the immediate aftermath of a large earthquake, however, it has not been suggested that the geodetic locking depth should be shallower than the seismogenic depth. Thus, the seismogenic depth is probably a minimum estimate of the geodetic locking depth.

2.4.3 2-D Inhomogeneous Model

Geological and seismological evidence suggests the existence of a narrow fault zone with material properties different from the surrounding rock. The San Andreas fault at San Francisco Bay area separates very different types of basement rock. The east wall of the San Andreas fault is formed by Franciscan rocks, a melange that consists of a dismembered sequences of graywacke, shale, and lesser amounts of mafic volcanic rocks, thin-bedded chert, and rare limestone, while the west wall of the San Andreas fault mainly consists of granitic Salinian rocks and is overlain by Quaternary and Tertiary sediments [*Irwin*, 1990]. The amplitude and phase of lunar semi-diurnal tilt data derived from a site within 10 km of the San Andreas fault suggest a 3 km wide fault zone with lower shear modulus

[*Wood*, 1973]. Seismic tomography suggests that the change in seismic velocity at the fault is abrupt [*Mooney and Ginzburg*, 1986; *Lees and Malin*, 1990]. Fault-zone-guided waves observed along the San Andreas fault provide evidence for a highly fractured low-velocity fault zone. For example, at Parkfield, California the fractured zone is 100 to 150 meters wide with a very low shear wave velocity of 1.1 to 1.8 km/sec [*Li* et al., 1990]. Magnetotelluric and seismic reflection surveys at Parkfield image a vertical zone of low electrical resistivity about 500 m wide and 4000 m deep on the San Andreas fault zone [*Unsworth* et al., 1997].

Lisowski et al. [1991] presented a lateral inhomogeneous model with a narrow zone of compliant material near a fault to explain the abrupt inflection in the velocity profile at Point Reyes. In general, if a fault is embedded in a compliant (lower rigidity) zone, the use of a simple homogeneous elastic half-space model will result in an underestimate of the locking depth [*Rybicki and Kasahara*, 1977; *McHugh and Johnston*, 1977]. The difference between the homogeneous and inhomogeneous models will be most pronounced very close to the fault. When compared to a homogeneous elastic half-space model, an elastic model with a compliant zone surrounding the fault predicts very similar (slightly smaller) strains in the far field, but substantially higher strains near the fault [*Rybicki and Kasahara*, 1977; *McHugh and Johnston*, 1977].

We used the inhomogeneous model of *Rybicki and Kasahara* [1977] to calculate velocities and strain rates. Instead of considering the deformation during an earthquake as in *Rybicki and Kasahara* [1977], we focus on the interseismic deformation. We also found and corrected a misprint in *Rybicki and Kasahara* [1977] (see Appendix). Figure 2.5 shows a sketch of a two-dimensional vertical strike-slip fault in a laterally inhomogeneous medium with a low rigidity zone of width H surrounding a fault. μ_1, μ_2, and μ_3 are rigidity of the medium (Figure 2.5). We assume that $\mu_1 = \mu_3$. Assuming that there is no fault creep and the upper part of the fault is locked to a locking depth D, while below D the fault slips at a constant long-term slip rate V, we integrate equation (1) in *Rybicki and Kasahara* [1977] from D to infinity to obtain the velocity v parallel to the fault. The fault-parallel shear strain rate is simply dv/dx. The velocity and strain rate on the surface are given by:

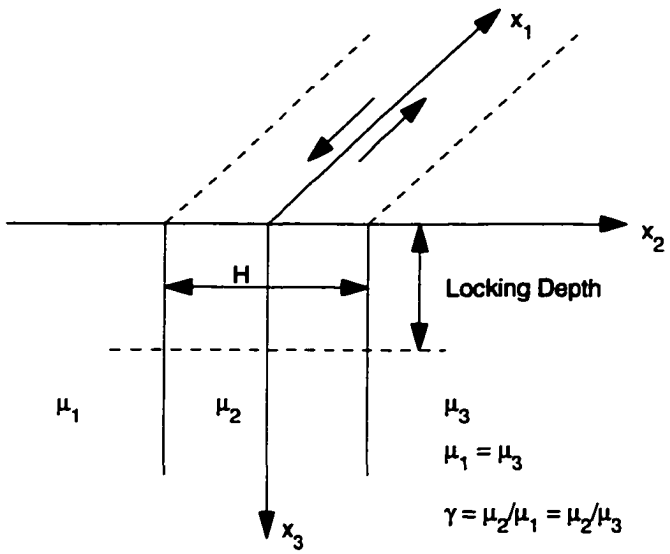

Figure 2.5. A two dimensional model in a laterally inhomogeneous medium. Two interfaces separate the medium into three parts, with rigidity μ_1, μ_2, and μ_3, respectively. We assume that $\mu_1 = \mu_3$.

When $0 \leq x \leq H/2$:

$$
\begin{aligned}
v &= \frac{V}{\pi}\left\{\arctan\frac{x}{D} + \sum_{m=1}^{\infty}\left[\left(\frac{\gamma-1}{\gamma+1}\right)^{2m-1}\left(\arctan\frac{D}{x+(2m-1)H} + \arctan\frac{D}{x-(2m-1)H}\right)\right.\right. \\
&\quad \left.\left. - \left(\frac{\gamma-1}{\gamma+1}\right)^{2m}\left(\arctan\frac{D}{x+2mH} + \arctan\frac{D}{x-2mH}\right)\right]\right\} \qquad (2.3) \\
\dot{\varepsilon}_{12} &= \frac{V}{2\pi}\left\{\frac{D}{x^2+D^2} - \sum_{m=1}^{\infty}\left[\left(\frac{\gamma-1}{\gamma+1}\right)^{2m-1}\left(\frac{D}{[x+(2m-1)H]^2+D^2} + \frac{D}{[x-(2m-1)H]^2+D^2}\right)\right.\right. \\
&\quad \left.\left. + \left(\frac{\gamma-1}{\gamma+1}\right)^{2m}\left(\frac{D}{(x+2mH)^2+D^2} + \frac{D}{(x-2mH)^2+D^2}\right)\right]\right\}
\end{aligned}
$$

When $x > H/2$:

$$
\begin{aligned}
v &= \frac{2V\gamma}{\pi(\gamma+1)}\left\{\arctan\frac{x}{D} - \sum_{m=1}^{\infty}\left[\left(\frac{\gamma-1}{\gamma+1}\right)^{2m-1}\arctan\frac{D}{x+(2m-1)H}\right.\right. \\
&\quad \left.\left. - \left(\frac{\gamma-1}{\gamma+1}\right)^{2m}\arctan\frac{D}{x+2mH}\right]\right\} \qquad (2.4) \\
\dot{\varepsilon}_{12} &= \frac{V\gamma}{\pi(\gamma+1)}\left\{\frac{D}{x^2+D^2} - \sum_{m=1}^{\infty}\left[\left(\frac{\gamma-1}{\gamma+1}\right)^{2m-1}\frac{D}{[x+(2m-1)H]^2+D^2}\right.\right. \\
&\quad \left.\left. - \left(\frac{\gamma-1}{\gamma+1}\right)^{2m}\frac{D}{(x+2mH)^2+D^2}\right]\right\}
\end{aligned}
$$

where V is the slip rate, D is the locking depth, x is the distance from the fault trace, H is the width of low rigidity zone, and $\gamma{=}\mu_2/\mu_1{=}\mu_2/\mu_3$ is the rigidity ratio. For $-H/2{\leq}x{\leq}0$ and $x < -H/2$, we can get the displacement and strain rate according to symmetry.

For $0{\leq}|x|{\leq}H/2$, the strain rate is larger than that predicted from the homogeneous model, and lower than the homogeneous model for $|x| > H/2$. That is, strain is concentrated within the near-fault compliant zone. If we take $\gamma{=}1$, equations (2.3) and (2.4) reduce to the homogeneous model (equations (2.1) and (2.2)).

We calculated the near-fault strain rates for all networks using this model, assuming slip rates and locking depths from *WGCEP99*. The width of the compliant zone is uncertain, so we try a range of widths (H): 0.5 km, 1 km, 2.5 km, and 5 km. The results of the inhomogeneous model are listed in Table 2.2. The observed strain rates in the BMT-RF and Lake San Andreas networks may be explained by an inhomogeneous model with a low rigidity compliant zone close to the fault if the rigidity of the fault zone is 50-60% that of the surrounding materials. A fault zone of <1 km width is probably the most realistic, but the estimated rigidity ratio is not sensitive to the assumed width unless the width of the fault zone is several kilometers. Because most sites are located 1-2 km away from the fault, we found very similar predicted strain rates for all models with $H < 2$ km, and cannot distinguish between models with different H.

2.5 Results

2.5.1 Black Mountain-Radio Facility Network

The BMT-RF network is located in the Santa Cruz Mountains segments [*WGCEP99*], and lies 44 km NW of the 1989 Loma Prieta epicenter. We used the models of *Árnadóttir and Segall* [1994] and *Bürgmann* et al. [1997] to remove the coseismic and postseismic effect of the 1989 Loma Prieta earthquake, respectively. Some lines crossing SAF were changed by up to ~14 mm and ~0.2 mm by the coseismic and postseimic deformation, respectively. Changes were smaller for the fault parallel lines. The near-fault tensor shear strain rate for the BMT-RF network would have been 0.462±0.063 μstrain/yr (instead of 0.316±0.060 μstrain/yr) without correcting for the effect of the Loma Prieta earthquake. After the correction, all baselines are well fit by a simple linear model in time (Figure 2.2a).

The 0.316±0.060 μstrain/yr observed tensor shear strain rate in the BMT-RF network (Table 2.2) is significantly higher than what we expect from a uniform model (0.180 μstrain/yr). A near-fault compliant zone offers a simple explanation for the high near-fault strain rate. Figure 2.6 shows the rigidity ratio required to explain the observed strain rate contoured as a function of the locking depth and slip rate. The rectangle shows the parameter values within two standard deviations of the locking depth and slip rate from *WGCEP99*. The rigidity ratio that would be inferred ranges between 0.37 and 0.81.

Another possible explanation is that *WGCEP99* may have underestimated the slip rate and/or overestimated the locking depth. However, the slip rate is well determined on the San Francisco Peninsula from geodetic data and paleoseismic studies [*WGCEP99*, *Schwartz* et al., 1998; *Hall* et al., 1999]. Assuming slip in a uniform elastic half-space, the observed strain rate in the BMT-RF implies a shallow locking depth, of the order of 8 km. The 1989 Loma Prieta earthquake model [*Árnadóttir and Segall*, 1994] implies substantial slip beneath 10 km depth. This is comparable with 15±1 km of seismogenic depth from *WGCEP99* and the model of *Bürgmann* et al. [2000] which predicts 10.5 km of locking depth and 21.2 mm/yr on SAF [*Bürgmann*, personal communication, 2001].

The best estimate of γ is determined by the best estimate for each input parameter. To estimate a realistic uncertainty in γ, taking $H = 1.0$ km, we assume that the errors of the observed strain rate, the locking depth, and the slip rate have Gaussian distributions,

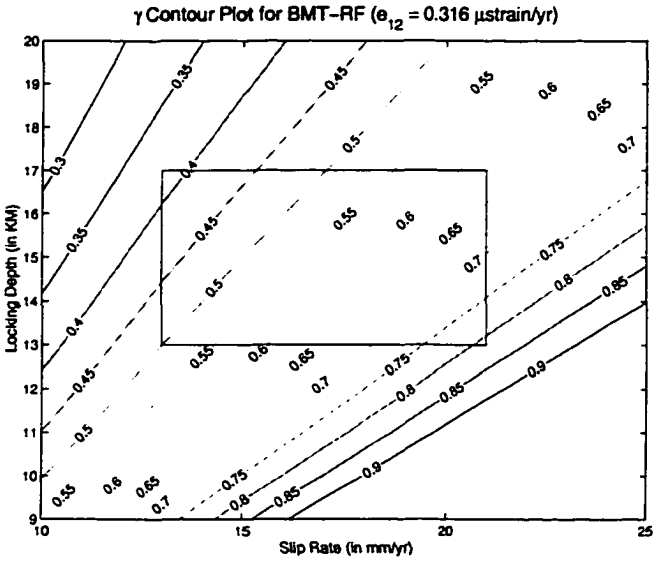

Figure 2.6. Rigidity ratio contoured plot for BMT0RF as a function of locking depth and slip rate. The rectangle shows the region within two standard deviations of slip rate and locking depth of the *WGCEP99* estimates

and run 10,000 models, choosing a random sample for each parameter in each model. We determine the two-sided confidence intervals at the 1-α level for γ by the percentile method in which the N estimated values are numerically ordered and the upper and lower limits are given by the Nα/2 and N(1-α/2) values, respectively, from the ordered list.

We estimate the rigidity ratio in the BMT-RF network and 95% confidence intervals to be $0.568^{+0.400}_{-0.202}$ (95% upper and lower confidence intervals are indicated by superscripts and subscripts). We can reject the hypothesis that the homogeneous model (γ=1) can fit the data at 95% confidence level, given the *WGCEP99* values for slip rate and locking depth.

The compliant zone surrounding the SAF in the BMT-RF network should correspond to a narrow low seismic velocity zone, such as the zone of low P velocity and high V_p/V_s ratio centered on the SAF at Loma Prieta [*Eberhart-Phillips and Michael*, 1998]. We estimate the rigidity of the fault zone to be about 60% of the surrounding materials. Assuming the density to be constant, the shear wave velocity in the fault zone should be about 80% of that away from the fault. A reduction in shear wave velocity of similar magnitude has been observed at Parkfield [*Li* et al., 1990] and Loma Prieta [*Eberhart-Phillips and Michael*, 1998].

2.5.2 Lake San Andreas Network

The Lake San Andreas network is in the Peninsula segment as defined by *WGCEP99*. The slip rate of the Peninsula segment is 17±2 mm/yr, and the locking depth is 13±1 km (Table 2.2) [*WGCEP99*]. We estimate the rigidity ratio in the Lake San Andreas network to be $0.565^{+0.212}_{-0.140}$ with 68.6% upper and lower confidence intervals. The 95% confidence region of 0.337-1.202 overlaps γ=1, the uniform half-space model. We can not reject the hypothesis of γ=1 at 95% confidence level although it is very likely that $\gamma < 1$.

2.5.3 Bodega-Tomales Network

The Bodega and Tomales networks are located in the North Coast South segment with slip rate 24±1.5 mm/yr and locking depth 11±1 km [*WGCEP99*]. These two networks were surveyed separately, but are adjacent (about 10 km apart along strike) and two lines (Bod head-tomal pt and Bod rml-tomal pt) connect them. We combined them as a single network. The observed tensor shear strain rate is 0.339±0.025 μstrain/yr for the combined Bodega-Tomales network, which is quite consistent with the uniform half-space model (Table 2.2). Here there is no evidence for strain concentration near the fault as long as the slip rate and locking depth were correctly estimated by *WGCEP99*.

We also analyzed the two networks independently to test whether the strain tensors were really the same in both networks, and because a few lines were not well fit by the uniform strain model. Considered independently, the shear strain rates in the Bodega and Tomales networks are 0.429±0.134 and 0.333±0.036 μstrain/yr, respectively (Table 2.2). The strain tensor solution for the Bodega network is suspicous, because it has a large uncertainty and has a large fault-parallel contraction component ($\dot{\varepsilon}_{22}$=-0.313 μstrain/yr). Five lines (finback-gaffney, doran-finback, aster-gaffney, aster-salmon, and aster-tide) have large uncertainties because the site Aster was destroyed around 1980 and finback could not be found.

The χ^2 for the solutions assuming uniform or separate strain tensors for the Bodega and Tomales networks are compared in Table 2.3. The total χ^2 of the models fitting the Bodega and Tomales networks separately does not improve significantly from the single combined model; an F-test shows that the improvement in χ^2 is not significant at the 95%

Table 2.3. Summary of the Model Fitness of Each Network

Network	Number of Data	Degree of Freedom	Weighted Residual Sum of Squares χ^2	F-ratio*	95% Confident Critical Value
BMT	18	15	12.47		
RF	5	2	1.14		
BMT-RF	23	20	16.61	1.25	3.20
Bodega	12	9	8.06		
Tomales	14	11	66.56		
Bodega-Tomales	26	23	90.10	1.38	3.10

*The F-ratio tests whether the reduction in χ^2 resulting from estimating a separate tensor for each network is significant.

confidence level. Thus we use the combined Bodega-Tomales network solution, although if more data were available for the Bodega network it is possible that the two networks should be considered separately. Several lines in the Bodega network have large uncertainties, and an additional survey with GPS would significantly improve the strain rate estimate for that network.

It is surprising that the shear strain rate in the Bodega-Tomales network can be explained by the 2D uniform model because the shear strain rate at Point Reyes, 20 km to the south, clearly shows a strain concentration near the fault [*Prescott and Yu*, 1986; *Lisowski* et al., 1991]. The reason for the different strain rate between the two nearby networks is unknown; we do note, however, that only two measurements of the Tomales network (EDM in 1983 and GPS in 1997) are available and we cannot know whether all of the measured line lengths are robust. One line, oyster-tomal pt, shows a significantly higher extension rate than predicted by the model (Figure 2.4b), although other lines of similar orientation are fit well. A repeat survey with GPS would improve the confidence in all of the Tomales network velocities.

2.6 Discussion

2.6.1 Compliant Zone or Shallow Locking Depth?

A very shallow locking depth (6-8 km) is required by the uniform model to explain the high shear strain rates observed in the BMT-RF and Lake San Andreas networks and at Point Reyes [*Prescott and Yu*, 1986]. This is inconsistent with past inferences from seismological and geodetic data. Inversion of geodetic data indicates that slip during the 1989 Loma Prieta earthquake occurred between 5 and 18 km depth [*Lisowski* et al., 1990; *Marshall* et al., 1991], and variable slip models concentrate the slippage below 10 km [*Árnadóttir and Segall*, 1994]. These are comparable with the seismological suggestion, which shows two main areas of concentrated slip at depths of 14 km and 12 km, northeast and southwest of the 1989 hypocenter, respectively [*Beroza*, 1991]. The 1906 earthquake slip models in the vicinity of Loma Prieta suggest the slip extends from the surface to 20 km depth [*Thatcher* et al., 1997]. More recently, *WGCEP99* estimated the seismogenic depths to be 13±1 and 15±1 km in the Peninsula and Santa Cruz Mountains segments, respectively.

We think that a near-fault compliant zone offers a simple explanation for the observations, and should be expected based on seismological data. However, if there is not a near-fault compliant zone, the 2D unform half-space model requires a very shallow locking depth to explain the high observed shear strain rates in the Peninsula and Santa Cruz Mountains segments of the SAF. In this case, estimates of seismogenic depths by *WGCEP99* would be wrong, and all inferences of *WGCEP99* using the seismogenic depths as input parameters also would be wrong.

2.6.2 Why Is the Fault Zone Compliant (But Not Everywhere)?

There is compelling evidence for a narrow compliant zone of concentrated shear strain in the BMT-RF, Lake San Andreas, and Point Reyes [*Lisowski* et al., 1991] networks, but not in the Bodega-Tomales network, or at Point Arena to the north [*Freymueller* et al., 1999]. Why and how does a near-fault compliant zone develop? Is it peculiar to the SAF or a general feature of all strike-slip faults once they have a large enough offset? That is, does this near-fault compliant zone develop because of the lithologies on either site of the fault, or simply from repeated slip on the fault over time? In much of northern and central

California, the Salinian block of granitic and metamorphic rocks form the west wall of the SAF while the Franciscan assemblage and overlying strata of the Great Valley sequence form the east. The Franciscan is a heterogeneous assemblage that consists of graywacke, shale and lesser amounts of mafic volcanic rocks and rare limestone [*Irwin*, 1990]. The Salinian block extends northward to the Bodega Bay network. Further northward, from just beyond Bodega Head to Point Arena, it is questionable whether the rocks along the fault are Salinian block or not [*Wentworth*, 1968]. The narrow compliant fault zone may be related to the lithologies juxtaposed by the fault.

Another possible reason for the developing of a near-fault compliant zone is that as the fault becomes older, the intrafault material that controls the failure characteristics becomes increasingly broken up, and its elastic properties may be changed. The role of this intrafault material (both fault gouge and highly fractured rocks) in controlling the failure characteristics of rocks is a function of mineralogy, temperature and pressure [*Brace*, 1972; *Byerlee* et al., 1978]. Because of variations in temperature and mineralogical composition and the complex structure of the fault zone, the geometry of a fault zone varies greatly both in vertical direction and along the fault. There are in general several zones of fault gouge or crushed rock. Water will flow into the highly porous and permeable fault zone until the balance of the pore pressure in the fault zone and the hydrostatic pressure in the country rock [*Byerlee*, 1993]. The high porosity of fluids may result in the low electrical resistivity at Parkfield [*Unsworth* et al., 1997] and lower seismic velocities northeast of the San Andreas fault [*Lees and Malin*, 1990].

Such a zone would be characterized by low rigidity, low resistivity and low P velocity. The high fluid pressure would reduce P velocity and increase the ratio of P velocity to S velocity. High V_p/V_s implies lower rigidity. All of these were observed at Loma Prieta [*Eberhart-Phillips and Michael*, 1998]. A 10% decrease in S velocity corresponds to 20% decrease in rigidity. The development of a near-fault low rigidity compliant zone may be associated with highly porous and permeable fault gouge zone [*Unsworth* et al., 1997; *Byerlee*, 1993; *Lees and Malin*, 1990] and the brittle/plastic transition [*Scholz*, 1988].

The geodetic data in this study suggested a compliant zone along the SAF in San Francisco Bay area, possibly extending from Point Reyes in the north to Loma Prieta in the south. The compliant zone becomes more pronounced to the south. This suggests that

both the materials on either side of the fault and the cumulative fault offset may play a role in the development of the compliant zone. We do not have a clear explanation for why the rigidity ratio changes so suddenly near Point Reyes.

2.6.3 Implications for Seismic Hazard Estimation

Biased Estimates of Slip Rates and Locking Depth

We have shown that a narrow low rigidity zone surrounding the fault can explain the concentration of strain in the BMT-RF and Lake San Andreas networks. Estimates of slip rates and/or locking depths from geodetic data would be biased if we do not account for the differing elastic properties across the fault. Here we do two tests to investigate how the slip rate and locking depth would be biased using a homogeneous model to fit synthetic data generated by the inhomogeneous model: (1) assume the locking depth and estimate the slip rate; (2) estimate both locking depth and slip rate.

Given the slip rate, locking depth, and our estimates of rigidity ratio for the BMT-RF network in Table 2.2 ($H = 1$ km), using the 2D inhomogeneous model we predict 64 surface velocities at different distances from the fault as our "observed" data. 32 of the sites were in the distance of $|x| \leq D$, and the others were in the range of $D < |x| < 6.3D$. We chose the distance up to $6.3D$ to capture 90% of the plate motion [*Lisowski* et al., 1991]. This synthetic network is more dense than most real networks, but we can easily consider subsets of this data set.

If the locking depth is assumed to be known, the slip rates are linearly related to the surface velocites (Equation (2.1)). We estimated the slip rate from the synthetic data using standard linear squares methods. The estimate of the slip rate in the BMT-RF was 17 mm/yr, indistinguishable from the input value, which implies that the estimate of the slip rate is not sensitive to near fault material preperties. This is because it is more sensitive to the far field data than to the near field. However the 32 data within $|x| \leq D$ contributed 91% of residuals in this inversion, suggesting that a slip rate estimated from only near-fault data could be biased if we do not count for the variations in material properties across the fault.

We also considered the case in which we estimated both the slip rate and locking depth.

In this case, the relationship between surface velocities and the locking depth is nonlinear. We use the random cost nonlinear optimization technique [*Berg*, 1993; *Freymueller* et al., 1999; *Cervelli* et al., 2001] to estimate both slip rate and locking depth. The result suggested that we underestimated the true locking depth by about 10%. However, the estimate of slip rate 17 mm/yr was again unaffected. The estimate of the locking depth is most sensitive to the near fault data. This suggests that the major impact of the differing elastic properties near the fault is on estimates of the locking depths, and locking depths estimated from geodetic data may be underestimated if a near-fault compliant zone is present but unmodeled.

Moment Deficit Rate

Seismogenic (locking) depths and fault slip rates are fundamental inputs to seismic hazard analysis. One measure of seismic potential is the seismic moment deficit rate $\dot{M}_0$ for per unit length of a fault, defined by

$$\dot{M}_0 = \mu V D$$

Here μ is the shear modulus, V is the fault slip rate, and D is the locking depth. $\dot{M}_0$ may be obtained either from geodetic or seismic data. For the half-space uniform model, according to equation (2.2), the moment deficit rate on the fault can also be written $\dot{M}_0 = 2\pi\dot{\epsilon}_{xy}D^2$.

Well-known slip rate and locking depth are needed to estimate the moment deficit rate. If we do not account for the differing elastic properties of a fault zone, a high near-fault shear strain rate would require a very shallow locking depth so that we might mis-estimate the seismic potential if a near-fault compliant zone is present but unmodeled. If the slip rate and locking depth are estimated from far-field geodetic data, underestimation of the locking depth may contribute to an underestimation of $\dot{M}_0$. If, however, the near-fault strain rate is used, the high strain rate that results from strain concentration would lead to an overestimation of $\dot{M}_0$.

2.7 Conclusion

A combination of GPS and EDM measurements in five small-aperture geodetic networks along the San Andreas fault in northern California were used to estimate the near-fault strain rate. The observed tensor shear strain rate increases systematically from the Black Mountain-Radio Facility network to the north before reaching the Tomales Bay, and then decreases to further north at Point Arena. On the San Francisco Peninsula, near-fault strain rates are higher than that expected from a uniform half-space with the slip rate and locking depth used in *WGCEP99*. In contrast, the strain rate of the Bodega-Tomales network is as expected from a uniform model.

The pronounced shear strain near the fault in the BMT-RF and Lake San Andreas networks can alternatively be explained by a 2D uniform half-space model with shallow locking depth (~7-8 km) or a model in which a low rigidity compliant zone surrounds the fault. Such a shallow locking depth is unlikely based on the seismological evidence, but cannot be ruled out. A shallow locking depth would lead us to underestimate the seismic moment released by this segment of the SAF. We prefer the material heterogeneity model, as there is substantial evidence for near-fault compliant zone on several segment of the SAF. The width of the low rigidity zone is not well constrained by the data, but is most likely less than 2 km wide. Within this zone at Black Mountain, the rigidity is roughly 60% of that outside the fault zone. At Lake San Andreas, the rigidity within the fault zone is between 50-100% of the rigidity outside of the fault zone. At Tomales Bay and Bodega Bay there is no evidence for a low rigidity zone surrounding the fault. The rigidity change at Black Mountain would result in a seismic low velocity zone surrounding the fault. The change in rigidity is consistent with the change in seismic wave velocity and resistivity observed in the fault zone at Loma Prieta and Parkfield, further to the south along the San Andreas fault, resulting in a low-resistivity (3-10 ohm-m) and a low P wave velocity of 3.3-5.8 km/s at Loma Prieta [*Eberhart-Phillips* et al., 1990] and a shear wave velocity of 1.8 km/sec at Parkfield [*Li* et al., 1990].

The decrease in rigidity contrast to the north suggests that the age of the fault may play a role in the development of the low rigidity zone. However, the materials on each side of the fault may also play a role. Past work shows evidence for a low rigidity zone at Loma

Prieta and Olema (southern Point Reyes Peninsula), while only 25-50 km to the north the Tomales network shows no evidence for a low rigidity zone.

2.8 Appendix

We found a misprint in equation (A4) in *Rybicki and Kasahara* [1977] (p. 137) in the course of our study. A ")" was missing and two terms of "$(x_2+2mH+y_2)^2$" should be "$(x_2+2mH-y_2)^2$" in their equation (A4). The corrected equation (A4) is listed below:

$$
\begin{aligned}
G_1^1(P,Q) \;=\; & -\frac{1}{2\pi\mu_2}\left\{\log\sqrt{(x_2-y_2)^2+(x_3-y_3)^2}+\log\sqrt{(x_2-y_2)^2+(x_3+y_3)^2}\right. \\
& +\sum_{m=1}^{\infty}\left[\left(\frac{\mu_2-\mu_1}{\mu_2+\mu_1}\right)^m\left(\frac{\mu_2-\mu_3}{\mu_2+\mu_3}\right)^{m-1}\left(\log\sqrt{[x_2+(2m-1)H+y_2]^2+(x_3-y_3)^2}\right.\right. \\
& \left.+\log\sqrt{[x_2+(2m-1)H+y_2]^2+(x_3+y_3)^2}\right)+\left(\frac{\mu_2-\mu_3}{\mu_2+\mu_3}\right)^m\left(\frac{\mu_2-\mu_1}{\mu_2+\mu_1}\right)^{m-1} \\
& \times\left(\log\sqrt{[x_2-(2m-1)H+y_2]^2+(x_3-y_3)^2}\right. \\
& \left.+\log\sqrt{[x_2-(2m-1)H+y_2]^2+(x_3+y_3)^2}\right) \\
& +\left(\frac{\mu_2-\mu_1}{\mu_2+\mu_1}\right)^m\left(\frac{\mu_2-\mu_3}{\mu_2+\mu_3}\right)^m\left(\log\sqrt{(x_2+2mH-y_2)^2+(x_3-y_3)^2}\right. \\
& +\log\sqrt{(x_2+2mH-y_2)^2+(x_3+y_3)^2}+\log\sqrt{(x_2-2mH-y_2)^2+(x_3-y_3)^2} \\
& \left.\left.\left.+\log\sqrt{(x_2-2mH-y_2)^2+(x_3+y_3)^2}\right)\right]\right\}
\end{aligned}
$$

2.9 Acknowledgments

We thank numerous landowners in the field areas for granting permission for us to resurvey sites. We also thank Paul Segall of Stanford University and Roland Bürgmann (then at UC Davis) for loaning GPS receivers, batteries, and fence-building materials. Chuck Stiffler and Gary Hamilton of the USGS Menlo Park provided valuable assistance in finding some of the sites, and Karen Wendt of the USGS found all of the old data and programs for us. We thank J. C. Savage, W. H. Prescott, and Roland Bürgmann for providing useful reviews, which improved the manuscript. This research was supported by USGS NEHRP Grant 1996-HQ-G02740.

Chapter 3

Active Deformation in Southern Tibet Measured by GPS[1]

3.1 Abstract

We use the Global Positioning System (GPS) to study present-day active deformation in southern Tibet. GPS data from 32 sites (three are permanent sites) in southern Tibet and Nepal surveyed between 1991 and 2001 reveal that the total extension rate between Shiquanhe and Lhasa is 13±1 mm/yr in the N110°E direction, and that this extension is spatially non-uniform. One-half of the extension occurs across the Yadong-Gulu rift with an opening rate of 6.5±1.5 mm/yr. Differential velocities of sites north and south of the Yarlung-Zangbo suture in western Tibet imply that the suture or an adjacent structure may be active as a strike-slip fault. A numerical model suggests that right-lateral strike slip on the Yarlung-Zangbo suture may extend from the Karakorum Fault Zone in the west to the Yadong-Gulu rift in the east with ~3 mm/yr slip rate, accommodating part of the eastward extrusion of Tibet. The spatially non-uniform extension in southern Tibet results from local faulting, such as the Yadong-Gulu rift and Yarlung-Zangbo suture. The convergence directions inferred from GPS are consistent with slip vectors of earthquakes, however, the rates of slip of India beneath Tibet along the Himalaya are different with a lower rate of

[1]Manuscript in preparation with authors Q. Chen, J. T. Freymueller, Z. Yang, C. Xu, W. Jiang, Q. Wang, and J. Liu

12.4±0.4 mm/yr between the longitudes of 83°E and 88°E, and 17±1 and 19±1 mm/yr in the western and eastern Himalaya, respectively. The variable slip rate results from variation in the deformation rate of the overriding Tibetan crust. We infer that the low convergence rate in the central Himalaya is significant.

3.2 Introduction

The Tibetan plateau lies between the Indian and Eurasian plates, and is a complex region with many earthquakes and active faults [*Molnar and Lyon-Caen*, 1989; *Rothery and Drury*, 1984; *Armijo* et al., 1986]. The motion of India relative to Eurasia is now constrained by geologic data (NUVEL-1A) [*DeMets* et al., 1990, 1994] and geodetic data [*Freymueller* et al., 1996; *Larson* et al., 1999; *Sella* et al., 2002], but Tibet is also moving significantly relative to Eurasia [*Armijo* et al., 1986, 1989; *Molnar and Tapponier*, 1975; *Harrison* et al., 1992; *Molnar*, 1984, 1990; *Molnar and Chen*, 1983] and undergoing significant internal deformation [*Rothery and Drury*, 1984; *Molnar and Lyon-Caen*, 1989; *Yin* et al., 1999] (also see chapter 4). According to the NUVEL-1A model [*DeMets* et al., 1990, 1994], the NNE movement of India towards Asia is approximately 50 mm/yr. More recently, newer data from space geodesy show a lower rate of 35-40 mm/yr between India and Eurasia [*Sella* et al., 2002; *Wang* et al., 2001]. About 17±2 mm/yr of convergence occurs in the Himalaya [*Bilham* et al., 1997], and two thirds of the convergence is distributed over a region extending north to Siberia. To understand the internal deformation in southern Tibet it is necessary to understand both the present kinematics and the development of the Himalaya and Tibetan Plateau.

In this chapter, we use Global Positioning System (GPS) data to study the internal deformation of southern Tibet. Seventeen GPS sites in southern Tibet surveyed between 1991 and 2001 [*Wang* et al., 2001] show that the rate of roughly east-west (N110°E) extension across southern Tibet is spatially variable and a large part of the extension is accounted for by the opening of the Yadong-Gulu rift. Two GPS sites velocities near Saga in southwestern Tibet (WT12 and SHOT, Figure 3.1) show strong evidence for right-lateral strike slip motion along the Yarlung-Zangbo suture, suggesting that strike slip motion along the Yarlung-Zangbo suture may contribute some parts of the east-west extension in southern

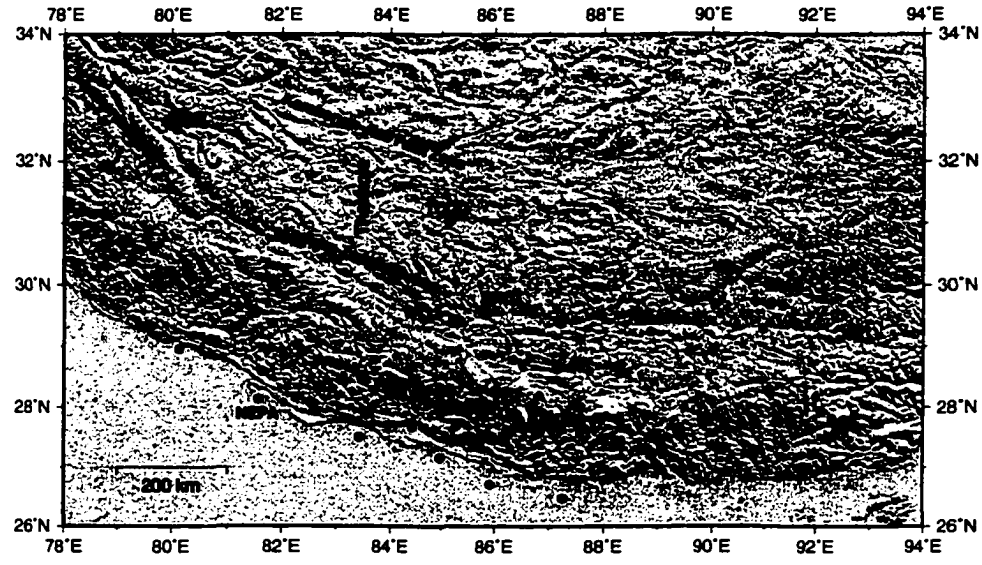

Figure 3.1. Map showing the sites used in southern Tibet. Circles: compaign sites; Triangle: permanent sites. YD is Yadong-Gulu rift.

Tibet.

3.3 Tectonic Background

Field investigations [*Tapponnier* et al., 1981; *Armijo* et al., 1986, 1989; *Burchfiel* et al., 1991; *Mercier* et al., 1987], Landsat images interpretation [*Rothery and Drury*, 1984] and earthquake fault plane solutions [*Molnar and Deng*, 1984; *Molnar and Lyon-Caen*, 1989] imply that north-south trending normal faulting characterizes the present tectonics of southern Tibet. Seven rift systems with a regular pattern, a few hundred kilometers long and about 200 km apart, extend north from the Himalaya and can be identified mostly south of latitude 32°N [*Armijo* et al., 1986]. On average, the normal faults trend N5.9°E ± 7.5°. The dips of the normal faults are between 45° and 60°. Among these normal faults, the Yadong-Gulu rift, which extends about 500 km from Yadong in the Himalaya to Gulu, is the longest and most continuous rift system in southern Tibet. A series of north-south trending rift sys-

tems cross the Tethyan Himalaya and cut the Yarlung-Zangbo suture (YZS) which broadly coincides at the surface with the Yarlung-Zangbo river.

A broad zone of *en échelon* right-lateral strike slip faults at about latitude 32°N, termed the Karakorum-Jiali Fault Zone (KJFZ) by *Armijo* et al. [1986], separates the well-developed normal faulting in southern Tibet from diffuse extension in central and northern Tibet. These faults trend 120-140°. *Armijo* et al. [1989] proposed that the Tibetan Plateau north of the KJFZ and south of the left-lateral Altyn Tagh fault was relatively undeforming and was extruding rapidly to the east. In contrast, based on interpretation of Landsat images, *Rothery and Drury* [1984] suggested that E-W extension, strike-slip and normal faulting extend throughout the Tibetan Plateau, and that the N-S shortening within the plateau could be about one-third of the total convergence between India and Eurasia. *Chen et al.* [Chapter 4] confirmed this interpretation, and attributed fast eastward extrusion of Tibet to deformation within the plateau (E-W extension and N-S shortening).

3.3.1 Yarlung-Zangbo Suture

The Yarlung-Zangbo suture in southern Tibet is the Tertiary suture that marks the boundary between rocks of Eurasian and Indian origin following the Late-Cretaceous-early Tertiary closure of the neo-Tethys [*Burg* et al., 1984; *Ni and Barazangi*, 1984]. Many tectonic models agree that early convergence between India and Eurasia took place along the YZS, and the suture closed during the Late Cretaceous-Eocence [*Seeber* et al., 1981; *Molnar and Chen*, 1982; *Barazangi and Ni*, 1982].

Whether the suture is active or not while the convergence between India and Asia is ongoing is still debatable. The linearity of the YZS and the steeply dipping faults accompanying it [e. g., *Tapponnier* et al., 1981] indicate that the suture is a steeply dipping zone [*Burg* et al., 1984] and that post-collision strike-slip movement along the suture may have been large [*Tapponnier* et al., 1981; *Burg* et al., 1984; *Tapponier* et al., 1986]. Although the strike-slip offset along the suture is unknown, *Tapponier* et al. [1986] suggested the YZS was active as a strike-slip shear zone with many kilometers of right-lateral offset in the Oligo-Miocene. The suture is not marked by continuous young fault traces except in the northwest where the suture appears to be a continuation (to about 86°E) of the active Karakorum Fault [*Tapponnier* et al., 1981; *Rothery and Drury*, 1984; *Tapponier* et al., 1986]. However,

based on field and radiometric data, *Ratschbacher* et al. [1994] argued that strike-slip faults along the YZS near Xigatse (near 89°E) may have been active recently. Wide-angle seismic data from Project INDEPTH (International Deep Profiling of Tibet and the Himalayas) suggest a prominent subhorizontal reflector, named the "Yarlung Zangbo reflector (YZR)", beneath the outcrop position of the YZS [*Makovsky* et al., 1999; *Alsdorf* et al., 1998; *Zhao* et al., 1997]. The YZR has been modeled as a fault or shear zone [*Zhao* et al., 1997; *Alsdorf* et al., 1998], but this model could not explain the high velocities observed on the YZR. *Makovsky* et al. [1999] interpret the YZR as an ophiolitic nappe complex and argue that the continuity of the YZR as a precollisional to syncollisional lithological unit excludes significant postcollisional strike-slip or steep-dip displacements along the YZS.

3.3.2 Yadong-Gulu Rift

The Yadong-Gulu rift is the longest and most continuous normal fault system in Tibet, extending from Yadong in the Himalaya to Gulu where it is linked to the Jiali Fault and other northwest trending strike-slip faults [*Armijo* et al., 1989]. From south to north, the rift extends across several major geologic zones: The Tethys Himalaya, the Yarlung-Zangbo suture, the Lhasa block, and the Nyainqentanglha range [*Armijo* et al., 1986]. The overall trend of the rift is about N30°E (Figure 3.1).

Armijo et al. [1986] divided the Yadong-Gulu rift into three geologic subsections: south of the YZS where normal faults dominate and dip to the west; between the suture and Nyainqentanglha range, where the rift is nearly symmetrical with faults dipping east and west; along the Nyainqentanglha range, where major faults dip to the east and have a large component of left-lateral movement (Figure 3.1). Several ductile high strain shear zones have been identified in the southern and northern Yadong-Gulu rift [*Pan and Kidd*, 1992; *Harrison* et al., 1995; *Kidd* et al., 1995; *Burchfiel* et al., 1991]. The locations and the shear sense of these localized high strain zones are probably associated with the opening of the Yadong-Gulu rift [*Cogan* et al., 1998]. The opening of the rift is being accommodated at depth by flow in the middle crust [*Cogan* et al., 1998]. This fluid behavior may be a consequence of the middle crust being partially molten suggested by INDEPTH data [*Nelson* et al., 1996].

3.3.3 Extension rate in Southern Tibet

Seismicity [*Molnar and Lyon-Caen*, 1989; *Ni and Barazangi*, 1984] and active north-south trending graben systems [*Armijo* et al., 1986] show that significant east-west extension occurs in the Himalaya and southern Tibet. The rate of extension across southern Tibet was estimated as 5-10 mm/yr by *Baranowski* et al. [1984] and 18±9 mm/yr in ~N115°E by *Molnar and Lyon-Caen* [1989] from seismic moment release in earthquakes. From geologic mapping and Landsat images interpretation, *Armijo* et al. [1986] estimated a rate of extension of 1.4±0.8 mm/yr along the Yadong-Gulu rift system and multiplied this by 7, the number of grabens in southern Tibet, and reached a 10±5 mm/yr extension rate in southern Tibet assuming spatially uniform extension. Since the westernmost graben is near 80°E, their estimate of 10±5 mm/yr ignores extension farther west, which was included in the estimate of *Molnar and Lyon-Caen* [1989]. The observation of ductile detachment faults along the Yadong-Gulu rift implies that the rift as a whole may have accommodated substantially greater extension than estimated by *Armijo* et al. [1986]. If the other rifts in southern Tibet are similarly bounded by ductile detachment faults, then the total EW extension across the Tibetan Plateau may be an order of magnitude greater [*Cogan* et al., 1998].

All of the estimated rates based on the geological and seismic data are highly uncertain. More recently, based on six years of GPS data in Nepal and southern Tibet, *Larson* et al. [1999] observed east-west extension across southern Tibet at a rate of 11±3 mm/yr between northwestern Nepal and Lhasa, which is in good agreement with the geologic estimate for the same region [*Armijo* et al., 1986], however, given the available site spacing, *Larson* et al. [1999] could not determine whether the extension was uniform or variable in space.

3.3.4 Convergence Rate Between Tibet and India

Previous studies estimated the long-term convergence rate to be in the range of 10-25 mm/yr across the Himalaya from geological and seismic evidence: geologic field observations [*Armijo* et al., 1986], seismic moment release rate for major thrust events in 80 years since 1900 along the Himalayan arc [*Molnar and Deng*, 1984], inversion of profiles of uplift rates [*Molnar*, 1987], and changes in the age of basal sediments in the Ganga basin over the last

10-20 Ma [*Lyon-Caen and Molnar*, 1985]. However, all these estimates were based on some assumed features, such as the assumed dating for geologic estimate and assumed rupture zone for seismic estimate, and yielded large uncertainties. Geodynamic models [e.g., *Shen* et al., 2001a] suggested a similar rate of ~20 mm/yr, however, based on the assumed rate of ~50 mm/yr of relative motion between India and Eurasia, which has been suggested to be ~10 mm/yr lower by *Sella* et al. [2002] based on geodetic data.

More recently, precise GPS geodesy suggested a convergence rate of ~18 mm/yr [*Bilham* et al., 1997; *Larson* et al., 1999]. *Larson* et al. [1999] presented a set of dislocation models for the Himalaya to interpret six-year GPS observations. Most of the sites they used were in Nepal. Several sites were in southern Tibet but within several tens of kilometers from the Himalaya. Their models did not fit the data from Lhasa within 95% confidence limits, because their models did not include the internal deformation of southern Tibet, but they did explain the data from Nepal satisfactorily. In this chapter, new data from southern Tibet allow us to model not only the Himalaya thrust but also the internal deformation of southern Tibet. We find that significant modifications to *Larson et al.*'s [1999] models are required by these new data. We also show the convergence rate in central Himalaya to be significantly lower than previous geodetic estimates [*Bilham* et al., 1997; *Larson* et al., 1999], and this rate may vary along the Himalayan arc.

3.4 Measurement and Analysis

3.4.1 GPS Observations

A total of seventeen GPS sites lie within a roughly N110°E transect about 1400 km long and 660 km wide in southern Tibet, extending from east of Lhasa west almost to the Karakorum fault (Figure 3.1). All data were measured between 1991 and 2000 through the collaborative efforts of researchers from the United States and China. Most measurements were in campaign style, with each survey lasting two or more days at each site. Fifteen sites in Nepal from *Larson et al.* [1999] are also included in this study. 1998-2000 observations at sites AIRP, NAGA, NAMC, and NEPA in Nepal are used here, which were not available to *Larson et al.* [1999]. Table 3.1 lists the locations of all the sites in southern Tibet, along with their temporal span. All these data were combined together with data from many

other sites in China, producing a self-consistent velocity field with a total of 354 sites in and surrounding China [*Wang* et al., 2001]. We use a subset of an improved version of the velocity field of *Wang* et al. [2001], and only discuss the 32 sites in Nepal and southern Tibet (Table 3.1).

A few small updates and changes have been made in the velocity solution of *Wang* et al. [2001]. We fixed antenna height errors at some sites, fixed a reference clock problem that biased a few solutions, excluded a few outlier measurements, and included more available data from regional permanent sites. About 60% of the solutions used in *Wang* et al. [2001] were improved in some way.

3.4.2 GPS Data Analysis

The GPS data in this chapter were analyzed using the GIPSY/OASIS II software (release 6) developed at the Jet Propulsion Laboratory [*Zumberge* et al., 1997; *Gregorius*, 1996]. Raw GPS data collected in the field were analyzed in 24-hour daily solutions along with regional and global permanent sites. Two types of GPS solutions were used in this study. For data prior to 1996, global GPS solutions were estimated using all data from Tibet, along with a well-distributed set of global sites. Satellite orbits were estimated in these solutions. The selection of global sites varied with time as the global GPS network grew. Prior to 1994, all global sites were included in the solutions. For the data after 1996, we used regional solutions by combining campaign data with a regional set of permanent sites and used fixed orbits obtained from JPL's submission to the IGS. For more details, refer to *Larson* et al. [1997] and *Freymueller* et al. [1999, 2000].

Each daily solution was then transformed into the ITRF97 reference frame. Finally, the individual daily GPS solutions were combined together to determine site velocities. The coordinates in the ITRF97 reference frame and their covariance matrix from the daily GPS solutions are used in a standard weighted least squares fit to estimate site positions at epoch 1995.0 and site velocities. The complete velocity field of 354 sites was presented in *Wang* et al. [2001]. We only discuss results from the sites listed in Table 3.1 and sites in Nepal.

For ease of interpretation, we express our velocities either relative to Xigatse (XIGA) or the Indian plate by subtracting the motion of XIGA or the Indian plate relative to the ITRF97 reference frame, respectively. We use the REVEL model [*Sella* et al., 2002] to

Table 3.1. GPS Sites Observed in southern Tibet

Site	ID	Latitude deg	Longitude deg	Height m	Observation First	Observation Last	Agency
Bala	BALA	29.7361	90.7979	3808.0259	1991.23	2000.43	UAF-Xi'an[1]
Dagze	DAGZ	29.6633	91.3634	3648.4792	1991.23	1998.68	UAF-Xi'an
Gongbu	GNGB	29.8808	93.2366	3504.5696	1998.64	2000.45	UAF-Xi'an
Gonggar	GGAR	29.2780	90.9588	3551.5462	1998.63	2000.44	UAF-Xi'an
Guoco	GUCO	28.7828	86.3401	4368.7148	1998.70	2000.49	UAF-Xi'an
Hotspring	SHOT	29.5911	85.7409	5019.4474	1998.70	2000.48	UAF-Xi'an
Jiangze	JIAN	28.9142	89.5728	3981.2922	1993.49	1998.70	SSB[2]
Lhasa	LHAS	29.6573	91.1040	3629.1804	1995.43	2000.50	IGS[3]
Lhaze	LAZE	29.1181	87.5766	3982.6581	1998.69	2000.41	UAF-WTUSM[4]
Nyalam	WT11	28.2938	86.0231	4166.3135	1993.63	1997.47	WTUSM
Rongbuk	RONG	28.1936	86.8271	4826.2595	1991.25	1998.69	UAF-Xi'an
Saga	WT12	29.4414	85.2140	4652.1091	1993.62	2000.42	WTUSM
Shiquanhe	SHIQ	32.5092	80.0984	4273.7805	1994.66	1999.45	SSB
Tcoqin	TCOQ	31.0186	85.1392	4654.3968	1998.69	2000.47	UAF-Xi'an
Tingri	TING	28.6293	87.1552	4179.5693	1991.25	1998.68	UAF-Xi'an
Xigaze	XIGA	29.2498	88.8643	3867.3193	1991.27	1998.43	UAF-WTUSM
Yadong	WT15	27.4887	88.9055	2927.8000	1997.46	2000.42	WTUSM, SSB

1. University of Alaska Fairbanks, USA and Chang'an University, China.

2. State Seismological Bureau of China.

3. International Geodetic Service.

4. Wuhan Technical University of Surveying and Mapping (now Wuhan University).

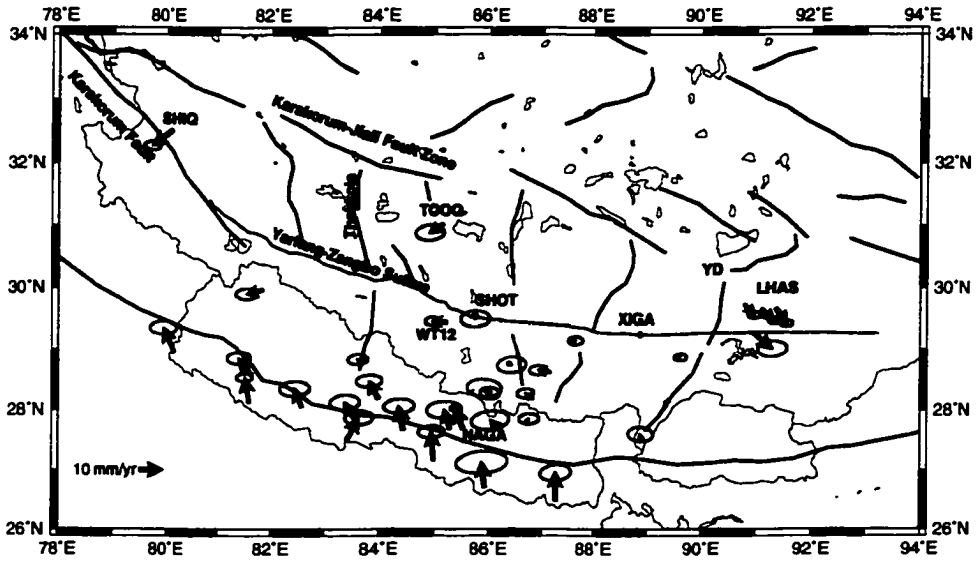

Figure 3.2. GPS velocities 1991-2001 in southern Tibet and Nepal, relative to Xigatse (XIGA). Xigaste is shown as a solid square. Uncertainties are 95% confidence ellipses.

define an India-fixed reference frame in this study. The uncertainty in the REVEL model, based on propagation of the full REVEL covariance matrix, is included in the uncertainties of velocities of sites relative to the Indian plate. For many sites, the uncertainty in the motion of the Indian plate is the dominant component in the velocity uncertainty. Figure 3.2 shows our site velocities in Nepal and southern Tibet relative to XIGA, in Xigatse.

3.5 Active deformation in southern Tibet

3.5.1 East-West Extension

Geologic and seismic evidence suggest that the orientation of extension in Southern Tibet is ~N110°E [*Armijo* et al., 1986; *Molnar and Lyon-Caen*, 1989]. To better compare our GPS results with geologic inferences, we show horizontal velocity components perpendicular and parallel to a N110°E profile through XIGA as a function of distance along the profile in Figure 3.3.

In southern Tibet and northern Nepal, the total rate of extension in the N110°E direction between Lhasa (LHAS) and Simikot (SIMI) is about 13±2 mm/yr over about 1000 km, or about 0.013 μstrain/yr. This agrees with 0.012 μstrain/yr of along-arc tensile strain rate in southern Tibet estimated by *Bilham* et al. [1998] and is consistent with the 11±3 mm/yr of extension rate observed between SIMI and LHAS by *Larson* et al. [1999] using a subset of our full data set. If we include the site Shiquanhe (SHIQ) on the west near Karakorum Fault Zone and Gongbu (GNGB), 250 km east of Lhasa (Figure 3.2 and 3.3a), the total extension rate between 80°E and 93°E in the N110°E direction is about 26±3 mm/yr. *Molnar and Lyon-Caen* [1989] estimated 18±9 mm/yr of extension between 75°E and 95°E from seismic evidence, which is smaller than our rate but was close to correct. The extension rate (N110°E) between SIMI in northwestern Nepal (82°E) and SHIQ is insignificant (1±2 mm/yr). About 13 mm/yr of extension occurs between Lhasa and Gongbu, which are only about 300 km apart. Clearly, the extension rate is not uniform along the length of the Himalayan arc as many previous studies had assumed.

The site velocities over the entire area are not easily explained by a simple combination of N110°E extension inferred from geologic features by *Armijo* et al. [1986] or strain resulting from uniform coupling along the Main Himalayan Thrust [*Larson* et al., 1999; *Bilham* et al., 1997]. Along the profile, the site velocities in the N110°E direction (relative to Lhasa) of sites Jiangzi (JIAN) and Xigatse (200-300 km west of Lhasa) are 5.5±1.2 mm/yr and 6.7±0.8 mm/yr respectively, implying that the extension rate across the Yadong-Gulu rift is about 5-7 mm/yr, while those of Tingri (TING), Rongbuk (RONG) and Jomosom (JOMO) (500-800 km west of Lhasa) average 10±2 mm/yr. Thus, about one-half of the east-west extension rate between 80°E and 90°E may be concentrated across the Yadong-Gulu rift. The extension rate increases to the east of Lhasa, although this observation is based on only one site. The velocity of Gongbu 300 km east of Lhasa is significantly different from that predicted from simple dislocation models that explain GPS data in the Himalaya of Nepal [*Larson* et al., 1999].

About 400 km west of Xigatse, near 86°E, the site SHOT north of the Yarlung-Zangbo suture and site WT12 south of the suture have significantly different velocities (about 7 mm/yr) in the N110°E direction (Figure 3.3). This can also be clearly seen in the velocities relative to Xigatse (Figure 3.2). These sites are only 50 km apart, and we interpret this

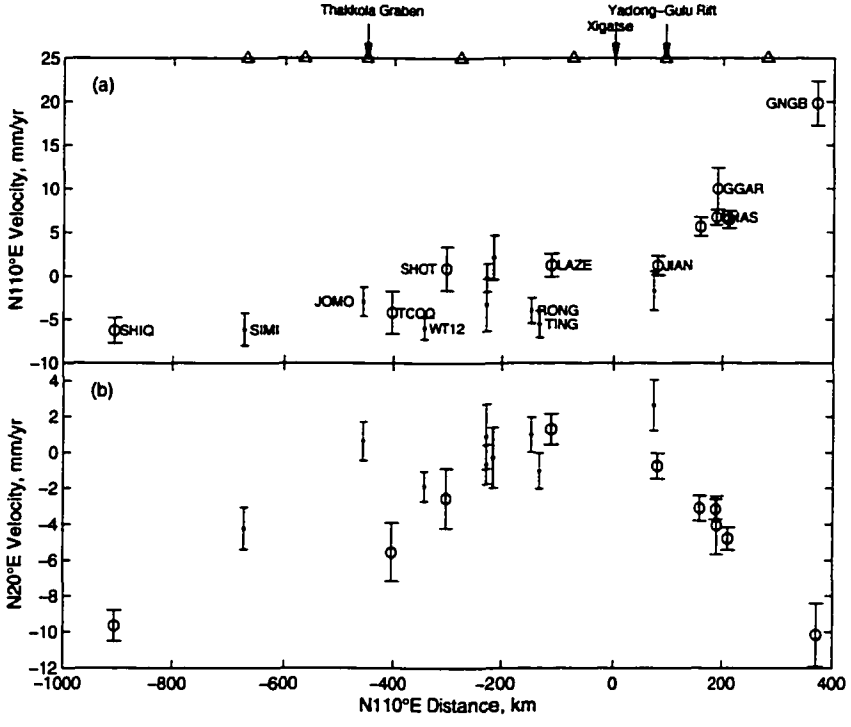

Figure 3.3. Velocity components as a function of distance along a N110°E profile (Relative to XIGA) in (a) the N110°E direction; (b) the N20°E direction. The error bars represent one standard deviation. Circle: sites north of the YZS; Dot: sites south of the YZS; Triangle: Projected locations of seven rift systems.

difference as being due to the presence of an active strike-slip fault between them. Figure 3.3 also shows that sites TCOQ, SHOT, LAZE, XIGA, on the north of the YZS show significantly slower westward velocities (relative to XIGA) than sites farther to the south (e.g., TING, RONG, WT12, and JOMO). This shows that not only is the extension rate non-uniform across all of southern Tibet, but also that the crust north of the Yarlung-Zangbo suture moves eastward more rapidly than that south of the suture, meaning that strike slip faults roughly coincident with the suture appear to accommodate part of the eastward extrusion of Tibet.

Figure 3.3b shows velocity components in the N20°E direction along a N110°E profile crossing the southern Tibet. For most of sites between the Yadong-Gulu rift and Thakkola graben system, the southward motion relative to XIGA is not significant, and slower than those of the sites from east of the Yadong-Gulu rift and west of Thakkola graben. If we postulate that this southward motion is mostly caused by the steady slipping portion of the thrust system below the Himalaya, the different southward motion at sites of southern Tibet would imply variation in the slip rate of India beneath Tibet along the Himalayan arc.

3.5.2 Convergence between Tibet and India

The convergence across the Himalaya can be shown best by projecting site velocities onto a single profile constructed in the direction of N12°E the approximate convergence direction between India and Eurasia (see later discussion). Figure 3.4 shows this profile with site velocities (relative to India) in the N12°E direction versus the distances from NAGA (in Kathmandu, Nepal) along the N102°E direction.

Figure 3.4 clearly shows that sites in southern Tibet (TING and XIGA) are moving southward at 12±2 mm/yr with respect to the Indian plate and that sites in southeastern Nepal (e.g., BIRA and JANK) are not moving significantly (2±2 and 0±2 mm/yr, respectively) relative to India. Thus, horizontal contraction between BIRA and TING across eastern Nepal is 11.7±1.5 mm/yr over 240 km (about 0.049 μstrain/yr contractional rate), significantly lower than 18±2 mm/yr estimated by *Larson* et al. [1999] based on the same sites but more limited data. We see the same situation in western Nepal, SIMI is moving south at 13±1 mm/yr, while sites in southwestern Nepal (MAHE and NEPA) are moving

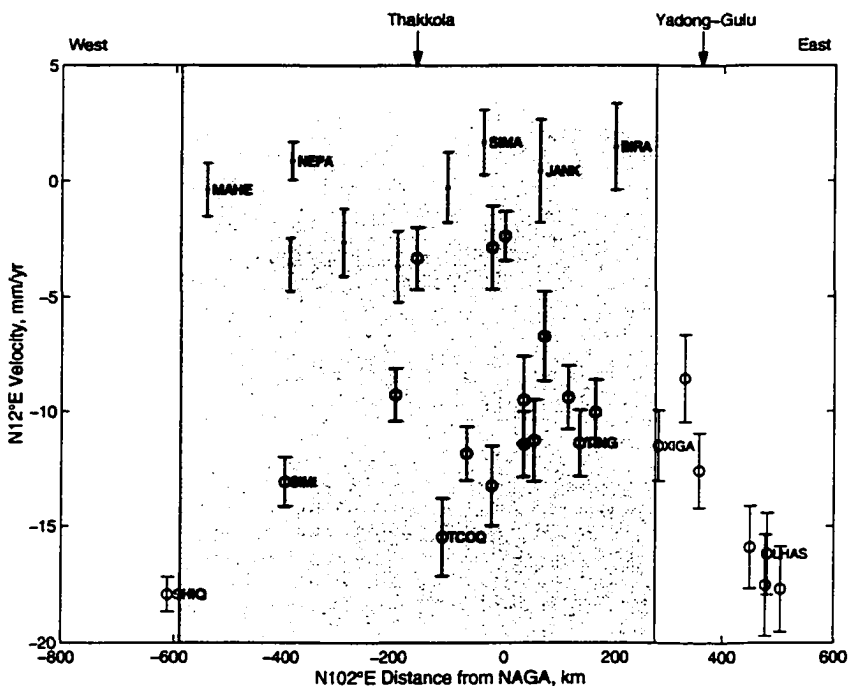

Figure 3.4. Velocity in the N12°E direction as a function of distance from NAGA along a N102°E profile (relative to Indian plate). The error bars represent one standard deviation. Circles: sites north of the MHT; Dot: sites south of the MHT. The region of the Nepal GPS network used in *Larson* et al. [1999] is shaded.

negligibly, again relative to India. This suggests that the rate of shortening within the network in western Nepal (between SIMI, MAHE, and NEPA) is 13.4±0.9 mm/yr over 200 km (about 0.067 μstrain/yr), as *Larson* et al. [1999] observed.

Farther to the west between 76°E and 81°E, and east of the Yadong-Gulu rift between 90°E and 93°E, we do not have data near the Himalayan arc, so we cannot determine the contraction rate across these two segments, although it looks like a higher rate of ~18 mm/yr exists there based on SHIQ and LHAS (Figure 3.4). More data from the region are required to constrain the shortening rate.

Compared to *Larson* et al. [1999], we find significant differences in the velocities at some sites. Figure 3.5 shows this comparison by constructing a similar profile of Figure 3.4 with site velocities relative to NAGA from this study and *Larson* et al. [1999]. Clearly the velocities at sites in Nepal are consistent within uncertainties, but velocities of three sites in southern Tibet (TING, RONG, and LHAS) are significantly different with ~6 mm/yr lower estimated by this study than that by *Larson* et al. [1999] based on more limited data. TING is an critical site because both *Larson* et al. [1999] and this study used it to estimate the convergence rate between India and Tibet.

The accuracy of the estimated site velocities depends on several factors: the number of site occupations, the daily survey period, and precise global tracking network, etc.. Figure 3.6 shows the time series of NAGA and TING. NAGA was first surveyed in 1991, and then followed in 1992, and 1995 in campaign style. After 1996, NAGA was observed as a permanent site. *Larson* et al. [1999] included data from NAGA measured between 1991 and 1997, while we used data between 1991 and 2000. TING is a campaign site, first surveyed in 1991. We include all available data for TING between 1991 and 1998, while only 1991 and 1995 data were available to *Larson* et al. [1999] (They did not yet have access to the 1994 survey data). The large scatter in the 1991 estimates of the site position results from the limited global tracking network available at that time. We found that the uncertainty in the determination of the reference frame transformation for the 1991 data is more than 10 cm due to the limited global tracking network. However, the transform program does not account for this and assumes that the transformation is perfect. Thus, the site positions for the 1991 data could be biased and the uncertainties too small. A single biased site position could bias the site velocity unless we have large enough number of the site occupations. For

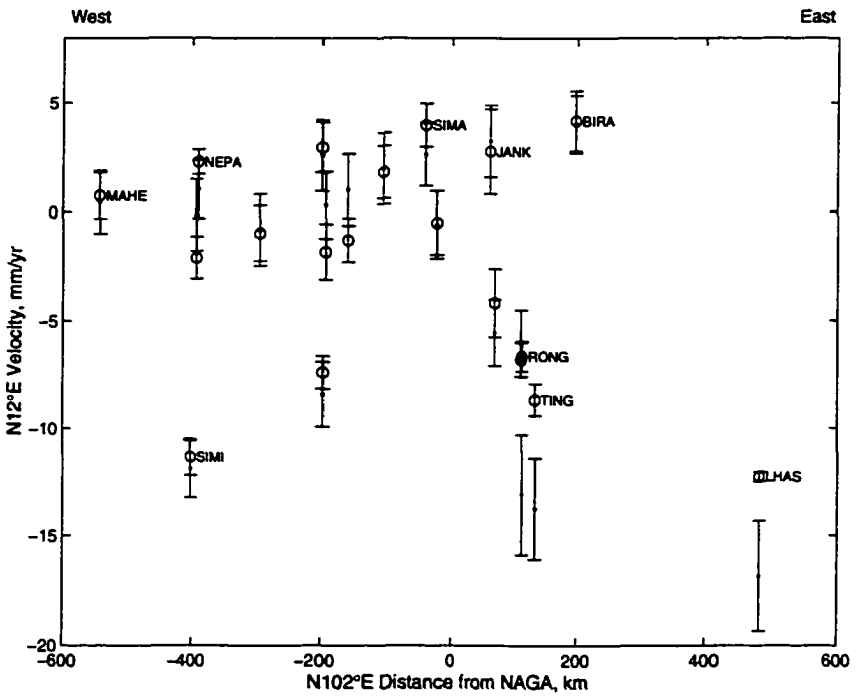

Figure 3.5. Velocity in the N12°E direction as a function of distance from NAGA along a N102°E profile (relative to NAGA). The error bars represent one standard deviation. Circle: velocities from this study; Dot: velocity from *Larson* et al. [1999].

example, the velocity at NAGA does not change if we exclude the 1991 survey, implying that the large scatter in site position resulting from the uncertainty of the reference frame transformation for the 1991 survey does not change the velocity significantly, because there are many other data spanning a long survey period. However, this is not the case at TING. Excluding either the 1991 or 1998 data for TING would significantly change the velocity at TING (Figure 3.6b). This suggests that the velocity at TING estimated by *Larson* et al. [1999] was biased based only on measurements in 1991 and 1995, thus the convergence rate between India and Tibet estimated by *Larson* et al. [1999] using velocity at TING as a input parameter was biased. It could be argued that the 1998 data are biased for some reasons rather than the 1991 data, however, this is less likely, and our velocity estimate for TING agrees well with neighboring sites.

3.6 Modeling

Strain resulting from the locked thrust system below the Himalaya has been modeled by *Bilham* et al. [1997] and *Larson* et al. [1999] as uniform slip on rectangular dislocation planes embedded in a homogeneous, isotropic, and elastic half-space [*Okada*, 1985]. In these models, they estimated the rate of slip of India beneath Tibet to be ~20 mm/yr, and reported ~18 mm/yr contraction rate across the Himalaya. The models fit the data from Nepal quite well but do not explain the observations at sites north of the Zangbo suture, which is affected by east-west extension of southern Tibet.

We start with the two-fault dislocation model of *Larson* et al. [1999] and try to use it to remove the effects of strain due to the Himalaya. Figure 3.7 shows the residuals of the observed and predicted velocity field by *Larson* et al. [1999] relative to Xigatse. This model fails to explain the east-west extension we observe in southern Tibet, and overestimates the arc-normal components by ~4 mm/yr implying that their model overestimated the slip rate of India beneath Tibet in eastern Nepal based on biased data. The misfit in the N110°E direction is largely due to the fact that the *Larson* et al. [1999] model does not include significant local structures such as the Yadong-Gulu rift. Clearly, a revised and more complex model is required.

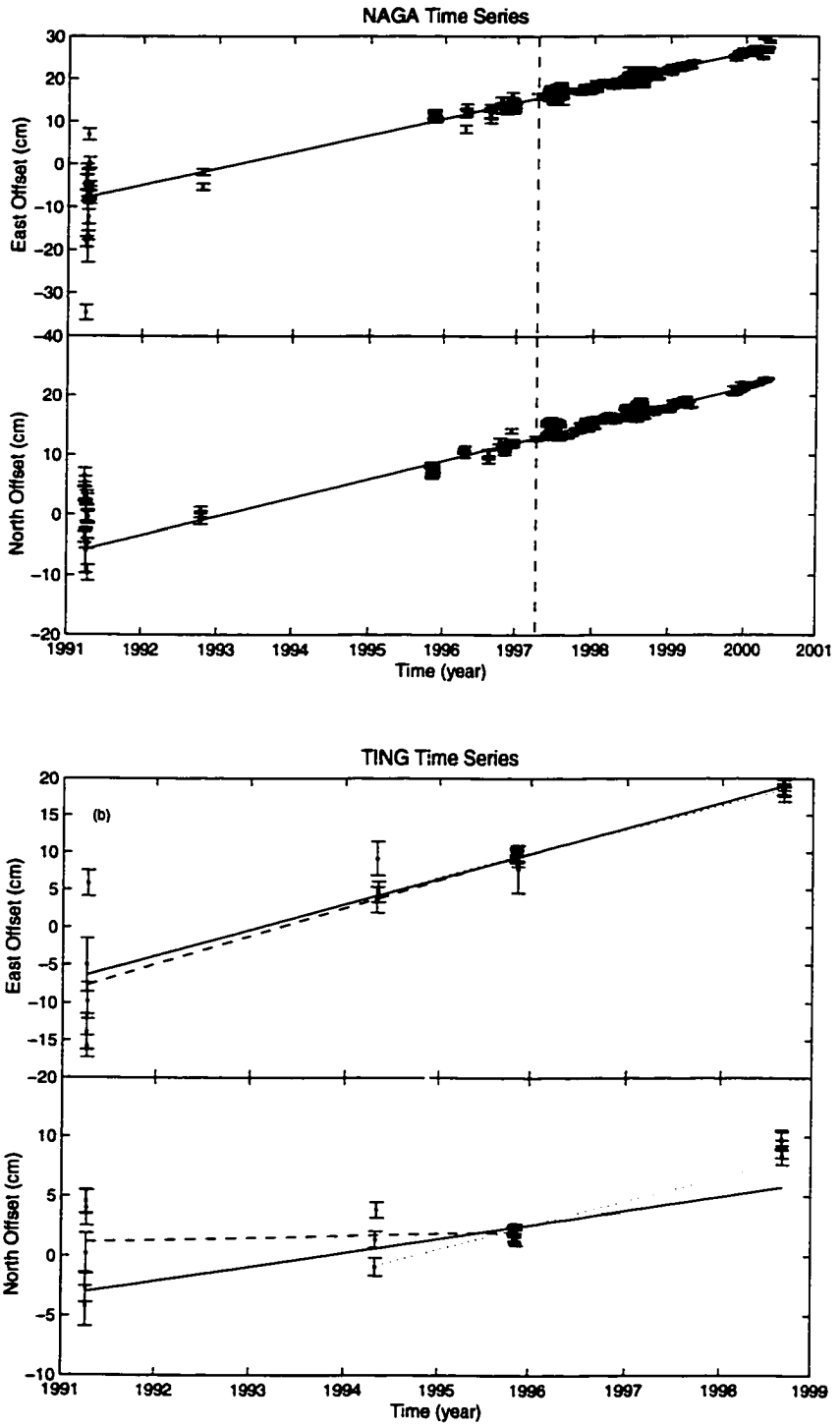

Figure 3.6. Time series plot of (a) NAGA, and (b) TING. Solid line: best fit for the complete time series; (a)Dashed line marks the end of temporal span in *Larson* et al. [1999]. (b) Dotted line: best line fit when excluding the 1991 survey for TING; Dashed line: best line fit when excluding the 1998 survey for TING. Note the different horizontal (time) scales for the two stations.

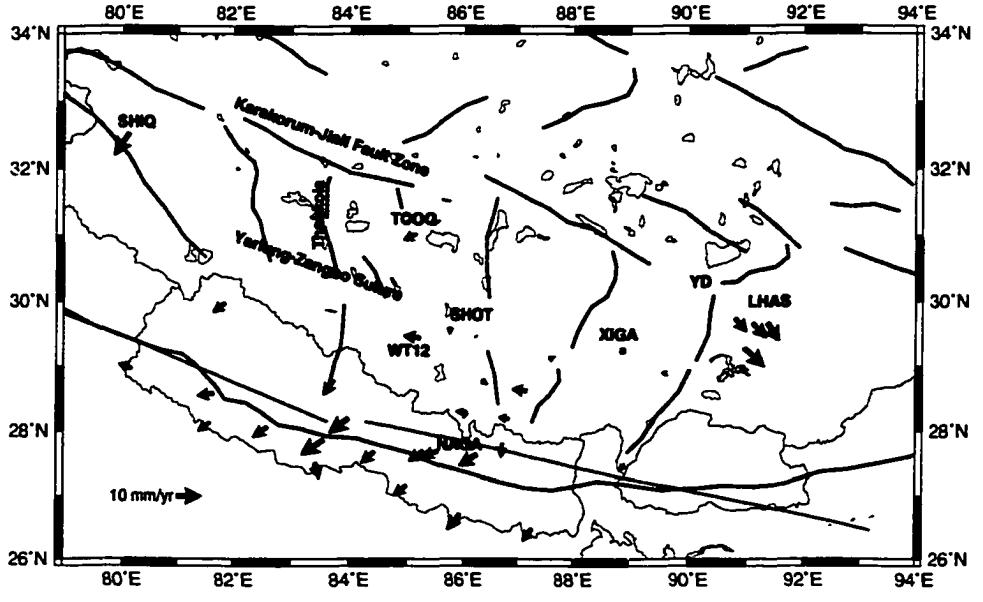

Figure 3.7. Velocity field (relative to XIGA) in Nepal and southern Tibet after removing the main Himalayan deformation using the two-fault model from *Larson* et al. [1999]. XIGA is shown as a solid square. The surface projections of the fault planes are shown as black lines.

3.6.1 Dislocation and Block Model

To better understand the mechanism of deformation in southern Tibet, we assume that GPS observations of surface deformation, to first order, are divided into two components: strain due to the locked Main Himalaya Thrust (MHT) and internal deformation of the plateau due to the local faults in southern Tibet. The first component is due to the Indian plate underthrusting Tibet. Possible faults in southern Tibet include the seven north-south trending normal faulting systems, right-lateral strike-slip faults of the proposed Karakorum-Jiali Fault Zone (KJFZ) [*Tapponnier* et al., 1981; *Armijo* et al., 1986, 1989], and the Yarlung-Zangbo suture which may cut through these normal faulting systems and separate southern Tibet into two parts: south and north of the suture.

Strain resulting from the locked thrust system below the Himalaya is modeled by rectangular dislocation planes embedded in a homogeneous, isotropic, and elastic half-space [*Okada*, 1985], as *Larson* et al. [1999] have done. We model the internal deformation component using four additional dislocations: one along the Karakorum fault, another along the YZS, both of which are modeled as pure right-lateral strike slip faults; the third dislocation is along the Thakkola graben, the fourth is along the Yadong-Gulu rift, the longest rift in southern Tibet, concentrating most of the east-west extension. We use simple models of vertical opening cracks for the graben and rift because we have no data close to them and the opening model is not distinguishable from a dipping fault model (with equivalent opening rate) in the far-field. We fix the geometries of these four faults based on geological evidence [*Armijo* et al., 1986, 1989], and only estimate the slip rates. We neglect the other five north-south trending rift systems in southern Tibet, because they do not appear to have any significant impact on the observations. We use all data shown in Figure 3.2 and Table 3.1. Table 3.2 summarize the geometries of the dislocations.

To better reflect the geometry of the Himalayan arc, we increase the number of dislocations along the Himalaya to model the MHT. We treat the eastern fault of *Larson* et al. [1999] as two dislocations with different orientations, separated by the Yadong-Gulu rift. The total seven dislocations separate southern Tibet and the Indian plate into six quasi-stable blocks: blocks north and south of the Karakorum fault, blocks north and south of the Zangbo suture between the Thakkola graben and Yadong-Gulu rift, a block east of the Yadong-Gulu rift, and the rigid Indian plate, as indicated in Figure 3.8.

Table 3.2. Model Parameters

Fault	Length km	Dep km	Mid-point‖ °N	Mid-point‖ °E	Dip deg	Strike deg	Dip-slip* mm/yr	Strike-slip† mm/yr	Opening‡ mm/yr
Karakorum	489.2	15.0	32.3	79.8	-90.0	140.0	-	3.6±1.0	-0.7±1.0
							-	(3.7±1.0)	(-0.5±1.0)
YZS	813.4	15.0	29.5	85.5	-90.0	106.0	-	2.8±0.8	0.0±0.3
							-	(2.9±0.8)	(-0.1±0.3)
N. Yadong	357.2	15.0	29.6	90.3	-90.0	30.0	-	2.6±0.6	6.6±2.2
							-	(2.3±0.6)	(4.3±2.0)
S. Yadong	141.2	15.0	27.6	89.0	-90.0	30.0	-	2.0±0.6	9.3±2.2
							-	(1.7±0.6)	(7.1±2.0)
N. Thakkola	319.5	15.0	31.5	83.5	-90.0	-1.0	-	-5.9±1.4	6.1±1.9
							-	(-5.6±1.2)	(5.0±1.7)
S. Thakkola	207.4	15.0	29.1	83.6	-90.0	-1.0	-	-3.5±1.4	5.2±1.9
							-	(-3.3±1.2)	(4.2±1.7)
West Himalaya	800.0	18.3	30.0	79.3	-9.5	115.0	-17.0±0.9	0.8±1.9	-
							(-16.4±0.8)	(1.7±1.8)	-
Central Himalaya	485.0	14.3	28.0	85.5	-2.5	102.2	-12.2±0.4	1.2±0.8	-
							(-12.2±0.4)	(1.4±0.8)	-
East Himalaya	660.0	20.3	27.4	92.5	-3.1	83.9	-19.0±1.2	3.7±1.2	-
							(-17.5±1.0)	(2.2±1.0)	-

‖surface projections of mid-points of downtip of locked part.

*negative values indicate thrusting.

†positive values indicate right-lateral motion; negative values indicate left-lateral motion.

‡positive values indicate opening; negative values indicate shortening.

Results in Brackets are from the alternative model, see text for detail.

For each dislocation along the MHT, *Larson* et al. [1999] estimated eight parameters: fault length L, width W, depth D, dip δ, strike ϕ, location (x_0, y_0) of the middle point of down tip of the locked portion, and dip-slip rate v. In our model, we estimate small changes to these parameters, and we also increase the number of estimated parameters by adding four local faults in southern Tibet. To make the model self-consistent, all slip rates on the dislocations are calculated using the velocities of the blocks as the fundamental parameters. To avoid edge effects, we estimate deformation using a back-slip model by a combination of steady block motion with a dislocation slipping in the opposite direction of the motion in the locked portion of the fault [*Savage*, 1983]. The site velocity can be calculated by $v = v_{block} - \sum_{i=1}^{N} v_{disloc_i}$. Here v_{block} is the block velocity, and v_{disloc_i} is the predicted velocity of ith dislocation slipping on the locked portion, and N is the number of the dislocations. v_{disloc_i} is modeled using dislocation theory [*Okada*, 1985], assuming a Poisson half-space. This technique is quite similar to that used in the Marmara Sea region in Turkey [*Meade* et al., 2002] where only vertical faults with strike-slip and opening were modeled. Here we extend the approach to include all types of faults with strike-slip, dip-slip, and/or opening.

3.6.2 Inversion Method

Any model that estimates fault geometries from geodetic data is a non-linear inversion problem (estimating only slip rates with a fixed geometry is a linear problem). Thus, our model reduces to non-linear optimization. The optimal source model will minimize the model misfit between the observation data and the model prediction. Here we use "Mean Square Error (MSE)" which is the weighted residual sum of squares normalized by the degrees of freedom (number of data minus the number of estimated model parameters) as followed:

$$MSE = \frac{(d_{obs} - d_{mod})^T \Sigma^{-1} (d_{obs} - d_{mod})}{n - p} \tag{3.1}$$

where d_{obs} and d_{mod} are the observation and model prediction, respectively, Σ is the data covariance matrix, n is the number of data, and p is the number of the estimated model parameters.

Many algorithms have been proposed to solve this optimization, such as the Levenberg-Marquardt method [*Gill* et al., 1981], the quasi-Newton method [*Árnadóttir and Segall*,

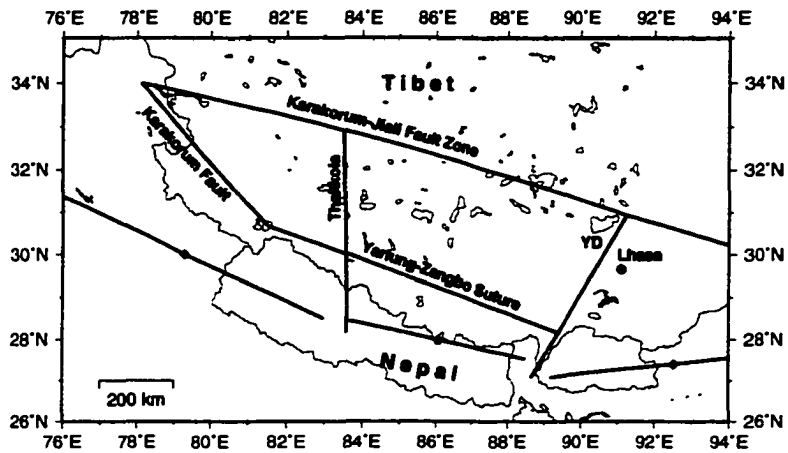

Figure 3.8. Map outlining the block boundaries in this study. The Himalayan arc is modeled as three faults, shown the surface projections of the fault planes with diamonds as mid-points.

1994], simulated annealing [*Metropolis* et al., 1953] and the random cost algorithm [*Berg*, 1993]. In this chapter, we use the random cost algorithm to estimate our model parameters. Random cost is an optimal Monte Carlo approach for non-linear optimization problems with many local minima in the misfit space, and mimics a random walk in "cost" space [*Berg*, 1993]. It preferentially samples the local minima (or maxima) in the cost space while using a simple stochastic process to search thoroughly the full possible model space. For more details about the algorithm, refer to *Berg* [1993] and *Cervelli* et al. [2001]. The random cost nonlinear optimization technique has been found to be a computationally efficient method of inverting source geometry using geodetic data [*Murray* et al., 1996; *Freymueller* et al., 1999; *Cervelli* et al., 2001].

However, in this study, the geometries of the dislocations along parts of the Himalaya cannot be well estimated based on our available GPS data, e.g., without data from close to the arc in the western and eastern part of the Himalayan arc, we cannot determine the locking depths there. In our modeling, we first use the random cost algorithm to estimate small changes to *Larson et al.*'s [1999] model parameters, then fix geometries of the dislocations of the "optimal" estimates to be *a priori* model geometries, and investigate

the block motions. This reduces to a linear inversion problem, so linear least squares estimation techniques are used. Finally, we use forward modeling to test the sensitivity of model geometries.

3.7 Results

In this study, we present results from a combination of forward and inverse (linear and non-linear) dislocation modeling. The estimated parameters for the optimal model are summarized in Table 3.2. Figure 3.9 the shows observed and model predicted horizontal velocities relative to rigid Indian plate, as well as the surface projection of the fault planes. The modeled velocity field is matched quite well, and yields a weighted misfit per degree of freedom of 1.12.

The Himalayan arc is modeled by three dislocations with different orientations. The estimated strikes of the western, central, and eastern faults are 115°, 102°, and 84°, respectively. The geometries of the fault tips in the western and eastern Himalaya are poorly determined, since we do not have data near the arc. We constrain these two fault tips to be consistent with a small circle shape of the India-Eurasia collision boundary constrained by seismicity, topography, stress state, and geodetic data [*Bendick and Bilham*, 2001]. In contrast, the location of the central fault is well determined, and we suggest that in the central Himalaya, the Indian plate is locked northward to 80 km north of Kathmandu (NAGA), with a shallow dip of ~4°.

Bilham et al. [1997] suggested a deeper locking depth in western Nepal than in eastern Nepal, with dislocations dipping at ~4° in the seismogenic portion, and increasing smoothly in dip to ~9° northward at a deeper level. *Larson et al.*'s [1999] two-fault model confirmed that. Our models favor a similar locking depth of 18-20 km along the Himalayan arc, with a steeper dipping angle of ~9° in western Himalaya, and a shallower dip of ~3° in the central and eastern Himalaya. Overall, the geometry of our central Himalaya model segment is quite consistent with the previous suggestions [*Bilham* et al., 1997; *Larson* et al., 1999], as there are more data available to constrain the model than in western Nepal.

Our model suggests slip rates of 17±1 and 19±1 mm/yr for India beneath Tibet in the western and eastern Himalaya, respectively. These are consistent with previous estimates

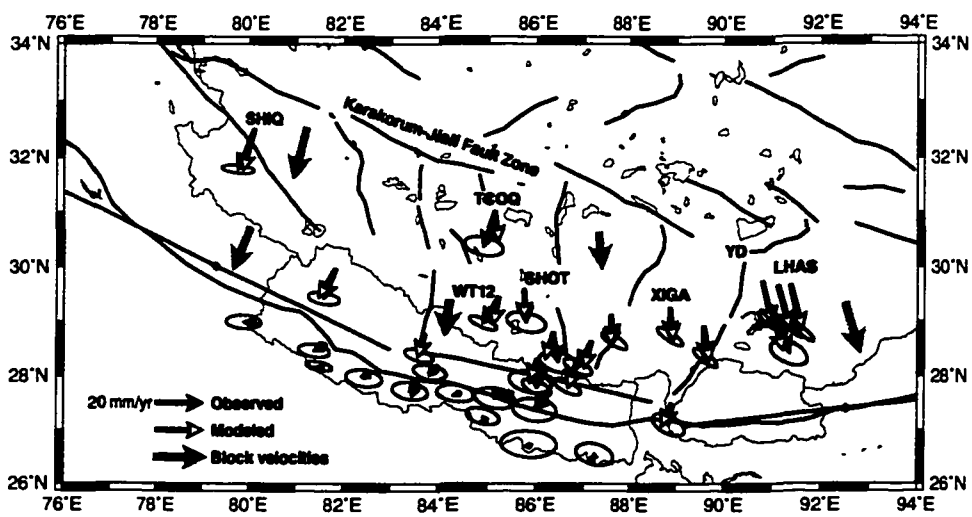

Figure 3.9. Observed horizontal velocities (solid vector) relative to Indian plate and predicted horizontal velocities (open vector) from our preferred model. Uncertainties are 95% confidence ellipses. The surface fault projections shown as solid lines with diamonds as indicating their middle points. Large grey vectors: predicted block velocities relative to Indian plate.

from GPS observations based on more limited data [*Bilham* et al., 1997; *Larson* et al., 1999]. However, along the central Himalaya, between the longitudes of 83°E and 88°E, we find a lower slip rate of 12.2±0.4 mm/yr. We will discuss this in more detail in the following section.

Our models predict a right-lateral shear of 4±1 mm/yr on the Karakorum fault, similar to the recent estimate by *Brown* et al. [2002] based on cosmic ray exposure dating of debris flows and moraines, but significantly lower than the ~30 mm/yr estimated by *Liu* [1993]. However, this geologic estimate was based on assumed dates for topographic offsets, which led to its high uncertainty. We infer that this strike-slip extends from the Karakorum fault to along or close to the Yarlung-Zanbo suture, with a slip rate of 3±1 mm/yr, and may terminate at the Yadong-Gulu rift.

3.8 Discussion

3.8.1 Convergence Across the Himalaya

We use three dislocations to model the Himalaya, with the estimated strikes of 115°, 102°, and 84° in the western, central, and eastern Himalaya, respectively. Our geometry is more realistic than *Larson et al.*'s [1999], where their eastern fault did not fit the curve of the Himalaya.

We estimate that the rates of slip of India beneath Eurasia in the western Himalaya between 76°E and 83°E and the eastern Himalaya between 89°E and 96°E are comparable to the previous estimates based on more limited GPS data [*Bilham* et al., 1997; *Larson* et al., 1999]. However, in the central Himalaya between 83°E and 88°E, our estimated rate of 12.2±0.4 mm/yr is significant lower than 21.8±1.3 mm/yr suggested by *Larson* et al. [1999]. The slip rates were mis-estimated by *Larson* et al. [1999] based on biased far-field data in southern Tibet (Figure 3.5 and Figure 3.6b).

For comparison, Figure 3.10 shows the GPS site velocities (relative to NAGA) in the fault perpendicular (12°) component plotted against the distance from NAGA, as well as the predictions of our model and that of *Larson* et al. [1999]. The model of *Larson* et al. [1999] overpredicted the slip rate of India beneath Tibet, resulting from biased data at sites RONG and TING. With the more accurate velocities of RONG and TING, we find a much

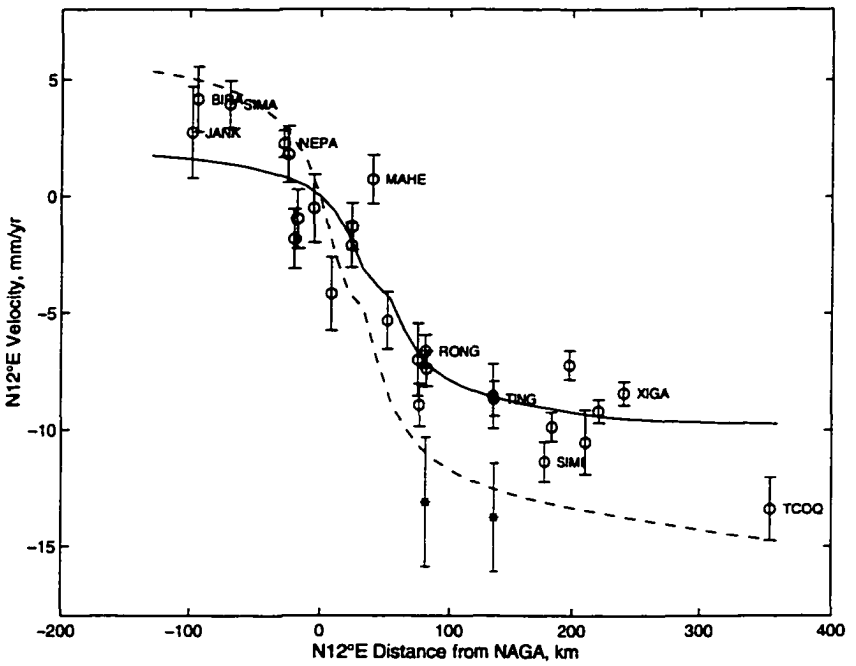

Figure 3.10. Velocities (relative to NAGA) in fault perpendicular (strike 102°) component of sites between 80°E and 90°E with respect to the distance from NAGA along N102°E. The error bars represent one standard deviation. Solid line: predicted by our model; Dashed line: predicted by *Larson* et al. [1999]. Circles: Velocities in this study; Stars: velocities from *Larson* et al. [1999].

different model than *Larson* et al. [1999].

3.8.2 Implications For the Convergence Rate

To test whether this low convergence rate might apply to the entire arc, we try an alternative model in which we added pseudo-observations to constrain the slip rates *a priori* along the eastern and western Himalaya to be 13±2 mm/yr, comparable with that in the central Himalaya. The total residuals (χ^2) increases from 60 to 70 when these *a priori* constraints are added, not significantly different at the 95% confidence level. Table 3.2 also gives the slip rate on each dislocation predicted by this model. Most rates are comparable with those predicted by the block model with data only, except that they are slightly different on the Yadong-Gulu rift and eastern Himalaya, implying that more data from eastern Himalaya will help to constrain the model. Even with the addition of these *a priori* constraints on the

slip rate, the convergence rate to the east and west remains substantially higher than in the central region. We infer from this that the variation in convergence rate that we observe is probably significant, despite the modest change in misfit when the *a priori* constraints are applied.

The 750-km-long segment between the rupture areas of the 1905 Kangra and 1934 Bihar/Nepal earthquakes (Figure 3.11) has been identified as a seismic gap, because great earthquakes have occurred there in the past but not in the last 200 years [*Khattri*, 1987]. This region corresponds to our eastern and central Himalayan segments. Our lower estimated slip rate implies a lower accumulation rate of strain, and thus a longer recurrence time for great earthquakes in this area. In western Nepal there have been no recent great earthquakes for 200 years and perhaps for much longer [*Bilham* et al., 1997]. Given the 17±1 and 12.2±0.4 mm/yr of slip rates in the eastern and central Himalaya, if one great earthquake occurs in the seismic gap, it is more likely to be west of N83°E than east. Futhermore, our new lower shortening rate (~12 mm/yr) suggests a slightly lower earthquake harzard than previous supposed. Nevertheless, 12 mm/yr of convergence is still quite rapid, and the fault is clearly locked, so compared to most parts of the world the seismic hazard in Nepal is extremely high.

Our estimated convergence directions along the western, central, and eastern Himalaya are N25°E, N12°E, and N12°W, respectively, approximately normal to the local strike of the Himalayan arc, also consistent with slip vectors of the earthquakes [*Molnar and Lyon-Caen*, 1989]. Figure 3.12 shows the azimuths of slip vectors of earthquakes from *Molnar and Lyon-Caen* [1989] and our estimated convergence directions versus longitude. The variations of the convergence directions are consistent with the variation in the strike of the arc. If India behaves as a rigid plate, this variation in the direction of overthrusting in the Himalaya results from roughly east-west extension in southern Tibet, as noted by *Molnar and Lyon-Caen* [1989]. We will discuss this in more detail in section 3.8.5.

3.8.3 Yadong-Gulu Rift

Our estimate of the opening rate for the Yadong-Gulu rift is 6.6±2.2 mm/yr, much higher than the 1.4 ± 0.8 mm/yr estimated by *Armijo* et al. [1986]. Our high rate supports the implication of greater extension in the rift from the observation of ductile high-strain zones

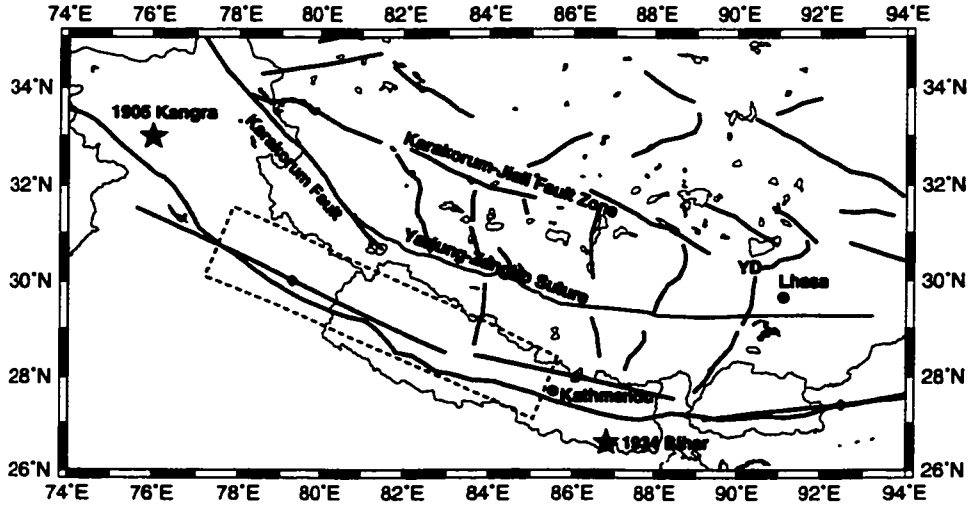

Figure 3.11. Map showing the location of seismic gap according to *Seeber and Armbruster* [1981]. The surface projections of the fault planes along the Himalaya are also shown as solid lines with diamonds as mid-points of the faults.

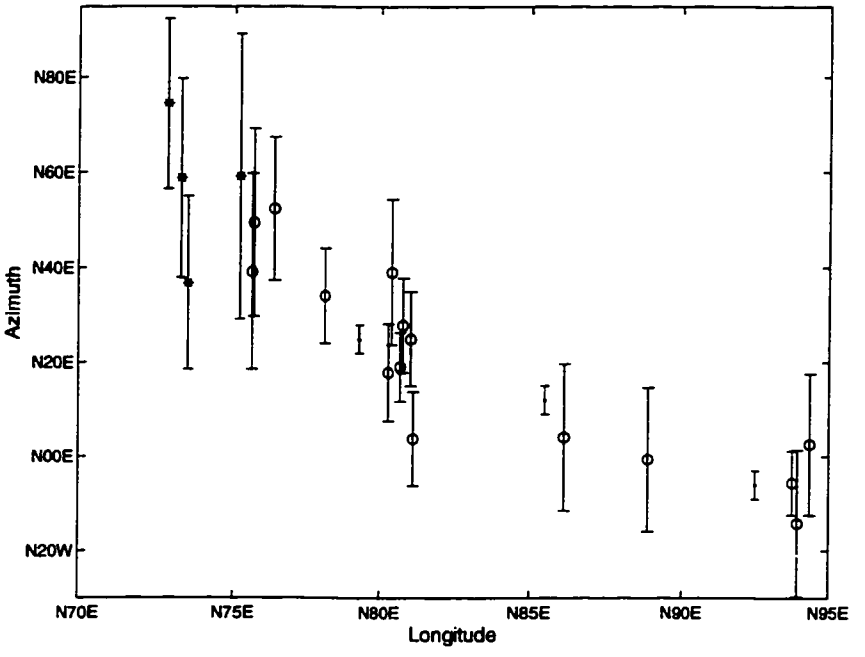

Figure 3.12. Azimuths of convergent vectors estimated in this study and slip vectors of earthquakes [*Molnar and Lyon-Caen*, 1989] in the Himalaya plotted as a function of the longitudes. The error bars represent one standard deviation. Circles: slip vectors of earthquake; Dots: estimated convergent vectors; Stars: P-axes of earthquakes in the western Himalaya.

exposing rocks exhumed from midcrustal depths in the footwalls along the Yadong-Gulu rift [*Cogan* et al., 1998].

The high opening rate of the Yadong-Gulu rift may be the cause of the ductile high strain shear zones which have been identified in the central Nyainqentanglha range of the northern Yadong-Gulu rift [*Pan and Kidd*, 1992; *Harrison* et al., 1995] and on the east side of Nieru and Duoqen Valley of the southern Yadong-Gulu rift [*Burchfiel* et al., 1991; *Kidd* et al., 1995]. Combining these observations of high-strain zones along the rift with INDEPTH refraction and shallow reflection data, *Cogan* et al. [1998] propose a "rolling-hinge" model of crustal extension. In this model, uplift and rotation of the footwall of the rift is being accommodated at depth by flow in the middle crust. This flow may accommodate the opening of the Yadong-Gulu rift, and is likely to be a consequence of the middle crust being partially molten [*Nelson* et al., 1996].

The presence of partially molten rocks and the observed locally extreme heat flow within the Yadong-Gulu rift [*Francheteau* et al., 1984] suggest that the weakness of crust is present along the rift. Such a weak crust implies localized high strain and deforming rate. Given non-uniform spatial extension rate in southern Tibet we observe here, we conclude that it is unlikely that the crust in the Yadong-Gulu rift is typical in southern Tibet. Any estimates of extension rate based on the assumption that the Yadong-Gulu rift is a representative of other rifts in southern Tibet, as *Armijo* et al. [1986] did, would be biased.

3.8.4 Yarlung-Zangbo Suture

The Yarlung-Zangbo suture is the principal paleogeographic boundary along which early convergence between India and Eurasia took place [*Seeber* et al., 1981; *Burg* et al., 1984; *Ni and Barazangi*, 1984; *Alsdorf* et al., 1998]. We find evidence of the presence of an active strike-slip fault along or near the YZS in the western Tibet. We interpret strike-slip faulting on or near the suture as a continuation of the active Karakorum fault further west. In our numerical model, we assume this explicitly through our block boundaries. Examination of the velocity field suggests that strike-slip motion continues as far east as the Yadong-Gulu rift, as noted by *Ratschbacher* et al. [1994] based on the field observations and radiometric data. East of the Yadong-Gulu rift, we have no data from south of the suture, so we cannot tell if strike-slip motion continues farther east.

If we assume that all relative motion between WT12 and SHOT results from slip along the YZS, we would expect a right-lateral slip rate of 7.4±2.7 mm/yr along the YZS. However, our block model requires overall consistency of the entire velocity field, and in the block model we obtain a lower rate of 2.6±0.7 mm/yr of right-lateral slip. The estimate from the block model should be more reliable because it is based on data from many sites. Recent field investigations along the Karakorum fault in Ladakh, western Indian Himalaya, suggest a slip rate of 4±1 mm/yr on the Karakorum fault [*Brown* et al., 2002], which is significantly lower than the ~30 mm/yr estimated by *Liu* [1993] using assumed ages of offset glacial features. These new slip rates for the Karakorum fault are quite similar to the slip rates we estimate across the suture, and the consistency supports our interpretation of this fault as an eastward continuation of the Karakorum fault. The slip rate we observe on the suture is approximately the projection of the Karakorum fault slip vector onto the orientation of the suture.

3.8.5 Non-uniform East-West Extension in Southern Tibet

Table 3.3 summarized the block velocities relative to the Indian plate. Figure 3.13 shows the block velocities relative to both the Indian plate and the block north of the YZS between the Thakkola graben and the Yadong-Gulu rift. To better evaluate east-west extension in southern Tibet, we look at the N110°E component of the block motions.

The block west of the Thakkola graben and north of the Karakorum fault moves at 2.0±2.5 mm/yr in the N110°E direction relative to India, not significantly different from zero. The N110°E component of block east of the Yadong-Gulu rift is 11.7±1.5 mm/yr. This suggests that the total permanent extension in the N110°E direction between longitudes of 78°E and 92°E is ~12 mm/yr. The slightly larger rate of 15±1 mm/yr observed between SHIQ and Lhasa includes a component due to elastic strain from the locked MHT, which is presumably recovered in great earthquakes.

The block east of the Yadong-Gulu rift moves at ~7 mm/yr in the N140°E direction relative to the block north of the YZS between the Thakkola graben and Yadong-Gulu rift, implying half of the relative motion between the longitudes of 78°E and 92°E north of the YZS is concentrated across the Yadong-Gulu rift. However, south of the YZS, about two-thirds of the extension occurs on the rift. The faster opening rate in the south is a

Table 3.3. Estimated Block Motions

Block	East	North
S. Karakorum	-6.5±2.0	-15.8±0.6
N. Karakorum	-4.8±2.6	-18.9±0.8
S. YZS	-1.3±0.7	-12.1±0.5
N. YZS	1.3±1.1	-12.9±0.7
E. Yadong Rift	5.7±1.3	-18.9±1.0

All velocities in mm/yr relative to the Indian plate.

eastward and northward are positive;

westward and southward are negative;

YZS: Yarlung-Zangbo Suture.

S: south; N: North; E: east.

consequence of the termination of strike-slip motion (in our model) on the suture at that point. Direct measurements of the opening rate across the rift on both sides of the YZS will test whether the strike-slip motion does indeed terminate there.

Seven north-south trending rift systems characterize the present tectonics of southern Tibet [*Tapponnier* et al., 1981; *Armijo* et al., 1986, 1989], where it undergoes east-west extension. About one-half of the total extension rate between SHIQ and LHAS is concentrated along the Yadong-Gulu rift. This suggests that the assumption of uniform extension rate across all the seven rifts on which *Armijo* et al. [1986] based their estimation is wrong. Given the current spacing of GPS sites, we cannot rule out a total of ~1-2 mm/yr extension rate across the five rifts in central southern Tibet. We find 5-6 mm/yr extension across the Thakkola graben. This suggests that the block between the Thakkola graben and Yadong-Gulu rift north of the suture is quasi-stable, and almost all current extension is focused on these two rifts.

Given the relative motion between the block north of the Karakorum fault and west of the Thakkola graben and the quasi-stable block between the Yadong-Gulu rift and Thakkola graben north of the YZS, assuming blocks north of the KJFZ have the similar relative motion, we would expect a SW-NE trending left-lateral strike-slip fault (Figure 3.13) forms

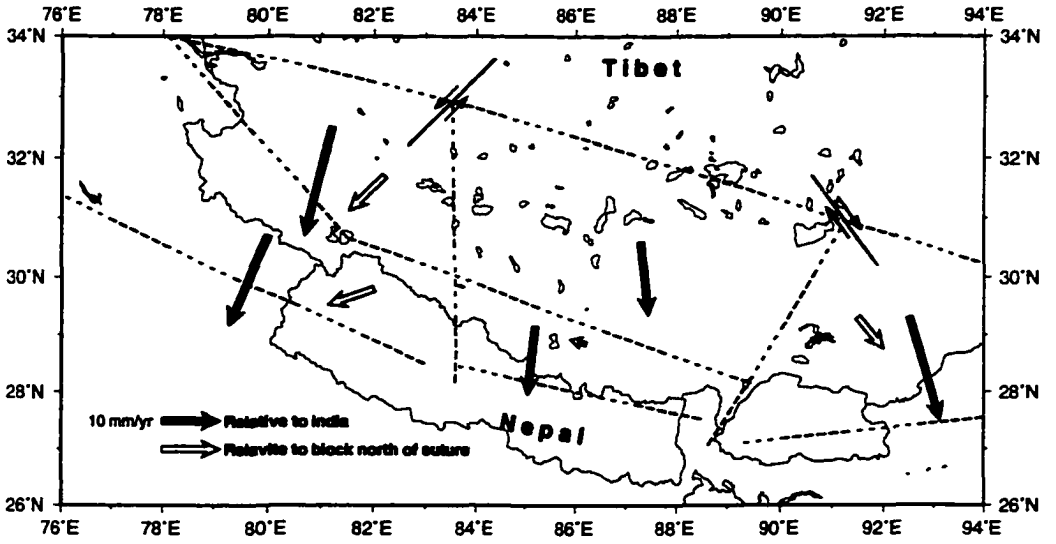

Figure 3.13. Estimated block velocities relative to the Indian plate (solid vectors) and the block north of the YZS between the Yadong-Gulu rift and Thakkola graben (open vectors). Block boundaries are shown as dashed lines; Solid line with opposed arrows: inferred faults.

the KJFZ to which the Thakkola graben links. Based on field observation, *Yin* et al. [1999] mapped this left-lateral strike-slip fault and suggested that such a left-lateral component was required by the east-northeast slip direction observed in northern Tibet. Similarly, the southeast-east relative motion between the block east of the Yadong-Gulu rift and the block between the Yadong-Gulu rift and Thakkola graben north of the YZS would require significant right-lateral components on the KJFZ where the Yadong-Gulu rift links (Figure 3.13). This inference is consistent with the result of a more detailed study on active *en échelon* strike-slip fault zones along the KJFZ at longitude of 90°E [*Armijo* et al., 1989].

The geometries of the two most active rifts in southern Tibet, the Thakkola graben and the Yadong-Gulu rift, as well as the relative block motions suggested in this study (Figure 3.13), may result in variations in the MHT convergence rates, as indicated in Figure 3.14. Given the overall trend of N30°E along the Yadong-Gulu rift [*Armijo* et al., 1986] and roughly north-south along the Thakkola graben [*Armijo* et al., 1986; *Mercier* et al., 1987], as the extension in Himalaya and southern Tibet, we would expect roughly N120°E and N90°E extension on the Yadong-Gulu rift and the Thakkola graben, respectively. In return, such an orientation of extension would drive variations in the MHT convergence

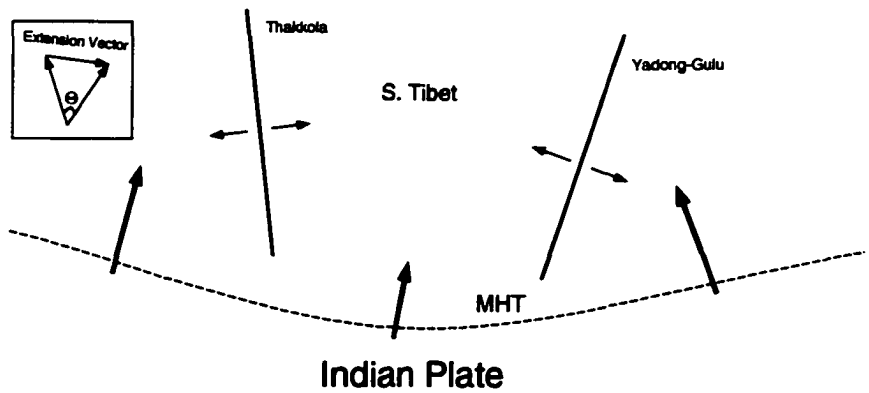

Figure 3.14. Sketch for kinematics of southern Tibet. Inset: simple model of *Molnar and Lyon-Caen* [1989]. MHT: Main Himalaya Thrust. Opening on the Yadong-Gulu rift and Thakkola graben results in faster convergence rates on the western and eastern Himalaya.

rates, implying the faster rates of convergence on the western and eastern segments than that on the central Himalaya.

Another possible local fault that plays a role in spatial non-uniform extension is the active right-lateral strike slip YZS with a rate of ~3 mm/yr. The area south of the YZS (including Nepal) moves to the west relative to Xigatse (Figure 3.2), meaning that the area north of the suture escapes eastward relative to India. *McCaffrey* et al. [1998] suggested that the extension in southern Tibet ought to be interpreted in terms of slip partitioning of oblique subduction, with the KJFZ serving as the strike-slip component of the partitioned deformation. We believe that the slip partitioning model is more appropriately applied to explain the right-lateral strike slip motion on the suture than on the KJFZ, which is located much farther to the north. However, the model of *McCaffrey* et al. [1998] predicted that the roughly arc-parallel extension in southern Tibet, which is a consequence of the frictional partitioning of slip, should not be greater than the convergence rate between India and Tibet. This conflicts with the extension rate we observed here that is much too high in relation with the convergence rate to be consistent with that explanation. We infer that in addition to the slip partitioning, another process source must also drive the extension in southern Tibet.

Pre-existing zones of weakness in Tibetan crust may be another possible explanation for the non-uniform extension in southern Tibet. Such zones of weakness have been suggested

as being caused by a partically molten mid-crustal layer existing beneath southern Tibet from INDEPTH geophysical and geological observations [*Nelson* et al., 1996]. However, a weak zone is unlikely to be present everywhere in southern Tibet based on the previous discussion. The existance of this zone implies that the upper crust of the Tibetan Plateau is regionally decoupled from the lower crust and mantle lithosphere below.

The arc-normal slip vectors of moderate earthquakes along the Himalayan arc, if India is assumed to be rigid, require ~N110°E extension of southern Tibet [*Ni and Barazangi*, 1984; *Baranowski* et al., 1984; *Molnar and Lyon-Caen*, 1989]. *Molnar and Lyon-Caen* [1989] suggested that if the convergence rate of India toward the Himalaya v_H is constant along the arc, we would expect an extension rate in southern Tibet of $v_T = v_H(2 - 2\cos\Theta)^{1/2} = 2v_H \sin(\Theta/2)$, where Θ is the difference in azimuths of slip vectors between easternmost and westernmost of the Himalaya, and v_H is the convergence rate (see inset in Figure 3.14). We suggest that the variations in extension rate, Δv_T, resulting from internal deformation of Tibet would drive the variations in convergence rate, Δv_H, along the Himalayan arc, such that $\Delta v_T = 2\Delta v_H \sin(\Theta/2)$ based on the simple model of *Molnar and Lyon-Caen* [1989]. Our observed different extension rates in southern Tibet and convergence rates on the three segments of the Himalaya are consistent with this simple model.

Gongbu (GNGB), 250 km east of Lhasa, moves at 13±3 mm/yr relative to Lhasa in the N110°E direction, suggesting the rate of extension is concentrated there. However, the velocity at GNGB cannot be explained by extending our block model farther east (unless we simply add another block east of Lhasa with only one site on it). Figure 3.3 shows that the average extension rate changes dramatically at the Yadong-Gului rift, and an intriguing possibility is that the extension rate may be higher in the easternmost part of the Himalayan arc. Geological evidence for well-developed rift systems east of Lhasa is lacking, so the interpretation of the motion of this site is not obvious. More GPS data between Gongbu and Lhasa will help improve our knowledge of east-west extension east of Lhasa in southern Tibet. If the variations of extension rates in the three segments are consistent with the variations in convergence rates according to the simple model of *Molnar and Lyon-Caen* [1989], we would expect over 30 mm/yr of convergence rate in the easternmost part of the Himalaya.

3.9 Conclusion

GPS velocities in southern Tibet show that 13±1 mm/yr of extension, roughly in the N110°E direction, occurs between Lhasa and Shiquanhe. The rate of extension is not uniform across all of southern Tibet, with extension concentrated across the Yadong-Gulu rift and the Thakkola graben system. The extension rate increases dramatically east of Lhasa, where no well-developed rift systems have been identified. An opening rate of 6.6±2.2 mm/yr along the Yadong-Gulu rift accounts for about one half of the total extension between Lhasa and Shiquanhe, while a quasi-stable block lies to the west of this rift and east of the Thakkola graben. Our results also suggest right lateral shear of 3±1 mm/yr on or near the YZS, extending from the Karakorum fault on the west to the Yadong-Gulu rift on the east. Sites north of the suture move slower in the N110°E direction than sites south of the suture, suggesting that the strike slip along the YZS may contribute some parts of the east-west extension in southern Tibet.

Our results suggest that arc-normal convergence directions along the Himalaya are in the directions of N25°E, N12°E, and N12°W in the western, central, and eastern segments of the Himalaya, respectively, consistent with slip vectors of moderate earthquakes along the Himalaya. We find slip rates of India beneath Eurasia to be 17±1, 12.2±0.4, and 19±1 mm/yr on the western, central, and eastern segments, respectively. We infer that the lower rate in the central Himalaya segment is significant, and the faster slip rates on the eastern and western Himalaya result from the geometries of the two most active rift systems, the Yadong-Gulu rift and Thakkola graben, in southern Tibet and the concentrated extension rates there.

Chapter 4

Strain Accumulation Across the Tibetan Plateau measured with GPS[1]

4.1 Abstract

Most past models have suggested that lithospheric deformation induced by the collision of India and Eurasia is accommodated by one of two dominant processes: (1) shortening and thickening of the crust, or (2) extrusion that transports material away from the collision via slip on a few large strike-slip faults. In this chapter, we use Global Positioning System (GPS) data from 44 sites across the Tibetan Plateau surveyed between 1991 and 2001 to show that neither process is presently dominant. Instead, a combination of shortening and extension resulting from many small active faults produces little net dilatation, and a state of strain in the plateau that approximates pure shear. The strain accumulation is spatially uniform across the plateau with maximum contraction is oriented in the direction of N32°E, comparable to the direction of the Indian plate motion relative to the Eurasian plate.

Several large-scale faults in the plateau also play an important role. Our results suggest that 5.9±0.7 mm/yr opening in the N69°W direction occurs on the Yadong-Gulu rift, and

[1]Manuscript in preparation with authors Q. Chen, J. T. Freymueller, Q. Wang, Z. Yang, C. Xu, and J. Liu

that this opening may extend as far north as the Nyainqentanglha range. We find 7.4±0.7 mm/yr of right-lateral slip on the Karakorum-Jiali Fault Zone (KJFZ), significantly slower than that previously estimated from offset geologic features. Our model and a 2-D screw dislocation model give lower and upper bounds, 4.4±1.1 and 10.3±0.4 mm/yr, respectively, on the slip rate on the Kunlun fault.

The eastward motion of central Tibet is as large as 50% of the convergence rate between India and Eurasia. However, this eastward motion is not motion of a relatively undeforming block bounded by rapidly moving strike-slip faults, as suggested by past extrusion models. Instead, we infer that much of this eastward motion is driven by the internal extension of the plateau. Conjugate strike-slip faulting is a plausible mechanism to accommodate the observed contraction and extension.

4.2 Introduction

The Tibetan plateau, a product of the ongoing collision between India and Eurasia, is a complex region with many earthquakes [*Molnar and Lyon-Caen*, 1989] and active faults [*Rothery and Drury*, 1984; *Armijo* et al., 1986]. The present-day tectonics of the Tibetan Plateau, and its origins and mechanisms have long fascinated researchers and have been subject to much debate. Many attempts have been made based on seismic, geologic, and geodetic data to solve these debates [*Molnar and Lyon-Caen*, 1989; *Peltzer and Saucier*, 1996; *England and Houseman*, 1986; *England and Molnar*, 1997; *Holt* et al., 1995, 2000; *Bilham* et al., 1997; *Larson* et al., 1997]. Regarding the principal mechanism assumed to accommodate the convergence of India, most of these efforts for lithospheric deformation of the Tibetan Plateau fall into one of two end-member categories: (1) shortening and thickening of the crust, or (2) extrusion that transports material away from the collision via slip on a few large strike-slip faults. Recently, *Wang* et al. [2001] presented a kinematic description of deformation in China constrained by Global Positioning System (GPS) measurements. In this chapter, we focus on the velocity field in the Tibetan Plateau, using a subset of an improved version of the *Wang* et al. [2001] dataset (see later discussion), and show that neither process is presently dominant. We find that strain accumulation is quite uniform across the plateau and can be well described by a combination of block motion, pure shear

and uniaxial contraction.

The prominence of large strike-slip faults in Asia led *Molnar and Tapponier* [1975] and *Tapponnier and Molnar* [1977] to suggest that much of the convergence which is not absorbed in the Himalaya must be converted into horizontal movements, predominantly the eastward displacement or extrusion of Tibet and southern China [*Tapponier* et al., 1986]. Following this suggestion, [*Armijo* et al., 1989] proposed that a set of overlapping strike slip faults at ~32°N represented a throughgoing right-lateral shear zone, termed this the Karakorum-Jiali Fault Zone (KJFZ), and suggested that it separates the east-west extending southern Tibet from relatively undeformed northern Tibet. They proposed that the region between the KJFZ and Altyn Tagh and Kunlun faults on the northern edge of Tibet moved eastward as a relatively unformed block, absorbing at least 30% of the convergence. Other estimates of convergence accomodated by lateral extrusion range from 15% from a strain rate description model [*England and Molnar*, 1997], 10-25% from geomorphic evidence [*Molnar* et al., 1987], and up to 50% from a kinematic block model [*Avouac and Tapponnier*, 1993]. Most of these descriptions of deformation have assumed that regions bounded by major strike-slip faults are relatively undeformed.

In contrast, other numerical models proposed that deformation of the Himalaya and Tibet is dominated by shortening and crustal thickening [e.g., *Houseman and England*, 1993]. One category of these models is dynamic models, usually a thin viscous sheet [e.g., *England and Houseman*, 1986; *Houseman and England*, 1993], which regards the behavior of continental lithosphere as a continuum. One advantage of these models is the ability to include the presence of body forces associated with crustal thickness. These models have been used to explain the history of crustal thickening in Tibet, and to propose that up to 75% of the convergence between India and Eurasia was accommodated by crustal thickening. However, these models produce limited eastward displacement in Tibet and ignore the effects of major strike-slip faults.

Recently, *Wang* et al. [2001] published a self-consistent velocity field for 354 GPS sites in China and Nepal, and discussed the large-scale kinematic implications for Asia. We use a subset of this velocity field to answer several major tectonic questions regarding the Tibetan Plateau: is the deformation caused by the continental coillision between India and Eurasia distributed across the entire plateau or localized on major faults? Is lateral extrusion

or crustal thickening dominant in absorbing the convergence? Is the strain accumulation spatially variant or uniform? How fast is the eastward extrusion of eastern Tibet? Does it result only from large-scale strike-slip faulting, as proposed by *Armijo* et al. [1989]? If not, what is an alternative tectonic source?

In this chapter, we address these questions using GPS measurements at 44 sites in Tibet. First, we spatially evaluate the strain accumulation in the plateau and suggest that the deformation of Tibet can be understood as being distributed, then we show that the observed kinematics is quite uniform across the Tibetan Plateau, and can be described as a combination of rigid block motion, pure shear, and uniaxial contraction. Finally, we will discuss our predicted velocity field in comparison with other numerical models.

4.3 GPS Data and Analysis

4.3.1 GPS Data

We have collected a rich GPS data set in the Tibetan Plateau and its neighboring regions through the collaborative efforts of many researchers in the United States and China. GPS data were collected between January 1991 and January 2001 as part of four separate efforts by seven institutions, and have been analyzed and merged with all other data in China into a single, self-consistent velocity field [*Wang* et al., 2001].

The GPS sites discussed in this study are located on the Tibetan Plateau north of the Yarlung-Zangbo Suture (YZS). Some sites are scattered to the west of Lhasa, but most of them are concentrated along a profile oriented roughly N32°E (Figure 4.1), the approximate contraction direction of India-Eurasia convergence, extending about 1400 km from Lhasa in the south to the Qilian Shan in the north. The profile extends across several major geologic features: the KJFZ, the Nyainqentanglha range, the Kunlun fault, the Qaidam basin, Nan Shan, and Qilian Shan (Figure 4.1). Table 4.1 summarizes the survey history of these sites.

4.3.2 GPS Data Analysis

The GPS data presented in this chapter were analyzed using the GIPSY/OASIS II software (release 6) developed at the Jet Propulsion Laboratory [*Zumberge* et al., 1997]. Raw GPS data collected in the field were analyzed in 24-hour daily solutions along with regional and

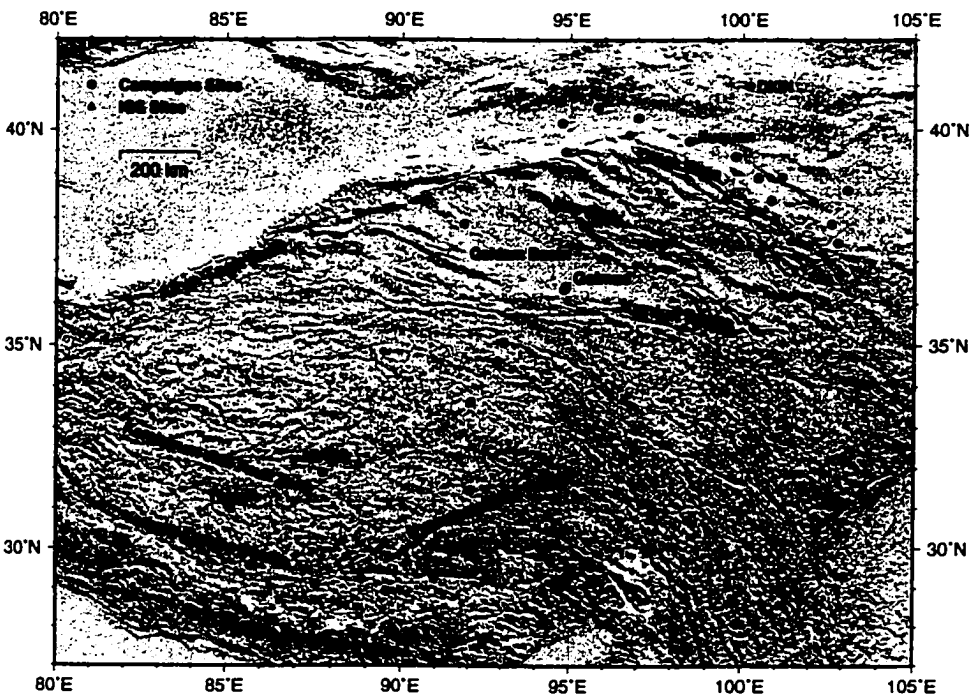

Figure 4.1. Shaded relief map showing the sites used in Tibet.

Table 4.1. GPS Sites Observed in the Tibetan Plateau

Site	ID	Latitude deg	Longitude deg	Height m	Observation First	Observation Last	Agency
Anduo	ANDU	32.2753	91.6926	4654.1169	1993.45	2000.41	SSB[1]-WTUSM[2]
Anxi	ANXI	40.5139	95.8004	1116.8204	1993.51	1999.66	SSB
Bala	BALA	29.7361	90.7979	3808.0259	1991.23	2000.43	UAF-Xi'an[3]
Budongquan	WT02	35.5199	93.9129	4554.2535	1993.55	1997.43	WTUSM
Chanma	CHMA	39.9027	96.7475	2062.8875	1993.51	1999.66	SSB
Dacaidam	DACA	37.8336	95.3766	3153.7739	1993.43	1999.65	SSB
Dagze	DAGZ	29.6633	91.3634	3648.4792	1991.23	1998.68	UAF-Xi'an
Delingha	DELI	37.3773	97.7295	3156.2186	1993.43	1999.66	SSB
Delingha	DLHA	37.3805	97.3778	2955.7811	1998.65	2000.54	CMONOC[4]
Dingxin	DXIN	40.9837	100.2006	1017.9556	1998.66	2001.04	CMONOC
Dunhuang	DUNH	40.1569	94.7582	1059.4178	1993.51	1999.66	SSB
Erbo	ERBO	37.9612	100.9305	3357.5284	1993.49	1999.70	SSB
Erdaogou	WT03	34.6305	92.8538	4727.7407	1993.55	1997.48	WTUSM
Gaotai	GAOT	39.4096	99.8144	1301.5513	1993.49	1999.70	SSB
Golmud	GLMD	36.3465	94.8306	2835.5171	1992.79	1995.87	WTUSM
Golmud	GOLM	36.4327	94.8745	2749.9440	1991.23	2000.40	SSB
Gonggar	GGAR	29.2780	90.9588	3551.5462	1998.63	2000.44	UAF-Xi'an
Gulang	GULA	37.4380	102.8449	2178.8891	1993.47	1999.72	SSB
Haergai	HAER	37.2173	100.4824	3237.0616	1993.49	1999.70	SSB
Hexibu	HEXI	38.3929	102.1020	1668.3413	1993.52	1999.72	SSB
Hongshihu	HONG	38.9359	101.1520	1892.7495	1993.49	1999.72	SSB
Hotspring	SHOT	29.5911	85.7409	5019.4474	1998.70	2000.48	UAF-Xi'an
J010	J010	31.1620	97.1692	3595.4862	1999.37	2000.39	CMONOC

Continued

Site	ID	Latitude deg	Longitude deg	Height m	Observation First	Observation Last	Agency
Jiangze	JIAN	28.9142	89.5728	3981.2922	1993.49	1998.70	SSB
Jiuquan	JIUQ	39.7582	98.4962	1404.4690	1992.79	1999.68	SSB
Lhasa	LHAS	29.6573	91.1040	3629.1804	1995.43	2000.50	IGS
Lhaze	LAZE	29.1181	87.5766	3982.6581	1998.69	2000.41	UAF-WTUSM
Mangnai	MANG	37.8870	91.8213	2876.2020	1994.65	1998.58	CU[5]
Minle	MINL	38.4148	100.8301	2291.9593	1993.49	1999.69	SSB
Minqing	MINQ	38.6451	103.1134	1312.4758	1993.52	1999.73	SSB
Nagqu	NAGQ	31.4687	92.0356	4455.3687	1993.46	1998.71	SSB-WTUSM
Nyma	NYMA	31.8908	87.7656	4509.9556	1998.66	2000.47	CMONOC
Qilian	QILI	38.1902	100.2361	2675.7490	1993.49	1999.69	SSB
Qingshizui	QING	37.4787	101.4254	2915.4773	1993.48	1999.70	SSB
Soxian	SOXI	31.8903	93.7837	3961.8118	1993.46	2000.42	SSB-WTUSM
Shubei	SUBE	39.5145	94.8568	2089.1467	1993.43	1999.65	SSB
Tcoqin	TCOQ	31.0186	85.1392	4654.3968	1998.69	2000.47	UAF-Xi'an
Wudaoliang	WUDA	35.0878	93.0518	4730.9690	1998.66	2000.47	CMONOC
Wuwei	WUWE	37.8858	102.6522	1531.6386	1993.47	1999.72	SSB
Xigaze	XIGA	29.2498	88.8643	3867.3193	1991.27	1998.43	UAF-WTUSM
Yanshiping	WT04	33.6492	92.0563	4649.2468	1993.56	2000.42	WTUSM
Yieniugou	YIEN	38.4446	99.5648	3248.9569	1993.49	1999.68	SSB
Yumen	YUME	40.2848	97.0120	1457.0728	1993.50	1999.66	SSB
Yushu	YUSH	32.9972	96.9880	3911.3364	1998.66	2000.47	CMONOC
Zhangyie	ZHAN	38.9269	100.4480	1427.2951	1993.49	1999.69	SSB

1. State Seismological Bureau of China.

2. Wuhan Technical University of Surveying and Mapping (now Wuhan University).

3. University of Alaska Fairbanks, USA and Chang'an University, China.

4. Crustal Movement Observation Net of China.

5. University of Colorado, Boulder, USA.

Latitudes, longitude, and heights are referenced to the WGS84 ellipsoid.

global permanent sites. All individual daily free network solutions were transformed into the ITRF97 reference frame and combined together to determine site velocities by standard weighted least squares techniques. A more detailed description of the analysis methods is given by *Freymueller* et al. [1999, 2000] and *Wang* et al. [2001]. We use an updated version of the velocity solution of *Wang* et al. [2001]. We fixed antenna height errors at a few sites, fixed a reference clock problem that biased a few solutions, excluded a few outlier measurements, and included more available data. About 60% of the solutions used in *Wang* et al. [2001] were improved in some way, although most changes were minor.

For ease of interpretation, we express our velocities either relative to Lhasa (LHAS), an International GPS Service (IGS) site in Tibet, or relative to the Eurasian plate, by subtracting the motion of LHAS or the Eurasian plate relative to the ITRF97 reference frame, respectively. In the past, the definition of a Eurasian-fixed reference frame has been notably difficult. Relative to ITRF97, *Wang* et al. [2001] estimated that the Eurasian plate rotates at $0.2523\pm0.0035°\,\mathrm{Myr}^{-1}$ about a pole at $56.9\pm0.3°$N, $104.3\pm0.3°$W. More recently, using more data, *Sella* et al. [2002] presented the REVEL model, which shows that the Eurasian plate rotates at $0.257\pm0.003°\,\mathrm{Myr}^{-1}$ about a pole at $58.27\pm1.2°$N, $102.21\pm0.8°$W (relative to ITRF97). These two estimates are in a good agreement, with REVEL predicting site velocities in Tibet that differ by no more than 1 mm/yr from those of *Wang* et al. [2001]. We use the REVEL model of *Sella* et al. [2002] to define a Eurasian-fixed reference frame in this study.

4.4 GPS Velocity Field

Figure 4.2 shows the GPS velocity field relative to Lhasa (LHAS), about 150 km east of the Yadong-Gulu rift. Site velocities on the west of the Yadong-Gulu rift and south of the KJFZ show that southern Tibet is undergoing east-west extension (Chapter 3). XIGA and JIAN, west of the rift, move at about 7 ± 1 mm/yr and 6 ± 1 mm/yr in the direction of N45°W relative to Lhasa, implying that 6-7 mm/yr extension occurs across the Yadong-Gulu rift. In Chapter 3, we estimated an opening rate of 6 ± 2 mm/yr based on a 3D self-consistent block model for southern Tibet. The site NYMA, located just north of the KJFZ, moves about 4 ± 1 mm/yr westward, and NAGQ, about 400 km east of NYMA at the same latitude,

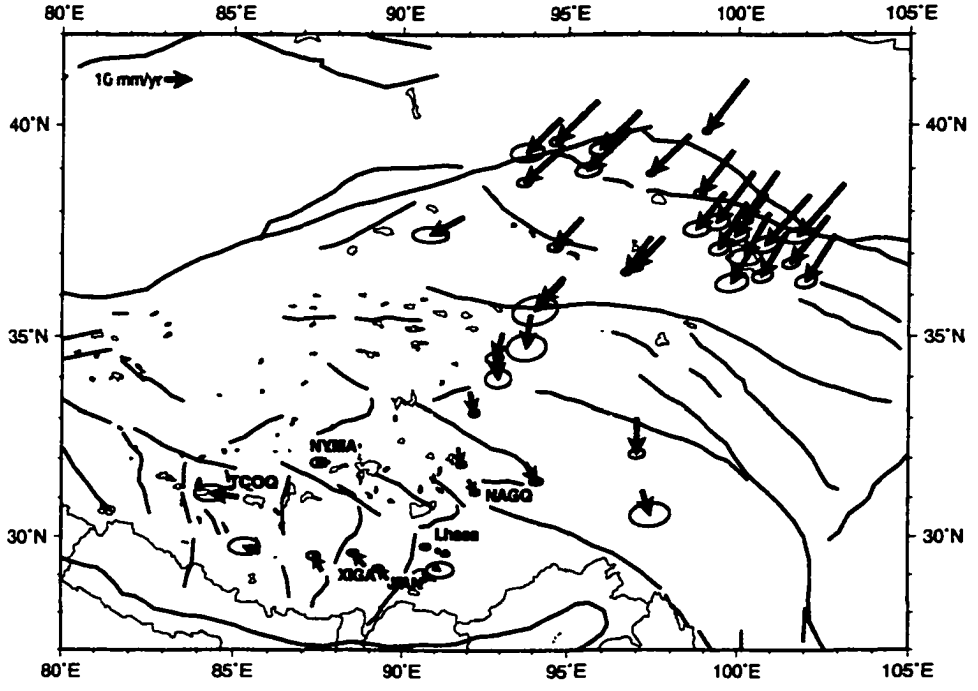

Figure 4.2. GPS velocites 1991-2001 for sites in the Tibetan Plateau and Qilian Shan area, relative to Lhasa (LHAS). Lhasa is shown as a solid circle. Uncertainties are 95% confidence ellipses.

moves about 3±1 mm/yr eastward, again relative to Lhasa. Thus, the concentrated east-west extension associated with the rift must extend north of the KJFZ, and may extend across a significant portion of the Tibetan Plateau. There is no GPS data from western Tibet north of NYMA.

Sites between the KJFZ and Kunlun fault move eastward relative to Lhasa, suggesting that the Tibetan Plateau south of the Kunlun and north of the KJFZ is being extruded to the east. As noted by *Wang* et al. [2001] and *Holt* et al. [2000], eastward site velocities increase steadily northward from the Himalaya across the Tibetan Plateau, then decrease rapidly across the Kunlun fault, at the northern margin of the Plateau.

The distributed nature of deformation across the Tibetan Plateau can be shown best by projecting site velocities onto a single profile constructed parallel to the maximum contrac-

tion direction of the Indian plate relative to Eurasia (Figure 4.3). The profile is oriented N32°E (see later discussion). The velocity gradient in the N32°E direction (Figure 4.3a) is surprisingly linear from just north of the Yarlung-Zangbo suture to north of the Qilian Shan, a distance of ~1400 km, and the average contractional strain rate in this direction is 16.4±0.3 nanostrain/yr. For comparison, deformation within the San Andreas Fault system in California is concentrated in a zone of 100-150 km in width [e.g., *Freymueller* et al., 1999; *Bennett* et al., 2002]. This linearity led *Wang* et al. [2001] to conclude that distributed deformation rather than block-like motion characterizes present-day tectonics of the Tibetan Plateau. This seems to be limited to the plateau itself, because rigid block-like motion characterizes deformation of the region to the north [*Shen* et al., 2001b]. Later we will show that broadly distributed deformation may extend to north of the Qilian Shan between 90°E and 100°E.

However, the velocity components in the N122°E direction (Figure 4.3b) suggest that although uniform shortening is seen across the whole plateau, some major faults such as the KJFZ, Yadong-Gulu rift, and Kunlun fault localize significant shear deformation. There are four groups of velocities in the N122°E direction as indicated by dashed lines in Figure 4.3b. West of the Yadong-Gulu rift, sites move about 6 mm/yr westward relative to the sites east of the rift. Tcoqin (TCOQ), located further to the west, moves slightly faster westward. Across the KJFZ from TCOQ to NYMA and across the Kunlun fault from WT02 to GOLM, the N122°E components change by 6 mm/yr and 8 mm/yr, respectively. These discontinuities in the velocity field result from right-lateral strike slip motion across the KJFZ and left-lateral strike-slip motion across the Kunlun fault.

4.5 Strain Models

To model strain accumulation and rotation rates within an area, from the theory of infinitesimal strain, we approximate that the observed site velocities are composed of three components: rigid body translation, strain rate, and rotation rate. In a two-dimensional Cartesian coordinate system, the approximation is [e.g., *Savage* et al., 2001; *Jaeger*, 1964].

$$\dot{u}_x = \dot{U}_x + \dot{\varepsilon}_{xx}\Delta x + \dot{\varepsilon}_{xy}\Delta y + \dot{\omega}\Delta y, \tag{4.1}$$

$$\dot{u}_y = \dot{U}_y + \dot{\varepsilon}_{xy}\Delta x + \dot{\varepsilon}_{yy}\Delta y - \dot{\omega}\Delta x, \tag{4.2}$$

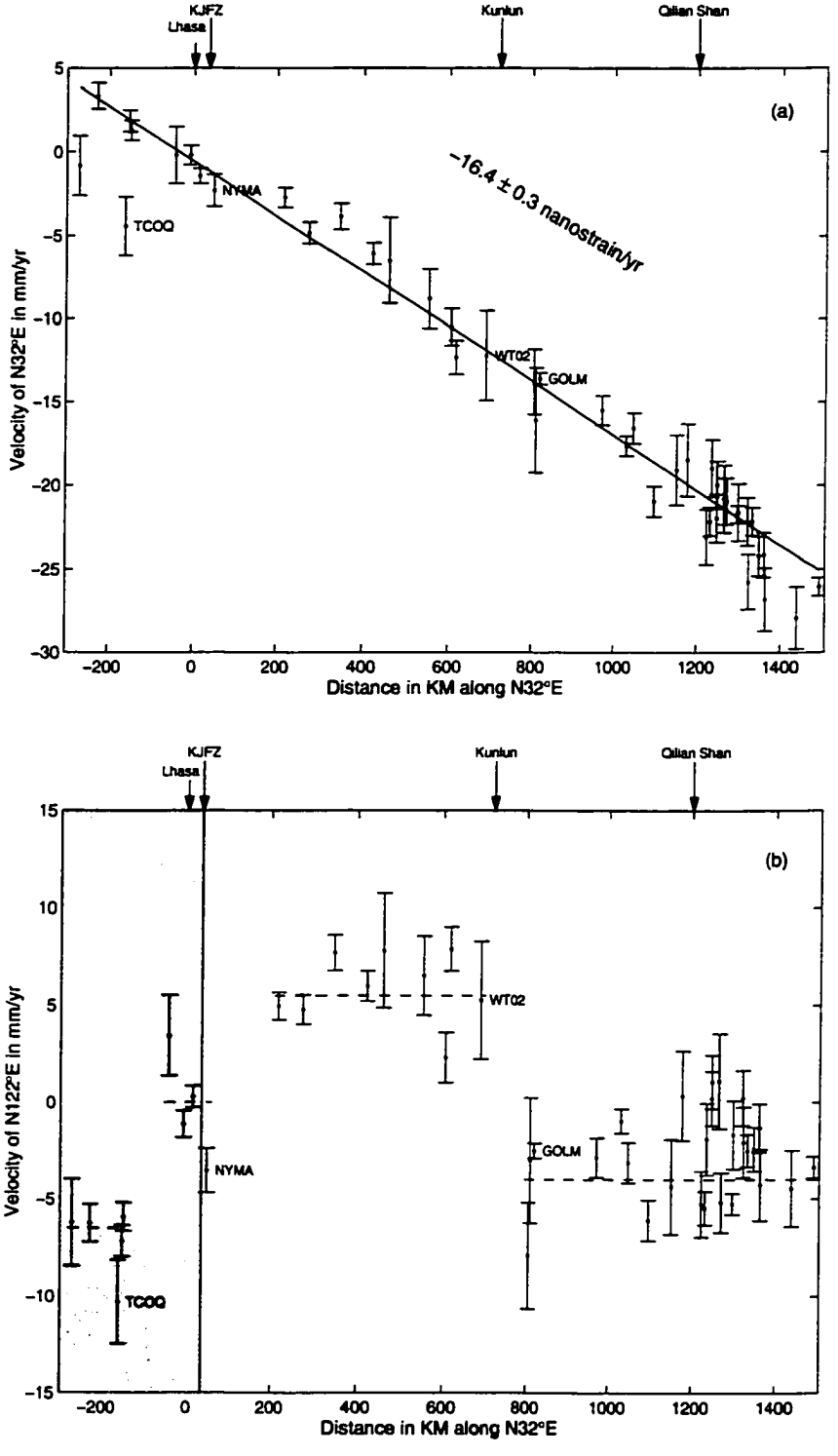

Figure 4.3. Velocity components as a function of distance along a N32°E profile (relative to LHAS) in (a) the N32°E direction; (b) the N122°E direction. The error bars represent one standard deviation. The region of southern Tibet south of the KJFZ is shaded where the large graben systems are found [*Armijo* et al., 1986]. This region is discussed in more detail in Chapter 3.

where $\dot{u}_x$ and $\dot{u}_y$ are the velocities at a point, $\dot{U}_x$ and $\dot{U}_y$ are the velocities at the centroid of the concerned area, Δx and Δy are the distances from the centroid, $\dot{\varepsilon}_{xx}$, $\dot{\varepsilon}_{xy}$, and $\dot{\varepsilon}_{yy}$ are the tensor strain rate components, and $\dot{\omega}$ is the rotation (Note that here rotation is reckoned positive in the clockwise sense as viewed from above the earth).

If an active fault crosses such an area, then deformation within this area can be decomposed into two parts: distributed and localized deformation, described by a strain tensor and an additional constant block motion, respectively. So equations (4.1) and (4.2) can be revised to strain rate plus block motion as follows:

$$v_x = V_x + \dot{\varepsilon}_{xx}\Delta x + \dot{\varepsilon}_{xy}\Delta y + \dot{\omega}\Delta y, \tag{4.3}$$

$$v_y = V_y + \dot{\varepsilon}_{xy}\Delta x + \dot{\varepsilon}_{yy}\Delta y - \dot{\omega}\Delta x, \tag{4.4}$$

where $v_x = \dot{u}_x - \dot{U}_x$ and $v_y = \dot{u}_y - \dot{U}_y$ are the velocities at a point relative to the reference point, V_x and V_y are the velocities of a block on which the point is located. Then given the motions of at least three geodetic monuments, one can solve for the six unknowns $V_x, V_y, \dot{\varepsilon}_{xx}, \dot{\varepsilon}_{xy}, \dot{\varepsilon}_{yy}$, and $\dot{\omega}$ using linear least squares methods. We can use either a particular site or a stable plate as reference for the velocities.

In our study area, we treat the Yadong-Gulu rift, KJFZ and Kunlun fault as block boundaries, and separate the Tibetan Plateau into four fault-bounded blocks: east and west of the Yadong rift, north of the KJFZ and south of the Kunlun fault, and north of the Kunlun block. Each block has its own velocity V. Figure 4.4 outlines these block boundaries. Two different models are tried in this study: (1) assuming these blocks to be rigid, we estimate the velocity and rotation rate for each block; (2) assuming these blocks to be deforming, we estimate the average strain rate and rotation rate in each block. We find that rigid blocks cannot explain the data present here with the weighted model misfit per degree of freedom of 10.2, about a factor of five worse than the best deforming block model. So we treat these blocks to be deforming in this study.

4.5.1 Spatial Variations in Strain Rate

In order to test for spatial variation of strain rates across the Tibetan Plateau, we have organized the 44 GPS sites into several subregions categorized in two types: regions bounded by major faults, and regions crossing major faults. We define four "fault-bounded" subregions

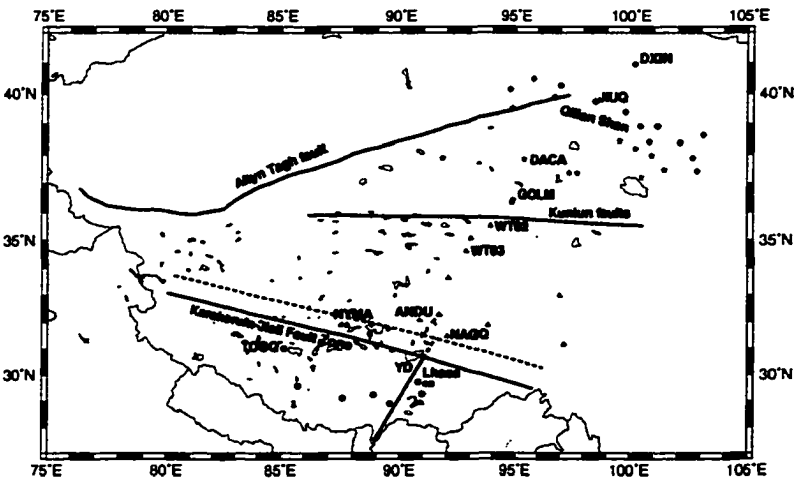

Figure 4.4. Map outlining the block boundaries and subregions discussed in the text. Solid lines with label: block boundary. Dashed lines: hypothesized boundary where the Yadong-Gulu rift extends northward and terminates. Solid circles: sites in the S. KJFZ region. Triangles: sites in the KJFZ-Kunlun region. Stars: sites in the Kunlun-Qilian region. Diamonds: sites in the N. Qilian region. YD: Yadong-Gulu rift.

seperated by the KJFZ, Kunlun, and Qilian Shan: the S. KJFZ subregion consists of eight sites located south of the KJFZ and north of the YZS; the KJFZ-Kunlun subregion has 10 sites located between the KJFZ and Kunlun faults; the Kunlun-Qilian subregion has 11 sites between the Kunlun and Qilian Shan; the N. Qilian region consists of 15 sites. Although we include the Yadong-Gulu rift as a block boundary, we do not define a subregion east of the rift because there are only four sites on the east of the rift (GGAR, DAGZ, BALA, and LHAS), one of them we use as the reference site (LHAS), and another site (GGAR) has a large velocity uncertainty. This region is discussed in more detail in Chapter 3. Four different symbols in Figure 4.4 are used to distinguished the sites in the different subregions. The fault-bounded regions are intended to define strain accumulation within the individual blocks.

Two contiguous fault-bounded subregions can be combined to be a "fault-crossing" region. The crossing KJFZ region consists of the S. KJFZ and KJFZ-Kunlun subregions, the crossing Kunlun region combines the KJFZ-Kunlun with the Kunlun-Qilian subregions, and the crossing Qilian region consists of the Kunlun-Qilian and N. Qilian regions. The fault-crossing regions are designed to define strain accumulation across the major faults. Finally, we define larger subregions that span multiple blocks to aid in the comparison of strain rates over the entire Plateau. Whenever sites on both sides of the major faults are used, we estimate the relative motion of the two blocks separated by the fault, and a single uniform strain model.

4.5.2 Strain Accumulation and Rotation Rates

Equations (4.3) and (4.4) are applied to estimate the strain accumulation and rotation rate in each subregion, as well as block motions relative to the reference site. Table 4.2 summarizes the results for each subregion. The principal strain rates and the azimuths of the axis of maximum contraction rate (measured clockwise from north) are shown in Table 4.2 column 3 through column 5. In column 6 and column 8, the maximun tensor shear strain rate $(\dot{\varepsilon}_1 - \dot{\varepsilon}_2)/2$ and the areal dilatation rate $(\dot{\varepsilon}_1 + \dot{\varepsilon}_2)$ are shown, respectively. The rotation rate about the local vertical is shown in column 7 (a clockwise rotation as viewed from above is positive). The final column in Table 4.2 shows the reduced chi-square (χ^2) for the model (uniform strain rate plus block motion) fit to the data. The values of the

reduced χ^2 in the last column are used to evaluate the goodness of fit of each model. Table 4.3 shows the estimated block motions using the data in each region.

We use the strain rates in the subregions to investigate the spatial variations of strain accumulation across the Tibetan Plateau to north of the Qilian Shan. The observed principal strain rates $\dot{\varepsilon}_1$ and $\dot{\varepsilon}_2$ are nearly constant over most of the plateau. The extension rate ranges from 7.4±1.7 to 10.1±2.3 nanostrain/yr and the contraction rate varies from 16.5±0.3 to 20.8±2.0 nanostrain/yr in magnitude for each region, except for the S. KJFZ subregion. The magnitude of the contraction rate is roughly twice that of the extension rate (Table 4.2 and Figure 4.5a), and the magnitude of the maximum shear strain and dilatation rates are roughly constant through out all subregions (Table 4.2 and Figure 4.5b).

The orientation of the maximum contraction (Table 4.2 column 5) varies little over all of the regions shown in Table 4.2, and is comparable with the India-Eurasia convergence direction [*Sella* et al., 2002]. Note that the azimuth of the maximum contraction in the "S. KJFZ" subset has a large uncertainty, and is marginally consistent with those in other regions. The model misfit in the "S. KJFZ" is significantly larger than those in other networks, implying that the site velocities south of the KJFZ are more heterogeneous than in the rest of the plateau, and cannot be interpreted by the uniform strain plus block motion model. In Chapter 3, we documented non-uniform east-west extension in southern Tibet, and we expect to see more rapid north-south contraction across the Himalaya than across the Tibetan Plateau [*Bilham* et al., 1997; *Larson* et al., 1999; *Wang* et al., 2001]. This is manifested in the larger maximum compressional strain that we observe there.

The strike of the vertical plane across which left-lateral shear is the greatest (azimuth of maximum contraction + 45°) for each subregion is about N78°E, implying that strain across the entire plateau in the east-west direction is dominated by left-lateral shear. Much left-lateral shear is concentrated in major sinistral shear zones, such as the Altyn Tagh or Kunlun faults on northern edge of the plateau. Note that we have already included these major shear zones through the relative block motions, so this means that the strain *between* the major faults is similar to that *on* the major faults. The ~N80°E strike of the Altyn Tagh fault is more comparable with that of the vertical plane across which left-lateral shear is the greatest, whereas the strike of the Kunlun fault is ~10-20° clockwise of this. The slip rates of the two faults are comparable [*Wang* et al., 2001].

Table 4.2. Tensor Strain and Rotation Rates in the Tibetan Plateau

Subregion[a]	Number of sites	$\dot{\varepsilon}_1^b$ *nstrain/yr*	$\dot{\varepsilon}_2^c$ *nstrain/yr*	Azimuth[d] deg	$(\dot{\varepsilon}_2 - \dot{\varepsilon}_1)/2$ *nstrain/yr*	$\dot{\omega}$ *nrad/yr*	$\Delta = (\dot{\varepsilon}_1 + \dot{\varepsilon}_2)$ *nstrain/yr*	Reduced χ^2
S. KJFZ	8	-41.3±11.6	11.9±5.4	37.6±5.2	26.6±7.3	-18.0±7.8	-29.3±10.7	3.39
KJFZ-Kunlun	10	-20.5±2.2	7.8±2.5	32.0±3.3	14.1±1.8	0.6±1.8	-12.7±3.2	1.63
Kunlun-Qilian	11	-16.5±0.3	10.1±2.3	33.1±3.0	13.3±1.1	-1.1±1.1	-6.4±2.4	1.12
N. Qilian	15	-17.3±0.3	7.4±1.7	32.9±2.4	12.3±0.8	-2.4±0.8	-9.9±1.8	1.75
Crossing KJFZ	18	-20.7±2.0	7.5±1.7	27.9±2.7	14.1±1.3	-1.0±1.5	-13.1±2.6	2.45
Crossing Kunlun	21	-18.1±1.7	8.1±2.1	31.3±3.0	13.1±1.5	-0.1±1.5	-10.0±2.3	1.36
Crossing Qilian	26	-17.0±0.2	7.4±1.5	33.0±2.1	12.2±0.7	-2.0±0.7	-9.6±1.5	1.72
All Data	44							
Two-strain		-20.8±2.0	8.1±2.1	28.5±2.8	14.5±1.5	-1.4±1.6	-12.8±2.7	
		-18.9±0.8	8.6±1.6	33.1±2.0	13.8±0.9	-3.5±0.9	-10.3±1.7	1.95
One-strain		-19.2±0.7	8.6±1.3	32.6±1.3	13.9±0.8	-3.2±0.7	-10.5±1.4	1.94
No internal strain		-	-	-	-	-	-	10.2

a. Subregions are designed to be "fault-bounded" and "crossing fault". See text for details.

b. Maximum contraction rates.

c. Maximum extension rates.

d. Azimuth of the contraction rate axis measured clockwise from north.

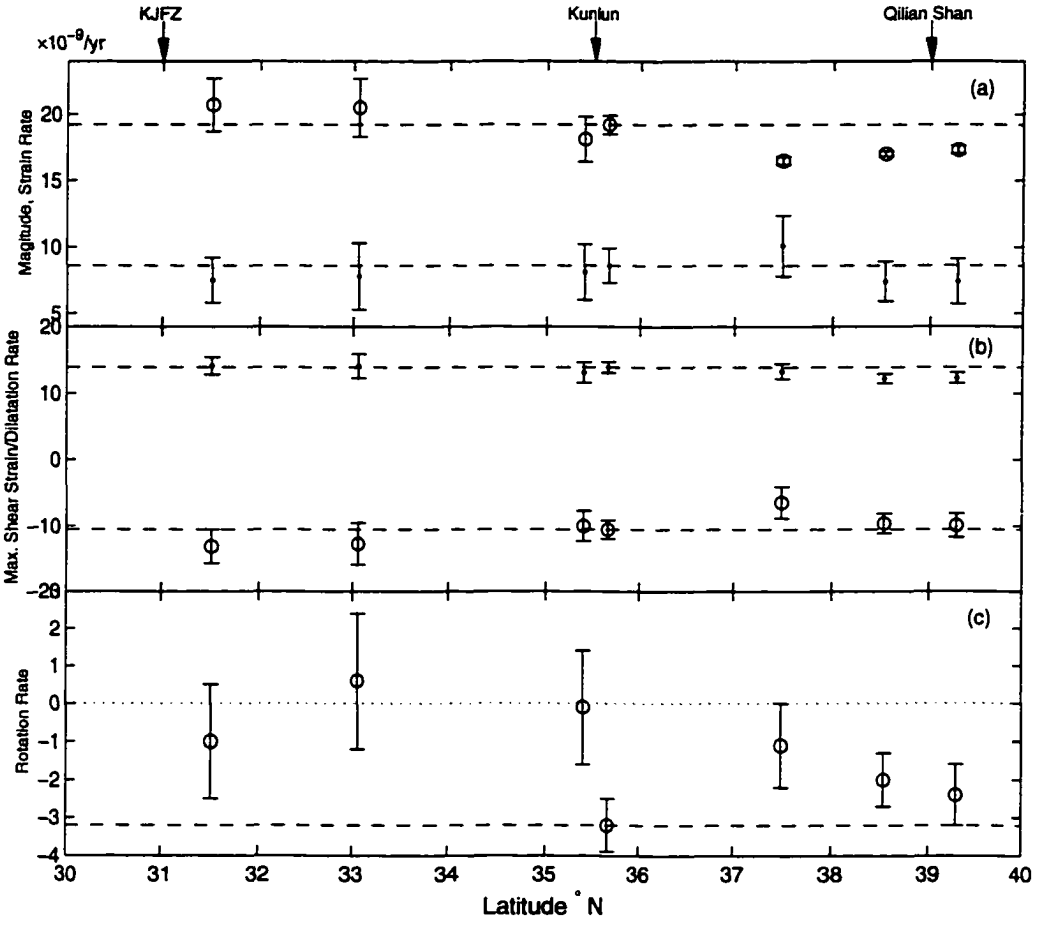

Figure 4.5. Principal strain rates vs mean latitude for the subregions described in Table 4.2. (a) Dot: extension rates; Circle: contraction rates. (b) Dot: maximum shear strain rates; Circle: dilatation rates; (c) Rotation rate. In all cases, the error bars represent one standard deviation, and the average values from the "one-strain" model are indicated by dashed horizontal lines.

Table 4.3. Estimated Block Motion in each Region

	W. Yadong Rift		S. Kunlun Fault		N. Kunlun Fault	
Network	East	North	East	North	East	North
S. KJFZ	-8.7±2.3	2.0±1.2				
KJFZ-Kunlun	-6.9±1.9	0.4±1.1	5.8±1.2	-1.5±0.7		
Crossing KJFZ	-5.2±0.8	1.6±0.4	5.7±0.9	-1.2±0.7		
Crossing Kunlun	-6.3±1.9	1.4±0.9	5.5±1.0	-2.3±0.6	0.8±2.1	2.2±1.2
All Data						
Two-strain	-5.1±0.8	1.6±0.4	6.0±1.1	-1.3±0.6	2.9±1.2	1.0±0.7
One-strain	-5.5±0.6	2.1±0.3	7.0±0.6	-2.5±0.3	2.6±1.1	1.5±0.7
No internal strain	-4.7±0.5	5.0±0.5	-1.0±0.6	-6.5±0.3	-18.5±0.7	-10.5±0.4

Block motion relative to Lhasa, in mm/yr.

The rotation rates given in Table 4.2 are about the local vertical through the reference station Lhasa. The observed rotation rates are not significant for the regions south of the Qilian Shan (crossing KJFZ, KJFZ-Kunlun, YZS-Kunlun, crossing Kunlun, and Kunlun-Qilian), but are significant for the regions including sites from the Qilian Shan-Nan Shan thrust belts (Table 4.2 and Figure 4.5c), with which the Altyn Tagh fault links. The velocities of sites in the Qilian Shan-Nan Shan are affected by the local deformation resulting from a young and rapidly uplifting series of parallel ranges bounded by active thrusts [*Burchfiel* et al., 1989; *Tapponnier* et al., 1990; *Meyer* et al., 1998].

Because the tensor strain rate is consistent in each principal region, the strain field across the Tibetan Plateau is best summarized by the next to last entry in Table 4.2, and the relevant block motions are shown in Table 4.3, representing the average deformation across the 44 GPS stations shown in Figure 4.1. We combined all 44 sites as a single network and use one uniform strain rate tensor plus block motions to describe the GPS velocities. The averaged principal strain rates are consistent with subregions (Table 4.2 and Figure 4.5), implying that the deformation is spatially uniform across the Tibetan Plateau, and can be fit by a single uniform strain rate tensor plus block motion model (hereafter referred to as "one-strain" model).

We also analyzed the data as two independent networks separated by either the Kunlun fault or the Qilian Shan, and used two independent strain rate tensors plus block motions

(referred to as "two-strain" models). Again, the estimated principal strain rates and the azimuths of the maximum contraction direction for the two subregions are not significantly different (Table 4.2), consistent with those estimated from the "one-strain" model. The total χ^2 of the "two-strain" model fitting all the data does not improve significantly from the "one-strain" model; an F-test shows that the improvement in χ^2 is not significant at the 95% confidence level. Thus we prefer the "one-strain" model.

For all data as a combined solution, we also tried a rigid block model in which the four blocks defined in Figure 4.4 were assumed to be rigid. We estimated the velocity and rotation rate about the local vertical through the reference station Lhasa. The model poorly fit the data with an extremely high reduced χ^2 of 10.2 (Table 4.2), predicting 6.5±0.3 and 4.0±0.4 mm/yr (Table 4.3) contraction across the KJFZ and Kunlun, respectively, which have been suggested to be strike slip faults [*Armijo* et al., 1989; *van der Woerd* et al., 2000]. This suggests that the hypothesis of rigid blocks can be rejected.

4.6 Discussion

4.6.1 State of Strain in the Tibetan Plateau

Because the rotation rates are not significantly different from zero (Figure 4.5c) across the Tibetan Plateau extending from the YZS to at least north of the Qaidam basin, and the principal contraction rate is about twice the magnitude as the principal extension rate, the strain tensor can be decomposed as follows:

$$\begin{pmatrix} \dot{\varepsilon}_1 & 0 \\ 0 & \dot{\varepsilon}_2 \end{pmatrix} = \dot{\varepsilon}_2 \begin{pmatrix} -1 & 0 \\ 0 & 1 \end{pmatrix} + \dot{\varepsilon}_2 \begin{pmatrix} -1 & 0 \\ 0 & 0 \end{pmatrix} \tag{4.5}$$

The strain across the Tibetan Plateau can be approximated as a combination of pure shear (the first term in equation (4.5)), uniaxial contraction (the last term in equation (4.5)), and block motion. Figure 4.6 shows the velocity components at each site contributed by these three components. The pure shear corresponds to right-lateral simple shear across a vertical plane striking N12.4°W±1.3° and left-lateral simple shear across a vertical plane striking N77.6°E±1.3°. The uniaxial contraction is in the orientation of N32.6°E±1.3°, the maximum contracton directon, comparable to the revised India-Eurasia convergence direction [*Gordon* et al., 1999; *Holt* et al., 2000].

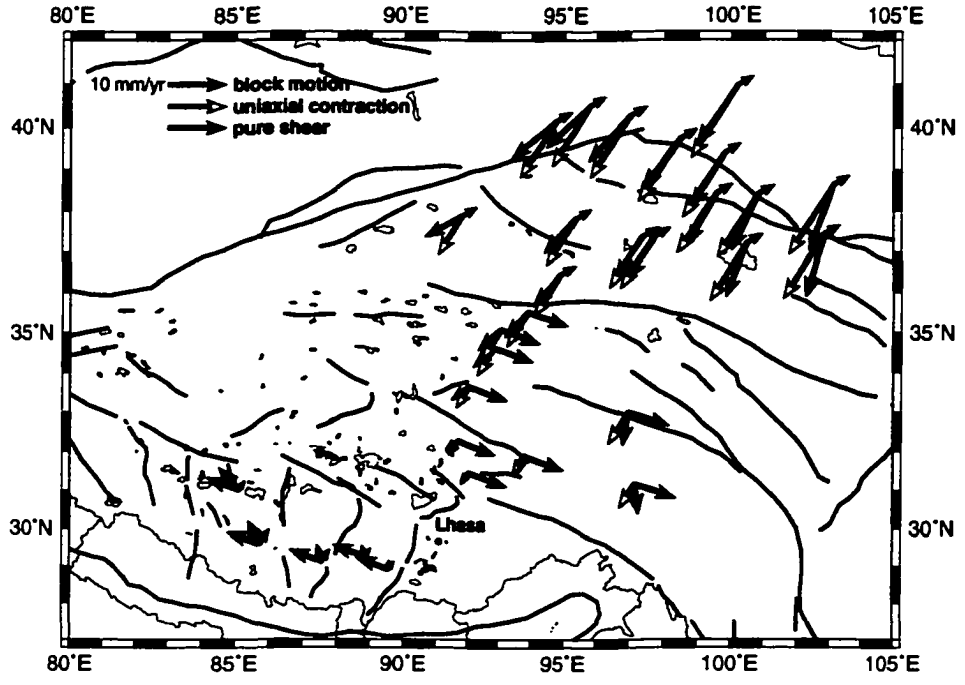

Figure 4.6. Modeled velocity field at selected sites relative to Lhasa (LHAS, shown as solid circle), shown for each of the three components of the best model. Solid arrows: block motions; Open arrows: uniaxial contraction; Grey arrows: pure shear.

The excellent fit of the single uniform strain rate tensor implies that deformation across the entire plateau can be described either as a continuum or as resulting from many distributed faults, each with a small slip rate. The prominence of strike-slip faulting across the Tibetan plateau, and the large velocity gradients we observe across the major strike-slip faults, leads us to suggest that deformation within the plateau is distributed rather than continuum. Distributed conjugate strike-slip faulting is a plausible mechanism for this distributed deformation, as noted by [*Molnar and Lyon-Caen*, 1989]. With an average GPS site spacing of ~80 km, we cannot identify individual faults, but if a single fault had a large slip rate (several mm/yr), we would expect to see a larger than average gradient over a distance from 50-100 km of the faults.

There are hints of deviation from uniform strain seen in Figure 4.3a. The slope of the line from NYMA at distance of 0 km to 400 km may be lower than the average, and the slope may be higher than average from km 400 to 600, but both a greater density of sites and more precise velocities would be needed to confirm the variation. The recent (November 2001) M_s 7.9 Kunlun fault earthquake [*van der Woerd* et al., 2002] makes it likely that any data aquired in the northern Tibetan Plateau over the next several years will be affected by postseismic deformation, so it may be many years before this question can be addressed again.

The strike N77.6°E±1.3° of the vertical plane of maximum left-lateral shear is similar to the orientation of the left-lateral Altyn Tagh fault (with a strike of ~N80°E), as we pointed out in the previous section. The Kunlun fault is oriented within 10-20° of this plane of maximum shear. Note that slip on these faults has been already incorporated in the model via the block motions. However, this shows that the broadly-distributed strain between the faults has a similar orientation to these major faults. The major faults may correspond to significant pre-existing zones of weakness that act to concentrate much of the shear in narrow zones. The left-lateral shear on these faults (the block motions), summed together with the uniaxial shortening component of the strain field, produces a velocity field that are approximately pure shear, meaning that the kinematics of the entire plateau is described as pure shear. Pure shear produces no areal dilatation. The dilatation rate ($\dot{\varepsilon}_1 + \dot{\varepsilon}_2$) in each region is about -0.01×10$^{-6}yr^{-1}$ (Table 4.2), so crustal thickening is presently minor within the Tibetan Plateau. See section 4.6.6 for more detail.

The vertical plane of maximum right-lateral shear strikes N12.4°W±1.3°. Although major left-lateral strike slip faults dominate the tectonics of eastern Tibet, *England and Molnar* [1990] argued that the left-lateral faulting in eastern Tibet is a manifestation of north striking, right-lateral, simple shear, resulting in the clockwise rotation of the crustal blocks forming the eastern part of the plateau. We suggest that *England and Molnar* [1990] recognized only a part of the overall deformation pattern, and not the entire pattern of pure shear.

4.6.2 Kunlun Fault

We investigated the slip rate of the Kunlun fault using three stations south of the fault (WT03, WUDA, and WT02) and five sites north of the fault (GOLM, GLMD, DACA, DHLA, and DELI). If we assume that all relative motion between these sites results from slip on the Kunlun fault, and that the fault is slipping below a depth of 15 km and locked to the surface, a 2-D screw dislocation model [*Savage and Burford*, 1973] will predict left lateral shear of 10.3±0.4 mm/yr with no significant contraction on the Kunlun fault (Figure 4.7). This estimate is consistent with the 11.5±2.0 mm/yr reported on the western Kunlun fault by *van der Woerd* et al. [2000].

However, the Tibetan Plateau undergoes broadly-distributed deformation that may absorb some of this relative motion. For example, our uniform strain plus block motion model suggests that about 2.4 mm/yr of the 5.8 mm/yr relative motion between GOLM and WUDA is accommodated by internal deformation, implying a slower slip rate of 4.4±1.1 mm/yr on the Kunlun fault, marginally comparable with 6±2 mm/yr reported by *Chen* et al. [2000] based on two GPS sites on the eastern Kunlun fault (east of our data). Figure 4.7 shows the comparison of our model and 2-D screw dislocation model with a 15 km locking depth.

Both models are satisfactory interpretations of the fault-parallel components of the data. The total residuals of the 2-D screw dislocation model and uniform strain plus block motion fitting the data are 6.7 and 5.5, respectively, not significantly different (the uniform strain model fits better). In the first model, we assume that there are no other faults close enough to the Kunlun fault, so all of the ~10 mm/yr of shear across the 400 km wide zone is attributed to the Kunlun fault. The "one-strain" model, on the other hand, assumes the

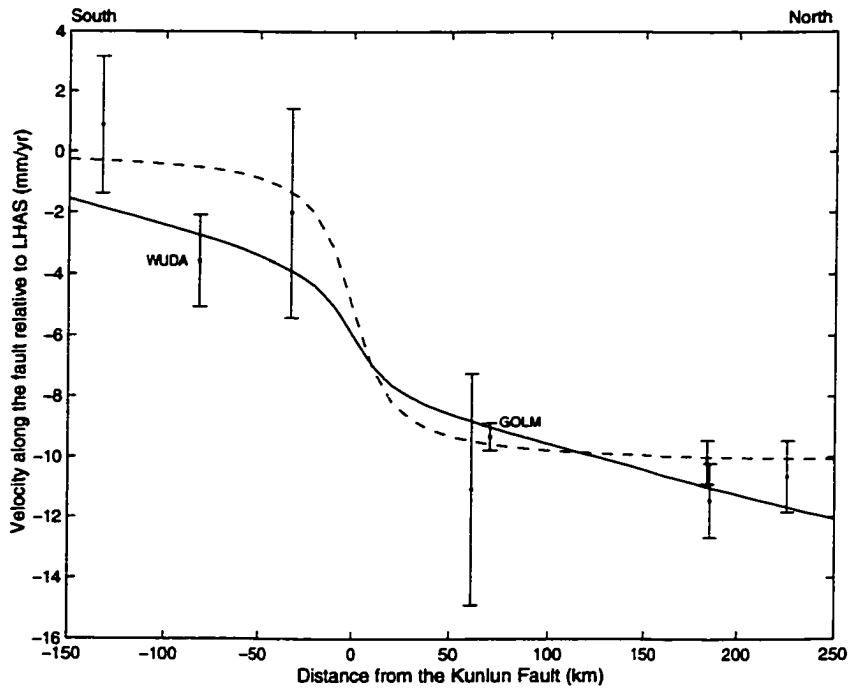

Figure 4.7. Predicted deformation from two different models, along with data from eight sites on either side of the Kunlun fault. Data are shown with error bars representing one standard deviation. Dashed line: preferred 2-D screw dislocation model with a 15 km locking depth; Solid line: our uniform strain plus block motion model, with uniform strain over the entire region, plus 4.4 mm/yr of slip rate on the Kunlun fault (15 km locking depth assumed).

material on each side of the fault is being deformed by slip on a broadly-distributed set of faults to approximate a continuum, and predicts that pure shear and uniaxial contraction accommodate about 30% and 20%, respectively, of the shear across this 400 km wide zone, while block motion accounts for roughly half of the shear seen across this region (Figure 4.6 and 4.7a). The model with only the Kunlun fault predicts the rate consistent with the geologic estimate, while the "one-strain" model is a slightly better fit to the GPS data. These two models are end-members that give upper and lower bounds, respectively, on the slip rate on the Kunlun fault. More data from near field of the Kunlun fault would help constrain the model.

Our deforming block model also suggests an opening rate of 4.0±0.9 mm/yr across the Kunlun fault. There is evidence for normal faulting in the eastern Kunlun range from SPOT images [*van der Woerd* et al., 2002], although our rate seems to be faster than what *van der Woerd* et al. [2002] inferred. This extension may result from the difference in strike between the Kunlun fault and the vertical plane across which left-lateral shear is greatest. A model with the Kunlun fault constrained to be purely strike slip also provides a satisfactory fit to the data, and gives a similiar left-lateral slip rate on the Kunlun fault to the "one-strain" model. However, an F-test shows that the "one-strain" model fits all the data significantly better than a model with pure strike-slip on the Kunlun fault at 95% confidence level. So we use our "one-strain" deforming block model here.

4.6.3 Opening of the Yadong-Gulu Rift

The Yadong-Gulu rift is the longest normal faulting system in Tibet, extending from Yadong close to the main Himalaya thrust north to the KJFZ [*Armijo* et al., 1986]. GPS data show that the Yadong rift is more active than other rift systems in southern Tibet, and concentrates up to one-half of the east-west extension in southern Tibet (Chapter 3). In our model, the rift is a block boundary that separates southern Tibet into blocks east and west of the rift. In the course of our modeling, we found that NYMA is a critical site, showing significant extension between NYMA and NAGQ. Both of these sites are located north of the KJFZ, which *Armijo* et al. [1986, 1989] suggested separates rapidly extending southern Tibet from undeforming northern Tibet, and which we chose as a block boundary. The "one-strain" deforming block model fails to explain the velocity of NYMA unless we allow

the opening of the Yadong rift to extend north of the KJFZ. Although we cannot contrain how far it must extend based on our present GPS data, we infer that the localized extension associated with the rift must extend north of NYMA. Data from new sites in north-central and northwestern Tibet will be required to resolve this question.

Our estimated opening rate for the Yadong-Gulu rift is 5.9±0.7 mm/yr in the N69°W direction, much higher than the 1.4±0.8 mm/yr estimated by *Armijo* et al. [1986]. We do not have a good explanation for this discrepancy, but note that the GPS data sample a wider zone than just the main rift, and thus there may be significant extension missed in the geologic studies. The GPS data also measure extension at depth, which might be more localized than surface extension.

4.6.4 Karakorum-Jiali Fault Zone

If we simply take the velocity difference between the sites TCOQ and NYMA, we would estimate ~7 mm/yr right-lateral strike slip on the KJFZ at 86°E. The block motions estimated in our "one-strain" model give the same result: 7.4±0.7 mm/yr of slip on the KJFZ. This is considerably less than 10-20 mm/yr proposed by *Armijo* et al. [1989]. The estimate of *Armijo* et al. [1989] was based on assumed dates for offset features, which led to their high uncertainty. The assumed dates probably explains the factor of two difference between *Armijo et al.*'s [1989] rate and the GPS rate.

The KJFZ is a series of *en échelon* right-lateral faults that *Armijo* et al. [1989] proposed acted as a major throughgoing shear zone. As described in the previous section, our results confirm that significant strike slip motion is localized there. However, the KJFZ does not represent the boundary between extensional southern Tibet and non-deforming northern Tibet, as *Armijo* et al. [1989] proposed. Instead, our data show that both southern and northern Tibet are extending in the N110°E direction.

Relative to Eurasia, the eastward components of the velocities of sites in central Tibet north of the KJFZ increase steadily northward from ~14 mm/yr just north of the KJFZ to ~23 mm/yr in eastern Tibet south of the Kunlun Shan, along with a decrease of the northward components [*Wang* et al., 2001]. This indicates that central and northern Tibet are being extruded eastward and this extrusive motion is rapid in eastern Tibet, amounting to ~50% of India-Eurasia convergence rate.

The observed strike slip on the KJFZ is not fast enough to cause all of the eastward extrusion in central Tibet if it is an undeformed block as suggested by *Armijo* et al. [1989]. Another tectonic source, internal deformation, must play the main role in driving the eastward extrusion.

4.6.5 Regional versus Localized Extension

In addition to large-scale strike slip faults in the Tibetan Plateau, the KJFZ in the south, and the Kunlun, Altyn Tagh faults in the north, the whole plateau is undergoing distributed deformation. Based on interpretation of a 1:1,000,000 scale mosaic of Landsat images, *Rothery and Drury* [1984] identified strike slip and normal faults distributed across the entire plateau. They proposed that these faults play a role in east-west extension and north-south shortening in the plateau to accommodate the northward motion of India, and estimated that shortening within the plateau could account for about one-third of the total India-Eurasia convergence over the last 3 Ma.

Earthquake fault plane solutions suggest that conjugate strike-slip and normal faulting prevails in north-central Tibet [*Molnar and Lyon-Caen*, 1989]. *Molnar and Lyon-Caen* [1989] inferred the rate of crustal shortening within Tibet to be 5 mm/yr, and the east-west extension rate across all of north-central Tibet to be roughly 10 mm/yr, with very large uncertainties. The GPS data show that the rate of internal deformation of the plateau is about twice as high as that estimated by *Molnar and Lyon-Caen* [1989]. Our estimated contraction rate within the Tibetan Plateau is about one-third of the total India-Eurasia convergence rate, which agrees with that proposed by *Rothery and Drury* [1984]. The implications of this style of distributed extension and conjugate strike-slip faulting will be discussed in the next section.

Direct field evidence for significant late Neogene east-west extension in north-central Tibet has been provided by *Blisniuk* et al. [1998] and *Yin* et al. [1999]. *Yin* et al. [1999] estimated the magnitude of slip across major normal faults in northern Tibet to be on the order of 1-4 mm/yr, comparable to that for similar faults in southern Tibet [*Armijo* et al., 1986], and suggested that the entire plateau has been extending and that east-west extension is distributed throughout the plateau.

Distributed regional extension is an important contribution to the eastward extrusion of

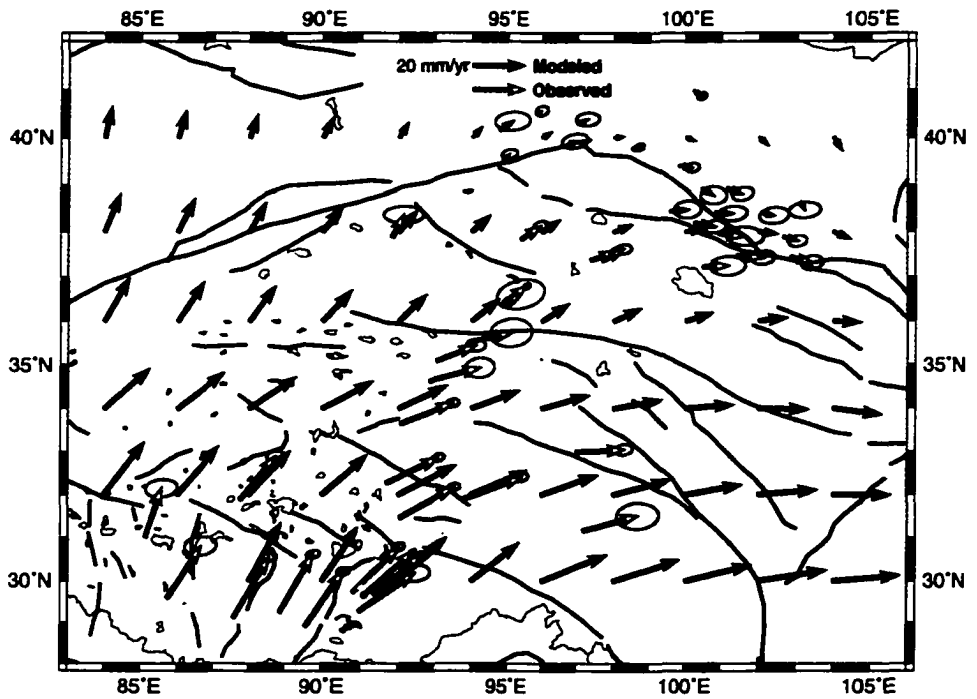

Figure 4.8. Velocity field (relative to the Eurasian frame) in the Tibetan Plateau predicted by our preferred uniform strain rate plus block motion model. Solid arrows: predicted velocity; Open arrows: observed velocities at sites used in this study. Uncertainties are 95% confidence ellipses.

eastern Tibet. In this study, we estimate a right-lateral slip rate of 7.4± 0.7 mm/yr on the KJFZ, and a left-lateral slip rate of between 4.4±1.1 and 10.3±0.4 mm/yr on the Kunlun fault. These strike slip rates, along with a slow slip rate of ~10 mm/yr on the Altyn Tagh fault [*Bendick* et al., 2000; *Shen* et al., 2001b; *Chen* et al., 2000] can explain only ~30% of the fast eastward component of displacement of ~25 mm/yr that we observe in central Tibet (with respect to Eurasia, Figure 4.8). The magnitude of the extension resulting from slip on conjugate strike-slip faults within Tibet could be up to 18 mm/yr between longitudes of 85°E and 95°E, based on our "one-strain" model. Thus, eastward extrusion of eastern Tibet results more from internal deformation of the plateau than from block-like extrusion.

Not only is the east-west extension in the plateau broadly distributed, but also the north-south shortening. The linear trend of the north-south shortening across the plateau (Figure 4.3b) suggests that the deformation must be broadly distributed over the entire plateau, as noted by *Wang* et al. [2001]. There would be a significant deviation from the linear trend if any single fault took up a considerable fraction of the shortening. Thus any models based on the assumption that all deformation is localized along a few major faults will be biased. For example, *Peltzer and Saucier*'s [1996] model does not predict the roughly east-west extension in southern and central Tibet that we observe. The spatially uniform deformation across the Tibetan Plateau proposed here is consistent with the strain expected for deformation of a continuum, although we cannot distinguish between continuum deformation and deformation broadly distributed over many active faults.

4.6.6 Lateral Extrusion versus Crustal Thickening

Our model of uniform strain rate plus block motions suggest that crustal thickening is minor at present. The dilatation rate ($\dot{\varepsilon}_1 + \dot{\varepsilon}_2$) in each region is about -0.01$\times 10^{-6} yr^{-1}$ (Table 4.2); presently the surface area in the plateau is reducing at a rate of 1% per million years from the collision between India and Eurasia. Pure shear, which is dominant across the entire plateau, does not cause any reduction in surface area. This style of strain probably resulting from conjugate strike-slip faulting, accommodates much of the shortening and extrusion. We propose that north-south shortening presently occurs within Tibet by slip on distributed conjugate strike-slip faults, and not by crustal thickening. Conjugate strike-slip faulting accommodates shortening without thickening. Thus we infer that once the Tibetan Plateau was formed, the resulting buoyancy force associated with the thick crust inhibits further thickening [*England and Houseman*, 1986] and eastward extrusion resulting from strike-slip faulting and internal deformation presently dominate in accommodating the collision between the India and Eurasia.

There has been a long debate over whether the crustal thickening or eastward block-like extrusion has been more significant in accomodating the collision of India. The answer for the present is that neither of these mechanism are dominant.

Lateral Extrusion

Based on field observations, *Armijo* et al. [1986, 1989] proposed an extrusion model, assuming that the plateau between the KJFZ and Altyn Tagh faults acts as a rigid or slowly-deforming block. They estimated a slip rate of 20±10 mm/yr along the KJFZ and 31±15 mm/yr along the Altyn Tagh, and suggested that the average rate of convergence absorbed by such block-like extrusion would be on the order of 20 mm/yr, "at least 30% of the present convergence between India and Asia" [*Armijo* et al., 1989]. Although we agree that a kind of eastward extrusion is significant in the convergence between India and Eurasia, the assumptions on which the *Armijo* extrusion model are based conflict with our observations.

First, geodetically observed fault slip rates on the KJFZ and Altyn Tagh are much lower than those they estimated. We observe a right-lateral slip rate of 7.4±0.7 mm/yr on the KJFZ. *Bendick* et al. [2000] measured a 9±5 mm/yr slip rate across the central part of the Altyn Tagh fault using GPS data along the profile approximated 89-91°E. Using more distributed GPS data along the fault, *Shen* et al. [2001b] reported a similar estimate of 9±2 mm/yr. *Chen* et al. [2000] determined rates of 9±2 mm/yr and 6±2 mm/yr on the two lines straddling the fault near longitude 92°E and 93°E, respectively. These geodetic estimates of slip rates along the Altyn Tagh fault are comparable with ~6 mm/yr estimated by *Project Altyn Tagh members* [1992] based on geological field observations, but are considerably less than the 20-30 mm/yr proposed by *Peltzer* et al. [1989] and *Ryerson* et al. [1997] based on geomorphological inferences. The cause of this disagreement is not yet clear. Such low slip rates can produce less than 10 mm/yr of eastward extrusion relative to Eurasia, only about one third of that observed. We have proposed that internal deformation of the plateau produces the dominant component of the extrusion.

Secondly, Tibet between the KJFZ and Altyn Tagh fault is strongly deformed as proposed by *Rothery and Drury* [1984], and not an undeformed block as assumed by *Armijo* et al. [1989]. In constructing a kinematic model, neglecting the internal deformation in the plateau would result in an underestimate of the eastward motion. If, however, the eastward displacement rate of eastern Tibet is used in such a model, the assumption of an undeformed block between the KJFZ and Altyn Tagh faults would lead to overestimates of slip rates on these faults.

Crustal Thickening

In contrast, numerical experiments, such as thin viscous sheet models treat deformation on a lithospheric scale as continuum and suggest that most of the convergence (may be up to 75%) between India and Eurasia has been absorbed by crusal shortening and thickening to produce the high plateau [*England and Houseman*, 1986; *Houseman and England*, 1993]. However, this kind of model predicts no strike-slip deformation and limited eastward displacements, both of which clearly conflict with our observations. This limitation could result partly from the rather artifical eastern boundary, described as a lithostatic boundary in the models [*Houseman and England*, 1993] or from the inability of such models to account for localized slip on major strike-slip faults. Their numerical experiments showed that the eastward displacement rate at the eastern boundary could not exceed 25% of the indentation rate in the thin viscous sheet model [*Houseman and England*, 1993]. However, our GPS data show that eastern Tibet is moving eastward at a rate of 20-25 mm/yr relative to Eurasia, about 50% of the convergence between India and Eurasia. There is no evidence that some of the rate could plausibly be related to the subduction of the western Pacific, as presumed by *Houseman and England* [1993], because the results of *Wang* et al. [2001] show that material rotates around the eastern syntaxis rather than extrudes eastward over the subduction zones. Thus, while thin viscous sheet models may be applicable to some of the history of the India-Eurasia collision, they do not describe the present tectonics of the Tibetan Plateau.

Unlike the thin viscous sheet model, *Shen* et al. [2001a] proposed a model with a Newtonian-viscous crust with no heterogeneities or anisotropies in any horizontal plane. This model suggests that the Tibetan Plateau is likely to have gone through a two-stage development: the convergence between India and Eurasia would have produced the present-day elevation of Tibet; subsequestly the plateau has grown to the north and east without significant increase in height. This developmental sequence differs from the results of the thin viscous sheet model [*England and Houseman*, 1986], where the region of crustal thickening is always distributed, and suggests that east-west stretching and eastward plateau growth dominate the present tectonics of the Tibetan Plateau, as we observe.

England and Molnar [1997] performed a Kostrov summation of strain rates inferred from Quaternary fault slip rates and fit them with a continuous velocity field within Asia.

They obtained little eastward motion of central Tibet, and inferred that most of India's convergence with Eurasia is absorbed by crustal thickening. The result of this approach, however, conflicts with the GPS observation of fast eastward motion in eastern Tibet. The problem with their approach results from the input Quaternary fault slip rates, which are incomplete and still debatable for some of the major faults in Asia. *England and Molnar* [1997] missed the rapid east-west extension within Tibet, and the rapid extrusion/rotation of material around the syntaxis because they lacked fault slip rates from those places.

4.6.7 Predicted Velocity Field

Based on the 44 GPS sites in and near the Tibetan Plateau, most concentrated between 90°E and 95°E, we derived a model of uniform strain rate plus block motion to interpret the data. Assuming the kinematics of the entire plateau can be well described by our model, we extrapolate from our small area and predict the velocity field of the entire Tibetan Plateau relative to stable Eurasia frame shown in Figure 4.9.

Our velocity field shows the general features that we have discussed in the previous sections. Tibet is strongly deformed, with distributed east-west extension throughout the entire plateau, which results in fast eastward extrusion rate at eastern Tibet. Western Tibet is extruding at a slower rate, and the rate of eastward motion increases from west to east. Figure 4.9 also shows where the observations deviate from the extrapolated uniform strain model. The Tarim vectors are systematically offset by a westward vector, which corresponds to the Altyn Tagh slip rate [*Bendick* et al., 2000; *Chen* et al., 2000; *Shen* et al., 2001b]. The Altyn Tagh fault is not included in our model, so this is not surprised. Finally, although most data from eastern Tibet are well-predicted, the one site near the syntaxis actually moves south rather than north relative to Eurasia. Our model does not predict the rapid rotation around the syntaxis. Taken together, these misfits show that the pattern of strain near the syntaxis is quite different from the rest of the plateau.

Holt et al. [2000] performed a joint inversion of Quaternary strain rates and GPS velocities in Asia for a self-consistent velocity field, including more minor Quaternary faults than used by *England and Molnar* [1997]. Their model has a general similarity to our observations, but some significant differences. Their model velocity field shows that east-west extension is distributed throughout both southern and north central Tibet, with a

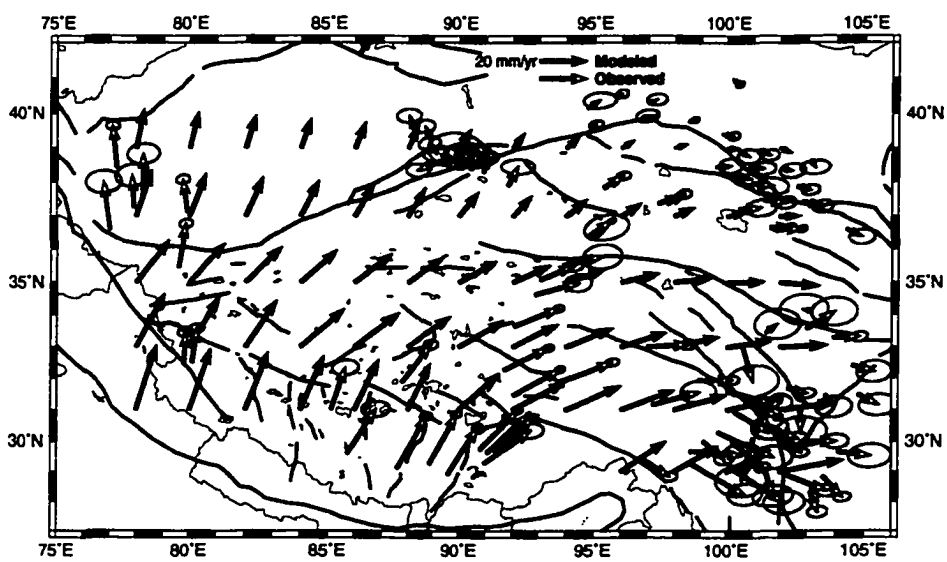

Figure 4.9. Velocity field in the Tibetan Plateau and its vicinity (relative to the Eurasian frame) predicted by our preferred uniform strain rate plus block motion model. Solid arrows: predicted velocity; Open arrows: observed velocities at selected sites used. These include sites not used to develop our model. Uncertainties are 95% confidence ellipses.

magnitude of 16-19 mm/yr between the longitude of 77°E to 92°E, comparable with that expected by our model. Furthermore, their solution suggests eastern Tibet is moving eastward at a high rate, as we observe. However, we show that a shear zone concentrates on the KJFZ, whereas *Holt et al.*'s [2000] model shows a more distributed deformation across Tibet and no equivalent throughgoing right-lateral shear zone is present across the KJFZ. These differences result from a lack of data available to *Holt* et al. [2000] in some critical places.

Our synthetic velocity field could not fit the GPS velocity in Shiquanhe, westernmost of the southern Tibet, where the velocity can be explained by pure shortening in the Indian-Eurasian plate motion direction. This suggests our model may underpredict the total amount of ~110° extension across southern Tibet. This misfit may result from the simplicity of our block boundaries, which are not well defined in western Tibet where there is little GPS data. More GPS data from west-central Tibet, which we have proposed to collect, will help improve the model.

In the Tarim basin, north of the Altyn Tagh fault, our uniform model doesn't completely interpret GPS observations (Figure 4.9). The reason for the large misfit is that our model doesn't include the Altyn Tagh fault as a block boundary. However, the misfit between the observations and prediction from our model can be interpreted as a rotation with a pole of 46.4°E and 12.6°N, and an angular velocity of $0.198°\text{Myr}^{-1}$. Tarim basin has been suggested to rotate clockwise relative to Eurasia as a rigid block [*Peltzer and Saucier*, 1996; *Holt* et al., 2000; *Shen* et al., 2001b]. So we suggest that rotation of the rigid Tarim basin is driven by the upper mantle in which pure shear is dominant.

4.7 Conclusion

The deformation caused by the collision between India and Eurasia is distributed across the Tibetan Plateau and partly localized on a few major faults in the plateau. The GPS velocities are well described by a combination of block motions, pure shear, and uniaxial contraction. The axes of maximum contraction and extension of the pure shear oriented in the direction of N32.6°E±1.3° and N57.4°W±1.3°, respectively, parallel and normal to the strike of the Altyn Tagh fault. The uniaxial contraction oriented in the direction of N32°E,

comparable to the convergence direction between the India and Eurasia. Thus the driving force for these shears is attributed to the relative motion between the Indian and Eurasian plates. The sum of the three components (block motions, uniaxial contraction, and pure shear) is essentially pure shear, therefore, the present-day kinematics of the Tibetan Plateau is dominant by pure shear.

Our results suggest that 5.9±0.7 mm/yr opening in the N69°W direction occurs in the Yadong-Gulu rift, and this opening may extend as far north as the Nyainqentanglha range. We place lower and upper bounds, 4.4±1.1 and 10.3±0.4 mm/yr, respectively, of left-lateral shear on the Kunlun fault, and estimate a right-lateral slip rate of 7.4±0.7 mm/yr on the KJFZ, significantly slower than geologic estimates.

GPS observations and our uniform strain plus block motions suggest eastward extrusion rather than crustal thickening is dominant present tectonics of the Tibetan Plateau. Eastward motion of eastern Tibet is about 25 mm/yr between the KJFZ and Kunlun fault, absorbing about 50% of the convergence between the India and Eurasia. The observed low strike-slip rates on the KJFZ and Altyn Tagh [*Bendick* et al., 2000; *Chen* et al., 2000; *Shen* et al., 2001b] can produce only ~30% of the eastward displacements of eastern Tibet. The strong deformation within the Tibetan Plateau accomodates up to 70% of the eastward extrusion. Conjugate strike-slip faulting plays a main role in accommodating the observed contraction and extension.

Chapter 5

Conclusions

GPS data presented within this thesis were used to investigate crustal deformation along and within two plate boundaries: the San Andreas Fault and the Tibetan Plateau. Several new contributions were made in this thesis, including: an understanding of the importance of lateral variations of elastic moduli in strain accumulation along the San Andreas Fault (Chapter 2); insight into the east-west extension in southern Tibet and its mechanism (Chapter 3); and a new kinematic description of the Tibetan Plateau and its tectonic implication (Chapter 4).

5.1 San Andreas Fault

GPS measurements in 1996 and 1997 at sites in five small-aperture geodetic networks along the San Andreas fault in San Francisco Bay area were used to improve site coordinates needed to process the raw EDM data. Line lengths computed from the GPS solutions and EDM data were combined to determine the near-fault strain rate.

Pronounced shear strain rates of 0.366 ± 0.095 and 0.316 ± 0.060 μstrain/yr were observed in the Lake San Andreas and Black Mountain-Radio Facility networks, respectively, which are located on the San Francisco Peninsula segment. A similar strain rate was reported at Point Reyes [*Prescott* et al., 1981; *Lisowski* et al., 1991]. This high observed near-fault shear strain can be explained by a 2-D uniform half-space model with shallow locking depth ($\sim$7-8 km). Although this cannot be ruled out, such a shallow locking depth is unlikely

based on the seismological evidence and GPS measurements made farther from the faults [*Lisowski* et al., 1990; *Marshall* et al., 1991].

We proposed a 2-D inhomogeneous model in which a low rigidity compliant zone surrounds the fault, as there is substantial evidence for near-fault compliant zone on several segment of the SAF. The change in rigidity required to explain the high near-fault strain rate is consistent with the change in seismic wave velocity and resistivity observed in the fault zone at Loma Prieta and Parkfield, farther to the south along the San Andreas fault.

However, at Tomales Bay, Bodega Bay, and Point Arena [*Freymueller* et al., 1999], farther to the north, there is no evidence for a low rigidity zone surrounding the fault, suggesting that both the age of the fault and materials on each side of the fault may play roles in the development of the low rigidity zone.

Future work should apply this method in other strike-slip faults with large-enough offset, such as the North Anatolian fault in Turkey, the Xianshuihe fault in eastern Tibet and the Altyn Tagh fault in northern Tibet, to test whether the compliant zone is peculiar to the San Andreas Fault or a general feature of all strike-slip faults.

5.2 Tibetan Plateau

GPS measurements have proven to be a good tool for plate tectonics studies, especially for broad plate boundary zones. The GPS sites in Nepal and the Tibetan plateau help us to determine how the Indian-Eurasian plate boundary deformation is distributed and which tectonic components are important in accommodating the relative motion of the plates.

We have observed 13±1 mm/yr of extension, roughly in the N110°E direction, in southern Tibet between the longitudes of 80°E and 91°E, resulting from the arc-normal convergence between India and Eurasia along the Himalayan arc. The rate of extension is not uniform across all of southern Tibet. The Yadong-Gulu rift with an opening rate of 6.5±1.5 mm/yr and the Yarlung-Zangbo suture with 3±1 mm/yr of right-lateral shear concentrate most of the extension. Including sites farther east to 93°E, the total rate of extension across southern Tibet is at 26±3 mm/yr.

Spatially non-uniform extension in southern Tibet results in variations in the arc-normal convergence rate along the Himalaya. We observe that the convergence rate varies along

the Himalaya, with 17±1, 12.1±0.8, and 19±1 mm/yr in the western, central, and eastern sgements of the Himalaya.

Not only does extension occur in southern Tibet, it is found throughout the entire plateau. Significant distributed internal deformation exists across the plateau. The distributed deformation is well expressed by pure shear on the two vertical planes roughly parallel and normal to the strike of the Altyn Tagh fault, with a maximum contraction oriented N32°E, comparable to the convergence direction between the India and Eurasia. Thus the driving force for these shears is attributed to the relative motion between the Indian and Eurasian plates.

GPS observations and our numerical model suggest eastward extrusion rather than crustal thickening is dominant the present tectonics of the Tibetan Plateau. Eastward motion of eastern Tibet between the KJFZ and Kunlun fault accommodates up to 50% of the convergence between the India and Eurasia. However, the observed low strike-slip rates on the KJFZ and Altyn Tagh [*Bendick and Bilham*, 2001; *Chen* et al., 2000; *Shen* et al., 2001b] can produce only ~30% of the eastward displacements of eastern Tibet. Instead, we infer that the internal extension of the plateau results in much of this eastward motion. Conjugate strike-slip faulting plays a main role in accommodating the observed contraction and extension.

This work has raised many new questions: Does the convergence rate between India and Tibet vary along the Himalaya? If so, is this variation consistent with that of the relative motion between India and Eurasia along the Himalaya, that is the motion of the Indian plate with respect to the Eurasian plate increases from western Himalaya to eastern Himalaya, predicted by both NUVEL-1A [*DeMets* et al., 1990, 1994] and REVEL [*Sella* et al., 2002] models? Is the east-west extension in northern Tibet spatially non-uniform as we see in southern Tibet where the Yadong-Gulu rift concentrates most of the extension? What drives extension in northern Tibet? Conjugate strike-slip faulting is a plausible mechanism for the extension in northern Tibet.

Because most of the Nepal sites were surveyed in 1991 and 1995, newer GPS measurements in Nepal are needed to improve the precision. Other data from sites in both sides of western and eastern Himalaya will help accurately determine the convergence rates between India and Eurasia. Data from more sites especially in western-central Tibet will improve

our knowledge of spatial distribution of crustal deformation in the Tibetan plateau, as well as the extension in northern Tibet.

Bibliography

Alsdorf, D. L., L. Brown, K. D. Nelson, Y. M. S. Klemperer, and W. Zhao, Crustal deformation of the Lhasa terrane, Tibet plateau from Project INDEPTH deep seismic reflection profiles, *Tectonics*, *17*, 501–519, 1998.

Armijo, R., P. Tapponnier, J. L. Mercier, and T. L. Han, Quaternary extension in Southern Tibet: Field observations and tectonic implications, *J. Geophys. Res.*, *91*, 13,803–13,872, 1986.

Armijo, R., P. Tapponnier, and T. L. Han, Late Cenozoic right-lateral strike-slip faulting in southern Tibet, *J. Geophys. Res.*, *94*, 2787–2838, 1989.

Árnadóttir, T. and P. Segall, The 1989 Loma Prieta earthquake imaged from inversion of geodetic data, *J. Geophys. Res.*, *99*, 21,835–21,855, 1994.

Árnadóttir, T., P. Segall, and P. T. Delaney, A fault model for the 1989 Kilauea south flank earthquake from leveling and seismic data, *Geophys. Res. Lett.*, *18*, 2217–2220, 1991.

Avouac, J. P. and P. Tapponnier, Kinematic model of active deformation in Asia, *Geophys. Res. Lett.*, *20*, 895–898, 1993.

Baranowski, J., J. Armbruster, L. Seeber, and P. Molnar, Focal depths and fault plane solutions of earthquakes and active tectonics of the Himalaya, *J. Geophys. Res.*, *89*, 6918–6928, 1984.

Barazangi, M. and J. Ni, Velocities and propagation characteristics of Pn and Sn beneath the Himalayan arc and Tibetan Plateau: Possible evidence for understanding of Indian continental lithosphere beneath Tibet, *Geology*, *10*, 1982, 1982.

Bendick, R. and R. Bilham, How perfect is the Himalayan arc?, *Geology*, *29*, 791–794, 2001.

Bendick, R., R. Bilham, J. T. Freymueller, K. Larson, and G. Yin, Geodetic evidence for a low slip rate in the Altyn Tagh fault system, *Nature*, *404*, 69–72, 2000.

Bennett, R. A., J. L. Davis, B. P. Wernicke, and J. E. Normandeau, Space geodetic measurements of plate boundary deformation in the western U.S. Cordillera, in S. Stein and J. T. Freymueller (eds.), *Plate Boundary Zones*, AGU Memograph, Washington, DC. in press, 2002.

Berg, B., Locating glocal minima in optimization problems by a random-cost approach, *Nature*, *361*, 708–710, 1993.

Beroza, G. C., Near-source modeling of the Loma Prieta earthquake: evidence for heterogeneous slip and implications for earthquake harzard, *Bull. Seism. Soc. Am.*, *81*, 1603–1621, 1991.

Bilham, R., K. Larson, J. Freymueller, and P. I. Members, GPS measurements of present day convergence rates in the Nepal Himalaya, *Nature*, *336*, 1997, 1997.

Bilham, R., F. Blume, R. Bendick, and V. K. Gaur, Geodetic constraints on the translation and deformation of India: Implications for future great Himalayan earthquakes, *Curr. Sci.*, *74*, 213–229, 1998.

Blisniuk, P. M., S. Siwen, O. Kuchel, and L. Ratschbacher, Late Neogene extension in the Shuang Hu graben, central Tibet, *EOS Trans. AGU*, *79*, 794, 1998.

Boucher, C., Z. Altamimi, and P. Sillard, The 1997 International Terrestrial Reference Frame (ITRF97), in *IERS Technical Note 27.*, Observatoire de Paris, France. 1999.

Brace, W. F., Laboratory studies of stick-slip and their application to earthquakes, *Tectonophysics*, *14*, 189–200, 1972.

Brown, E. T., R. Bendick, D. L. Bourlès, V. Gaur, P. Molnar, G. M. Raisbeck, and F. Yiou, Slip rate of the Karakorum fault, Ladakn, India, determined using cosmic ray exposure dating of debris flows and moraines, *J. Geophys. Res.*, in press, 2002.

Burchfiel, B. C., Q. Deng, P. Molnar, L. H. Royden, Y. Wang, P. Zhang, and W. Wang, Intracrustal detachment with zones of continental deformation, *Geology*, *17*, 752–784, 1989.

Burchfiel, B. C., Z. Chen, L. H. Royden, Y. Liu, and C. Deng, Extensional development of Gabo valley, southern Tibet, *Tectonophysics*, *194*, 187–193, 1991.

Burg, J. P., , and G. M. Chen, Tectonics and structural zonation of southern Tibet, China, *Nature*, *311*, 219–223, 1984.

Bürgmann, R., P. Segall, M. Lisowki, and J. Svarc, Postseismic strain following the 1989 Loma Prieta earthquake from GPS and leveling measurements, *J. Geophys. Res.*, *102*, 4933–4955, 1997.

Bürgmann, R., D. Schmidt, R. M. Nadeau, M. d'Alessio, E. Fielding, D. Manaker, T. V. McEvilly, and M. H. Murray, Earthquake potential along the northern Hayward Fault, California, *Science*, *289*, 1178–1182, 2000.

Byerlee, J., Model for episodic flow of high-pressure water in fault zones before earthquakes, *Geology*, *21*, 303–306, 1993.

Byerlee, J., V. Mjachkin, R. Summers, and O. Voevoda, Structures developed in fault gouge during stable sliding and stick-slip, *Tectonophysics*, *44*, 161–171, 1978.

Cervelli, P., M. Murray, P. Segall, Y. Aoki., and T. Kato, Estimating source parameters from deformation data, with an application to the March 1997 earthquake swarm off the Izu Peninsula, Japan, *J. Geophys. Res.*, *106*, 11,217–11,237, 2001.

Chen, Z., B. C. Burchfiel, Y. Liu, R. W. King, L. H. Royden, W. Tang, E. Wang, J. Zhao, and X. Zhang, Global positioning system measurements from eastern Tibet and their implications for India/Eurasia intercontinental deformation, *J. Geophys. Res.*, *105*, 16,215–16,227, 2000.

Cline, M. W., R. A. Snay, , and E. L. Timmerman, Geodetically derived strain from San Francisco Bay to the Mendocino triple junction, California, in *NOAA Tech. Rep. NGS*

311, volume NGS 311, p. 17pp, Nat. Oceanic and Atmos. Admin., Silver Spring, MD. 1985.

Cogan, M., K. Nelson, W. Kidd, C. Wu, and P. I. Team, Shallow structure of the Yadong-Gulu rift, southern Tibet, from refraction analysis of Project INDEPTH common mid-point data, *Tectonics*, *17*, 46–61, 1998.

DeMets, C., R. Gordon, D. F. Argus, and S. Stein, Current plate motions, *Geophys. J. Int.*, *101*, 425–478, 1990.

DeMets, C., R. Gordon, D. Argus, and S. Stein, Effect of recent revisions to the geomagnetic reversal time scale on estimates of current plate motions, *J. Geophys. Res.*, *21*, 2191–2194, 1994.

Du, Y., P. Segall, and H. Gao, Dislocations in inhomogeneous media via a moduli perturbation approach: General formulation and two-dimensional solutions, *J. Geophys. Res.*, *99*, 13,767–13,779, 1994.

Eberhart-Phillips, D. and A. J. Michael, Seismotectonics of the Loma Prieta, California, region determined from three-dimensional V_p, V_p/V_s, and seismicity, *J. Geophys. Res.*, *103*, 21,099–21,120, 1998.

Eberhart-Phillips, D., V. F. Labson, W. D. Staley, A. J. Michael, and B. D. Rodriguez, Preliminary velocity and resistivity of the Loma Prieta earthquake region, *Geophys. Res. Lett.*, *17*, 1235–1238, 1990.

England, P. C. and G. A. Houseman, Finite strain calculations of continental deformation; 2. Comparison with the India - Asia collision zone, *J. Geophys. Res.*, *91*, 3664 – 3676, 1986.

England, P. C. and P. Molnar, Right-lateral shear and rotation as the explanation for strike-slip faulting in eastern Tibet, *Nature*, *344*, 140–142, 1990.

England, P. C. and P. Molnar, The field of crustal velocity in Asia calculated from Quaternary rates of slip on faults, *Geophys. J. Int.*, *130*, 551–582, 1997.

Francheteau, J., C. Jaupart, J. S. Xian, K. Wen-Hua, L. De-Lu, B. Jia-Cha, W. Hung-Pin, and D. Hsia-Yeu, High heat flow in southern Tibet, *Nature*, *307*, 32–36, 1984.

Freymueller, J. T., R. Bilham, R. Bürgmann, J. Paul, S. Jade, and V. Gaur, lobal Positioning measurements of Indian Plate Motion and Convergence across the Lesser Himalaya, *Geophys. Res. Lett.*, *23*, 3107–3110, 1996.

Freymueller, J. T., M. H. Murray, P. Segall, and D. Castillo, Kinematics of the Pacific-North America plate boundary zone, northern California, *J. Geophys. Res.*, *104*, 7419–7441, 1999.

Freymueller, J. T., S. C. Cohen, and F. H. J, Spatial variations in present-day deformation, Kenai Peninsula, Alaska, and their implications, *J. Geophys. Res.*, *105*, 8079–8107, 2000.

Gill, P. E., W. Murray, and M. H. Wright, *Practical optimization.* Academic Press, London, 1981.

Gordon, R. G., D. F. Argus, and M. B. Heflin, Revised estimate of the angular velocity of India relative to Eurasia (abstract), *EOS Trans. AGU, Fall Meet. Suppl.*, *80*, F273, 1999.

Gregorius, T., *GIPSY-OASIS II: A User's Guide.* self-published, Univ. of Newcastle, Newcastle, England, U.K., 1996.

Hall, N. T., R. H. Wright, and K. B. Clahan, Paleoseismic studies of the San Francisco penninsula segment of the San Andreas fault zone near Woodside, California, *J. Geophys. Res.*, *104*, 23,215–23,236, 1999.

Harrison, M. T., P. Copeland, W. Kidd, and A. Yin, Raising Tibet, *Science*, *255*, 1663–1670, 1992.

Harrison, M. T., P. Copeland, W. Kidd, and O. M. Lovera, Activation of the Nyainqentanglha Shear Zone: Implications for uplift of the southern Tibet plateau, *Tectonics*, *14*, 658–676, 1995.

Holt, W. E., M. Li, and A. J. Haines, Earthquake strain rates and instantaneous relative motion within central and east Asia, *Geophys. J. Int.*, *122*, 569–593, 1995.

Holt, W. E., N. Chamot-Rooke, X. L. Pichon, A. H. B. Shen-Tu, and J. Ren, Velocity field in Asia inferred from Quaternary fault slip rate and Global Positioning System observations, *J. Geophys. Res.*, *105*, 19,185–19,209, 2000.

Houseman, G. A. and P. England, Crustal thickening versus lateral expulsion in India-Asia continental collision, *J. Geophys. Res.*, *98*, 12,233–12,249, 1993.

Irwin, W. P., Geology and plate-tectonic development, in R. E. Wallace (ed.), *The San Andreas fault system, California*, pp. 61–80, USGS professional paper 1515. 1990.

Jaeger, J. C., *Elasticity, Fracture and Flow.* Methuen, New York, 1964.

Johnson, H. O. and F. K. Wyatt, Geodetic network design for fault mechanics studies, *manusc. geod.*, *19*, 309–323, 1994.

Khattri, K., Great earthquakes, seismicity gaps, and potential earthquake disaster along the Himalaya plate boundary, *Tectonophysics*, *138*, 79–92, 1987.

Kidd, W., M. Edwards, Y. Yue, C. Wu, and K. Nelson, The END (East Nieru Detachment): A new low-angle mylonitic shear zone bording the Yadong-Gulu rift system, southern Tibet, *Geol. Soc. Am. Abst. Programs*, *27*, A–337, 1995.

Larson, K. M., J. T. Freymueller, and S. Philipsen, Global plate velocities from the Global Positioning System, *J. Geophys. Res.*, *102*, 9961–9981, 1997.

Larson, K. M., R. Bürgmann, R. Bilham, and J. T. Freymueller, Kinematics of the India-Eurasia collision zone from GPS measurements, *J. Geophys. Res.*, *104*, 1077–1093, 1999.

Lees, J. M. and P. E. Malin, Tomographic images of P-wave velocity variation, California, *J. Geophys. Res.*, *95*, 21,793–21,804, 1990.

Li, V. C. and J. R. Rice, Crustal deformation in great California earthquake cycles, *J. Geophys. Res.*, *92*, 11,533–11,551, 1987.

Li, Y. G., P. C. Leary, K. Aki, and P. E. Malin, Seismic trapped modes in the Oroville and San Andreas fault zones, *Science*, *249*, 763–766, 1990.

Lienkaemper, J., G. Borchardt, and M. Lisowski, Historic creep rate and potential for seismic slip along the Hayward fault, California, *J. Geophys. Res.*, *96*, 18,261–18,283, 1991.

Lisowski, M. and W. H. Prescott, Short-range distance measurements along the San Andreas fault system in central California, 1975 to 1979, *Bull. Seism. Soc. Am.*, *71*, 1607–1624, 1981.

Lisowski, M., W. H. Prescott, J. C. Savage, and M. J. S. Johnston, Geodetic estimate of slip during the 1989 Loma Prieta, California, earthquake, *Geophys. Res. Lett.*, *17*, 1437–1440, 1990.

Lisowski, M., J. C. Savage, and W. H. Prescott, The velocity field along the San Andreas fault in central and southern California, *J. Geophys. Res.*, *96*, 8369–8389, 1991.

Liu, Q., Paléoclimat et contraintes chronologiques sur les mouvements récent dans l'Ouest du Tibet: Failles du Karakorum et de Longmu Co-Gozha Co, lacs en pull-apart de Longmu Co et de Sumxi Co, *PhD thesis*, *Université Paris VII*, 1993.

Lyon-Caen, H. and P. Molnar, Gravity anomalies, flexure of the Indian plate, and the structure, support and evolution of the Himalaya and Ganga basin, *Tectonics*, *4*, 513–538, 1985.

Makovsky, Y., S. L. Klemperer, and L. Ratschbacher, Midcrustal reflector on INDEPTH wide-angle profiles: An ophiolitic slab beneath the India-Asia suture in southern Tibet?, *Tectonics*, *18*, 793–808, 1999.

Marshall, G. A., R. S. Stein, and W. Thatcher, Faulting geometry and slipfrom coseismic elevation changes: the 18 October 1989, Loma Prieta, California, earthquake, *Bull. Seism. Soc. Am.*, *81*, 1660–1693, 1991.

Matthews, M. V. and P. Segall, Estimation of depth-dependent fault slip from measured surface deformation with application to the 1906 earthquake, *J. Geophys. Res.*, *98*, 12,153–12,163, 1993.

McCaffrey, R., , and J. Nabelek, Role of oblique convergence in the active deformation of the Himalayas and southern Tibet plateau, *Geology*, *26*, 691–694, 1998.

McHugh, S. and M. Johnston, Surface shear stress, strain, and shear displacement for screw dislocations in a vertical slab with shear modulus constrast, *Geophys. J. R. Astron. Soc.*, *49*, 715–722, 1977.

Meade, B. J., B. H. Hager, S. C. McClusky, R. E. Reilinger, S. Ergintav, O. Lenk, A. Barka, and H. Özener, Estimates of seismic potential in Marmara Sea region from block models of secular deformation constrained by Global Positioning System measurements, *Bull. Seism. Soc. Am.*, *92*, 208–215, 2002.

Mercier, J. P., R. Armijo, P. Tapponnier, E. Carey-Gailhardis, and T. L. Han, Change from Tertiary compression to Quaternary extension in southern Tibet during the Indo-Asia collision, *Tectonics*, *6*, 275–304, 1987.

Metropolis, N., A. Rosenbluth, M. Rosenbluth, A. Teller, and E. Teller, Equation of state calculations by fast computing machines, *J. Chem Phys.*, *21*, 1953, 1953.

Meyer, B., P. Tapponnier, L. Bourjot, F. Metivier, Y. Gaudemer, G. Peltzer, S. Guo, and Z. Chen, Crustal thickening in Gansu-Qinghai, lithospheric mantle subduction, and oblique, strike-slip controlled growth of the Tibet Plateau, *Geophys. J. Int.*, *135*, 1–47, 1998.

Molnar, P., Structure and tectonics of the Himalaya: Constraints and implications of geophysical data, *Ann. Rev. of Earth and Planetary Sciences*, *12*, 489–518, 1984.

Molnar, P., Inversion of profiles of uplift rates for the geometry of dip-slip faults at depth, with examples from the Alps and Himalaya, *Ann. Geophys.*, *5*, 663–670, 1987.

Molnar, P., A review of the seismicity and the rates of active underthrusting and the deformation of the Himalaya, *J. Himalayan Geology*, *1*, 131–154, 1990.

Molnar, P. and W. P. Chen, Seismicity and mountain building, in K. J. Hsu (ed.), *Mountain Building Processes*, pp. pp. 41–57, Academic, New York. 1982.

Molnar, P. and W. P. Chen, Depths and fault plane solutions of earthquakes under the Tibetan Plateau, *J. Geophys. Res.*, *88*, 1180–1196, 1983.

Molnar, P. and Q. Deng, Faulting associated with large earthquakes and the average rate of deformation in central and eastern Asia, *J. Geophys. Res.*, *89*, 6203–6227, 1984.

Molnar, P. and H. Lyon-Caen, Fault plane solutions of earthquakes and active tectonics of the Tibetan Plateau and its margins, *Geophys. J. Int.*, *99*, 123–153, 1989.

Molnar, P. and P. Tapponier, Cenozoic tectonics of Asia: Effects of a continental collision, *Science*, *189*, 419–426, 1975.

Molnar, P., B. C. Burchfiel, L. K'unangyi, and Z. Ziyun, Geomorphic evidence for active faulting in the Altyn Tagh and northern Tibet and qualitative estimates of its contribution to the convergence of India and Eurasia, *Geology*, *15*, 249–253, 1987.

Mooney, W. D. and A. Ginzburg, Seismic measurements of the internal properties of fault zone, *Pure Appl. Geophys.*, *124*, 141–157, 1986.

Murray, M. H., G. A. Marshall, M. Lisowski, and R. S. Stein, The 1992 M=7 Cape Mendocino, California, earthquake: Coseismic deformation at the south end of the Cascadia megathrust, *J. Geophys. Res.*, *101*, 17,707–17,725, 1996.

Nelson, K. D., W. Zhao, L. D. Brown, and et al., Partially molten middle crust beneath southern Tibet: A synthesis of Project INDEPTH results, *Science*, *274*, 1684–1687, 1996.

Ni, J. and M. Barazangi, Seismotectonics of the Himalayan collision zone: geometry of the underthrusting Indian plate beneath the Himalaya, *J. Geophys. Res.*, *89*, 1147–1163, 1984.

Niemi, T. M. and N. T. Hall, Late Holocene slip rate and recurrence of great earthquakes on the San Andreas fault in northern California, *Geology*, *20*, 195–198, 1992.

Okada, Y., Surface deformation due to shear and tensile faults in a half-space, *Bull. Seism. Soc. Am.*, *75*, 1135–1154, 1985.

Pan, Y. and W. S. F. Kidd, Nyainqentanglha shear zone: A late Miocene extensional detachment in the southern Tibet, *Geology*, *20*, 775–778, 1992.

Peltzer, G. and F. Saucier, Present day kinematics of Asia derived from geologic fault rates, *J. Geophys. Res.*, *101*, 27,943–27,956, 1996.

Peltzer, G., P. Tapponier, and A. R., Magnitude of late Quaternary left-lateral displacements along the northern edge of Tibet, *Science*, *246*, 1285–1289, 1989.

Prentice, C. S., Earthquake geology of the northern San Andreas fault near Point Arena, California, *Ph.D. thesis*, *Calif. Inst. of Technol.,Pasadena*, 249pp., 1989.

Prescott, W. H. and S. B. Yu, Geodetic measurement of horizontal deformation in the northern San Francisco bay region, California, *J. Geophys. Res.*, *91*, 7475–7484, 1986.

Prescott, W. H., J. C. Savage, and W. T. Kinoshita, Strain accumulation rates in the western United States between 1970 and 1978, *J. Geophys. Res.*, *84*, 5423–5435, 1979.

Prescott, W. H., M. Lisowski, and J. C. Savage, Geodetic measurement of crustal deformation on the San Andreas, Hayward, and Calaveras faults near San Francisco, California, *J. Geophys. Res.*, *86*, 10,853–10,869, 1981.

Project Altyn Tagh members, *Altyn Tagh fault.* Seismology Press, Beijing, Seismological Bureau of China, Beijing, 1992.

Ratschbacher, L., W. Frisch, G. Liu, and C. Chen, Distributed deformation in southern and western Tibet during and after the Indian-Asia collision, *J. Geophys. Res.*, *99*, 19,917–19,945, 1994.

Rothery, D. A. and S. A. Drury, The neotectonics of the Tibetan Plateau, *Tectonics*, *3*, 19–26, 1984.

Royden, L. H., B. Burchfiel, R. King, E. Wang, Z. Chen, F. Shen, and Y. Liu, Surface deformation and lower crustal flow in eastern Tibet, *Science*, *276*, 788–790, 1997.

Rybicki, K. and K. Kasahara, A strike-slip fault in a laterally inhomogeneous medium, *Tectonophysics*, *42*, 127–138, 1977.

Ryerson, F. J., R. C. Finkel, A. Meriaux, , M. W. Caffee, . Peltzer, T. Farr, O. Chadwick, and D. H. Clarke, Rapid slip on the Altyn Tagh fault; Karakax Valley segment, in *Annual meeting, Geological Society of America, 29*, volume No.26. 1997.

Savage, J. C., A dislocation model of strain accumulation and release at a subduction zone, *J. Geophys. Res.*, *88*, 4984–4996, 1983.

Savage, J. C., Equivalent strike-slip cycles in half-space and lithosphere-asthenosphere earth models, *J. Geophys. Res.*, *95*, 4873–4879, 1990.

Savage, J. C., Displacement field for an edge dislocation in a layered half-space, *J. Geophys. Res.*, *103*, 2439–2446, 1998.

Savage, J. C. and R. O. Burford, Geodetic determination of relative plate motionin California, *J. Geophys. Res.*, *78*, 832–845, 1973.

Savage, J. C. and M. Lisowski, Viscoelastic coupling model of the San Andreas Fault along the big bend, southern California, *J. Geophys. Res.*, *103*, 7281–7292, 1998.

Savage, J. C. and W. H. Prescott, Precision of geodolite distance measurements for determining fault movements, *J. Geophys. Res.*, *78*, 6001–6008, 1973.

Savage, J. C. and W. H. Prescott, Asthenosphere readjustment and the earthquake cycle, *J. Geophys. Res.*, *83*, 3369–3376, 1978.

Savage, J. C., W. H. Prescott, and G. Gu, Strain accumulation in Southern California, *J. Geophys. Res.*, *91*, 7455–7473, 1986.

Savage, J. C., M. Lisowski, and P. W. H., Observed discrepancy between Geodolite and GPS distance measurements, *J. Geophys. Res.*, *101*, 25,547–25,552, 1996.

Savage, J. C., J. L. Svarc, and W. H. Prescott, Geodetic estimates of fault slip rates in the San Francisco Bay Area, *J. Geophys. Res.*, *104*, 4995–5002, 1999.

Savage, J. C., W. Gan, and J. L. Svarc, Strain accumulation and rotation in the Eastern California Shear Zone, *J. Geophys. Res.*, *106*, 21,995–22,007, 2001.

Scholz, C. H., The brittle-plastic transition and the depth of seismic faulting, *Geol. Runds.*, *77*, 319–328, 1988.

Schwartz, D. P., D. Pantosti, K. Okumura, T. Powers, and J. Hamilton, Paleoseismic investigations in Santa Cruz Moutains: Implications for the recurrence of large magnitude earthquakes on the San Andreas Fault, *J. Geophys. Res.*, *103*, 17,985–18,001, 1998.

Seeber, L. and J. Armbruster, Great detachment earthquakes along the Himalayan arc and long-term forecasting, in *Earthquake Predicition: An International Review*, volume Maurice Ewing Series 4, pp. pp. 259–277, AGU, Washington, D. C. 1981.

Seeber, L., J. Armbruster, and R. Quittmeyer, Seismicity and continental subduction in the Himalayan arc, in H. K. Gupta and F. M. Delany (eds.), *Zagros, Hindu Kush, Himalaya, Geodynamic Evolution, Geogyn. Ser.*, volume 3, pp. pp. 215–242, AGU, Washington, D. C. 1981.

Sella, G. F., T. H. Dixon, and A. Mao, Revel: A model for recent plate velocities from space geodesy, *J. Geophys. Res.*, *107(B4)*, 10.1029/2000JB000033, 2002.

Shen, F., L. H. Royden, and B. C. Burchfiel, Large-scale crustal deformation of the Tibetan Plateau, *J. Geophys. Res.*, *106*, 6793–6816, 2001a.

Shen, S. K., M. Wang, Y. Li, D. Jackson, Y. D. D. A, and P. Fang, Crustal deformation along the Altyn Tagh fault system, western China, *J. Geophys. Res.*, *106*, 30,607–30,621, 2001b.

Sibson, R. H., Fault zone models, heat flow, and the depth distribution of earthquakes in the continental crust of the United States, *Bull. Seism. Soc. Am.*, *72*, 151–163, 1982.

Sibson, R. H., Continental fault structure and the shallow earthquake source, *J. Geol. Soc. London*, *140*, 741–767, 1983.

Tapponier, P., G. Peltzer, and R. Armijo, On the mechanics of the collision between India and Asia, in M. P. Coward and A. C. Ries (eds.), *Collision Tectonics*, pp. pp. 115–157, Geol. Soc. Spec. Publ. 1986.

Tapponnier, P. and P. Molnar, Active faulting and Cenozoic tectonic of China, *J. Geophys. Res.*, *82*, 2905–2930, 1977.

Tapponnier, P. and P. Molnar, Active faulting and Cenozoic tectonic of the Yian Shan, Mongolia, and Baykal regions, *J. Geophys. Res.*, *84*, 3425–3459, 1979.

Tapponnier, P., J. L. Mercier, and F. P. et al., The Tibetan side of the India-Eurasia collision, *Nature*, *294*, 405–410, 1981.

Tapponnier, P., B. Meyer, J. P. Avouac, G. Peltzer, Y. Gaudemer, S. Guo, H. Xiang, K. Y. Z. Chen, S. Cai, , and H. Dai, Active thrusting and folding in the Qi Lian Shan, and decoupling between upper crust and mantle in northeastern Tibet, *Earth Planet. Sci. Lett.*, *97*, 382–403, 1990.

Thatcher, W., Strain release mechanism for the 1906 San Francisco earthquake, *Science*, *184*, 1283–1285, 1974.

Thatcher, W., Nonlinear strain buildup and the earthquake cycle on the San Andreas fault, *J. Geophys. Res.*, *88*, 5893–5902, 1983.

Thatcher, W. and P. C. England, Ductile shear zones beneath strike-slip faults: Implications for the thermomechanics of the San Andreas fault zone, *J. Geophys. Res.*, *103*, 891–905, 1998.

Thatcher, W., G. Marshall, and M. Lisowski, Resolution of fault slip along the 470-km-long rupture of the great 1906 San Francisco earthquake and its implications, *J. Geophys. Res.*, *102*, 5353–5367, 1997.

Unsworth, M. J., P. E. Malin, G. D. Egbert, and J. R. Booker, Internal structure of the San Andreas fault at Parkfield, California, *Geology*, *25*, 359–362, 1997.

van der Woerd, J., F. J. Ryerson, P. Tapponnier, A. S. Mériaux, Y. Gaudemer, B. Meyer, R. C. Finkel, M. W. Caffee, G. Zhao, and Z. Xu, Uniform slip-rate along the Kunlun fault: implication for seismic behaviour and large-scale tectonics, *Geophys. Res. Lett.*, *27*, 2353–2356, 2000.

van der Woerd, J., A.-S. Mériaux, Y. Klinger, F. J. Ryerson, Y. Gaudemer, and P. Tapponnier, The 14 November 2001, M_w=7.8 Kokoxili Earthquake in Northern Tibet (Qinghai Province, China), *Seism. Res. Lett.*, *73*, 125–135, 2002.

Wang, Q., P.-Z. Zhang, J. T. Freymueller, R. Bilham, K. Larson, X. Lai, X. You, Z. Niu, J. Wu, Y. Li, J. Liu, Z. Yang, and Q. Chen, Present-day crustal deformation in China constrained by Global Positioning System measurements, *Science*, *294*, 574–577, 2001.

Wentworth, C. M., Upper Cretaceous and lower Tertiary strata near Gualala, California, and inferred large right slip on the San Andreas faults, in W. R. Dickinson and G. Arthur (eds.), *Proceedings of conference on geologic problems of San Andreas fault system: Stanford, California*, pp. 130–143, Stanford University Publications in Geological Sciences. 1968.

Williams, S. D. P., J. L. Svarc, M. Lisowski, and W. H. Prescott, GPS measured rates of deformation in the northern San Francisco Bay region, California, 1990-1993, *Geophys. Res. Lett.*, *21*, 1511–1514, 1994.

Wood, M. D., Time dependent tilt response to ocean loading for sites across the San Andreas fault, in *Conference on tectonic problems of the San Andreas fault system, Proceedings*, volume 13, p. 124, Stanford University Publications in Geological Sciences. 1973.

Working Group on California Earthquake Probabilities, Earthquake Probabilities in the San Francisco Bay Region: 2000-2030, *U.S. Geol. Survey Open File Rep.*, *99-517*, 1999.

Yin, A., P. A. Kapp, M. A. Murphy, C. E. Manning, T. M. Harrison, M. Grove, D. Lin, X.-G. Deng, and C.-M. Wu, Significant late Neogene east-west extension in northern Tibet, *Geology*, *27*, 787–790, 1999.

Zhao, W., J. Mechie, J. Guo, F. Wenzel, R. Meissner, L. Ratschbacher, H. Steentoft, S. Husen, H. J. Brauner, D. Jiang, W. Frisch, and S. F. Hauff, Seismic mapping of crustal structures beneath the indus-Yarlung suture, Tibet, *Terra Nova*, *9*, 42–46, 1997.

Zumberge, J. F., M. B. Heflin, D. C. Jefferson, M. M. Watkins, and F. H. Webb, Precise point positioning for the efficient and robust analysis of GPS data from large networks, *J. Geophys. Res.*, *102*, 5005–5018, 1997.